REPORT DOCUMENTATION PAGE

AFRL-SR-BL-TR-99-

0258

ived
4-0188

d, and completing and reviewing
es, Directorate for Information

1. AGENCY USE ONLY *(Leave blank)*	2. REPORT DATE	3. REPORT TYPE AND DATES COVERED
		FINAL TECHNICAL REPORT 15 jUL 96-14 jUL 99

4. TITLE AND SUBTITLE
MICRO HEAT EXCHANGER USING MEMS IMPINGING JETS AND VACUUM-INSULATED SKIN

5. FUNDING NUMBERS
F49620-96-1-0376

A564/56
63739E

6. AUTHOR(S)
YU-CHONG TAI, CHIH-MING HO

7. PERFORMING ORGANIZATION NAME(S) AND ADDRESS(ES)
CALIFORNIA INSTITUTE OF TECHNOLOGY
ELECTRICAL ENGINEERING DEPARTMENT
PASADENA, CA 91125

8. PERFORMING ORGANIZATION REPORT NUMBER

9. SPONSORING/MONITORING AGENCY NAME(S) AND ADDRESS(ES)
AIR FORCE OFFICE OF SCIENTIFIC RESEARCH
110 DUNCAN AVENUE SUITE B115
BOLLING AFB DC 20332-8050

10. SPONSORING/MONITORING AGENCY REPORT NUMBER

11. SUPPLEMENTARY NOTES

12a. DISTRIBUTION AVAILABILITY STATEMENT
APPROVED FOR PUBLIC RELEASE, DISTRIBUTION IS UNLIMITED

12b. DISTRIBUTION CODE

13. ABSTRACT *(Maximum 200 words)*
The goal of this work was to study micro impinging jet cooling, focusing on experimentation with variable parameters of height, nozzle diameter, and nozzle spacing in the sub-millimeter range. The objective of this project is to obtain a set of design rules that can be used to develop an efficient and economical heat exchanger that will meet present and future integrated circuit microchip cooling requirements. The two factors which largely determine the efficiency of a heat exchanger in this situation is (1) its ability to transfer heat from the chip surface to a transport medium, usually air, and (2) this medium's capacity to convect the heated fluid away from the chip. Our proposed solution was to develop and characterize a micro jet impingement cooling system. A high-speed cool gas directly impinges on the hot surface through MEMS nozzle/slot array, and penetrates deep into the boundary layer to form a sharp temperature gradient. About one nozzle length downstream, the coherent structures in the jets induce an unsteady separation which has a strong upward motion to carry the heat away from the surface.

14. SUBJECT TERMS			15. NUMBER OF PAGES
			80
			16. PRICE CODE

17. SECURITY CLASSIFICATION OF REPORT	18. SECURITY CLASSIFICATION OF THIS PAGE	19. SECURITY CLASSIFICATION OF ABSTRACT	20. LIMITATION OF ABSTRACT
U	U	U	

Micro Heat Exchanger Using Impinging Jets

Final Report
September 16, 1999

Yu-Chong Tai

Electrical Engineering Department
Division of Engineering and Applied Science
California Institute of Technology
Pasadena, CA 91125

Phone: (818) 395-8317   Fax: (818) 584-9104
E-mail: yctai@touch.caltech.edu
Web: http://mems.caltech.edu

Chih-Ming Ho

Mechanical and Aerospace Engineering Department
University of California, Los Angeles
Los Angeles, CA 90095

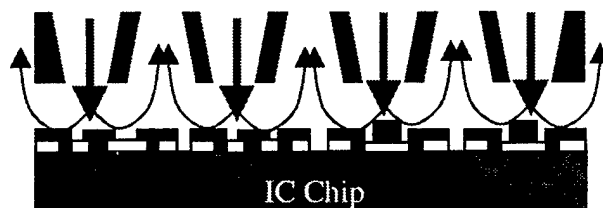Phone: (310) 825-9993   Fax: (310) 206-2302
E-mail: chihming@seas.ucla.edu
Web: http://ho.seas.ucla.edu

1

19991109 102

Table of Contents

1. INTRODUCTION

1.1 Background

The thermal conductivity of thin films can be one to two orders of magnitude lower than the bulk thermal conductivity [1]; thus even small power dissipation in a thin-film region may cause serious local heating in micro devices including IC's and MEMS. Moreover, as the transistor density, or the number of transistors on a standard-sized chip, increases in IC's, the power dissipation also increases. It is therefore necessary to investigate better thermal cooling methods for future chip cooling. It is interesting to note that for a chip under a given heat flux and a maximum allowable chip temperature increase, the tangential forced-convection heat transfer coefficient, h, is on the order of 0.01 W/cm^{2}K [2]. For impinging-jet cooling, on the other hand, the heat transfer coefficient can be one order of magnitude larger, i.e., approximately $h = 0.3$ W/cm^{2}K. Thus, impinging-jet cooling is a promising cooling method with the advantage of single-phase (gas phase) cooling.

Unfortunately, impinging-jet cooling experiments reported in the literature to date have mainly used macro-scale impinging jets [3]. In addition, these works focused largely on turbulent jets with H/D ratios greater than 1.0, where H is the spacing between the nozzle and impingement surface (also called the height of the jet) and D the diameter of the jet. Interestingly, the regime with H/D ratios less than 1.0 can now be studied since MEMS technology can produce micro-scaled jets. As a result, a more efficient micro heat exchanger may become possible, since micro jets can be placed much closer to the hot surface than macro jets. The goal of this work was to study micro impinging jet cooling, focusing on experimentation with variable parameters of height, nozzle diameter, and nozzle spacing in the sub-millimeter range.

1.2 Project goals

The objective of this project was to obtain a set of design rules that can be used to develop an efficient and economical heat exchanger that will meet present and future integrated circuit microchip cooling requirements. The two factors which largely determine the efficiency of a heat exchanger in this situation is (1) its ability to transfer heat from the chip surface to a transport medium, usually air, and (2) this medium's capacity to convect the heated fluid away from the chip.

1.3 Proposed Solution

The proposed solution was to develop and characterize a micro jet impingement cooling system, as conceptually illustrated in figure 1.3.1. A high-speed cool gas directly impinges on the hot surface through MEMS nozzle/slot array, and penetrates deep into the boundary layer to form a sharp temperature gradient. About one nozzle length downstream, the coherent structures in the jets induce an unsteady

4

separation (Didden and Ho, 1985) which has a strong upward motion to carry the heat away from the surface. The distance between the nozzle plane and the hot surface is much smaller than that in a macro model so that a much higher heat flux can be achieved. In some cases, the cooling is even more efficient by arranging nozzles to cool the hot spots locally on the electronic chip. Furthermore, our proposed MEMS heat exchanger will be economical because of the capability of mass production from MEMS technologies. Finally, it will be easy to use because only cold air is required so that many difficult technical and reliability problems in the liquid-phase or multi-phase heat exchanger are avoided.
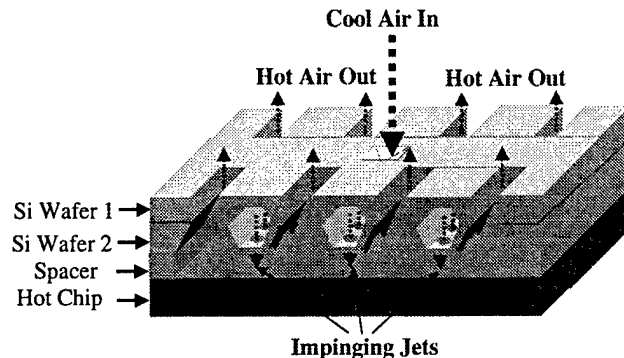
Figure 1.3.1. Conceptual illustration of MEMS impinging jet heat exchanger.

In additional to convective heat transfer due to impinging jet, the characteristics of the fluid flow along its path from the reservoir to the jet nozzle will also have a significant impact on the heat exchanger's performance. At the micro scale, such flow paths often take the form of micro channels. Therefore, the study of micro channel flow will greatly facilitate the understanding of fundamental operation principles of micro heat exchangers, and provide for an effective tool in practical micro heat exchanger design. Figure 1.3.2 shows our proposal for micro channel flow study. Using surface micromachining technique, we fabricate robust micro channels, which are able to withstand pressures up to several hundred pounds per square inch. Micro sensors are integrated with the micro channels so that we are able to obtain the temperature, pressure, and flow rate information during the fluid flows through the channels. Further more, undercutting the silicon underneath thermally isolates the channel, which allows us to study the thermal effect of micro channel flow.
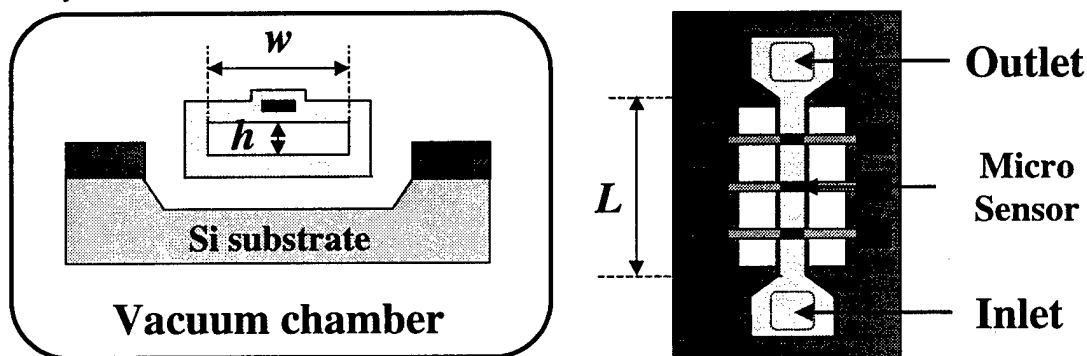
Figure 1.3.2 Conceptual illustration of MEM freestanding micro channel integrated with micro sensors.

2. MEMS HEAT EXCHANGER

2.1 Introduction

The problem has been broken up into three distinct engineering and research focus areas. The first part is the design and fabrication of single micro nozzles and nozzle arrays. The second part is the design, fabrication and characterization of a "target sensor chip", or "temperature imager", which simulates heat fluxes found in present microprocessors and has an embedded sensor array to measure surface temperature distributions. The third part is the characterization of heat convection away from the impingement region via the investigation of high-pressure fluid flow in instrumented micro channels. The data obtained from experiments with these devices can be used to formulate rules for the optimal design of micro impinging jet heat exchangers based on air inlet pressure conditions or maximum allowable surface temperature.

2.2 Simulation of Impinging Jets by Computational Fluid Dynamics (CFD)

Simulation of impinging jet has been run by computational fluid dynamics software in order to compare different jet designs. Since verification of CFD Research Corporation's CFD-ACE software was necessary before micro scale numerical results could be believed, we decided to model an impinging jet system with a micro chip heat source, as seen in figures 2.2.1 and 2.2.2. These 3-D simulations were run on a Pentium II 300 MHz system. Taking advantage of symmetry, only one quarter of the impinging jet system had to be gridded. The 0.5-mm jet enters the system at a constant velocity in the lower left corner of the figure. The 0.5 cm x 0.5 cm area directly below the jet is given a constant heat flux of 1 w/cm^2, thus simulating the effective heat flux in the mini jet experiments. In order to simplify the gridding of the system, the area directly above the "chip" is defined as a solid wall, resulting in more of a confined jet simulation. The lower area extending from the chip is defined as an adiabatic wall. The area directly above this surface is defined as a constant pressure outlet.

These simulations were run with the same nozzle at three heights (500 um, 750 um, and 1.0 mm) and at inlet velocities from 10 m/s to 150 m/s. This yields Reynolds numbers from approximately 690 to 10,300. Figures 2.2.1 and 2.2.2 are sample solutions at various heights at Re = 6900. The temperature distribution over and away from the chip is displayed along with a graph (in the lower left corner of each figure) showing the diagonal Nussuelt number distribution along the chip. Following an analysis process similar to the data reduction of the experimental mini impinging jet results, we calculated an average Nu at each configuration situation. Plotting average Nu vs. Re$^{0.5}$ at each height yields "efficiency" lines similar to the one shown in figure 2.2.3. This shows that the efficiency of the impinging jet increases, as evident in the increasing slope (Nu vs. square root of Re) values with each decrease in height.
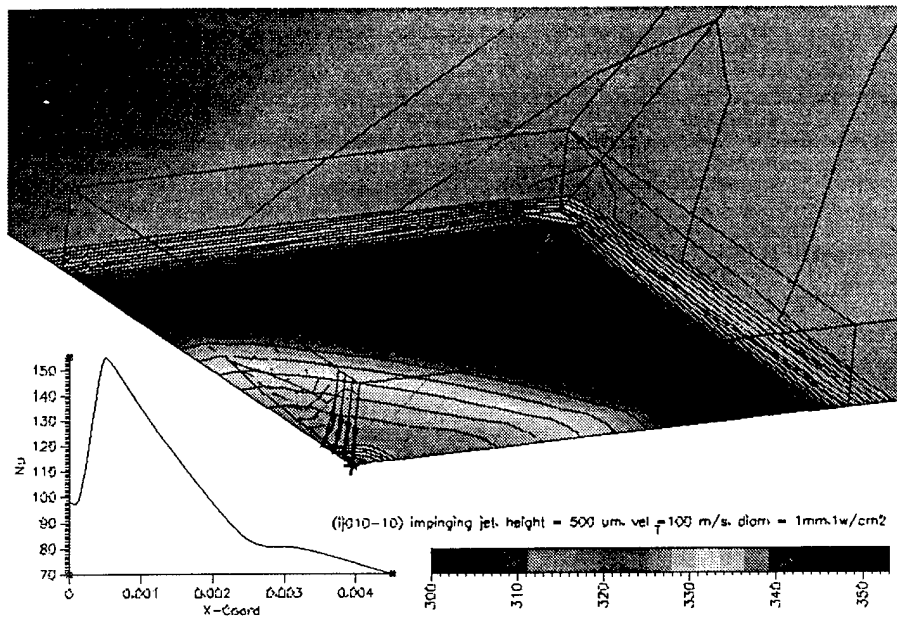
Figure 2.2.1. Sample CFD result for an impinging jet 500 um from the target chip surface.
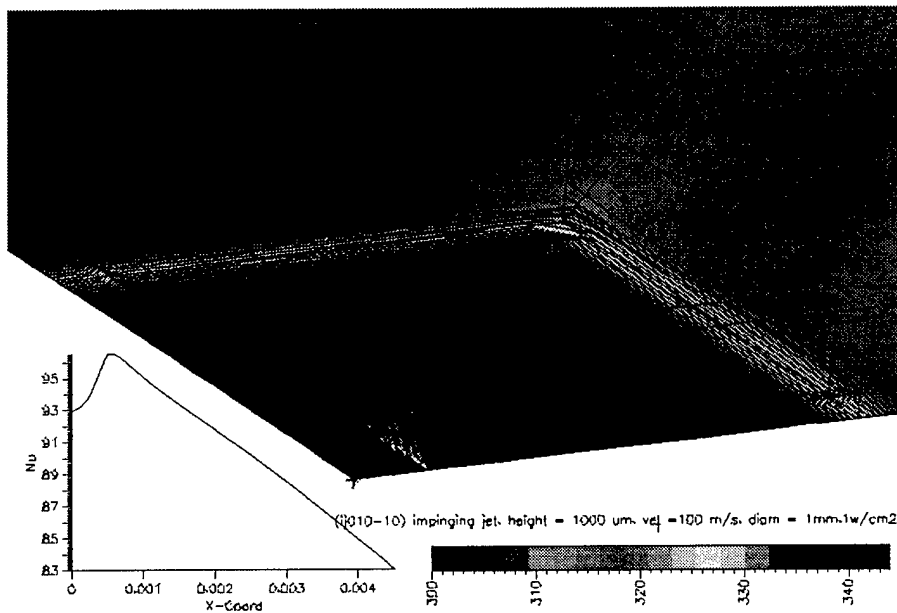
Figure 2.2.2. Sample CFD result for an impinging jet 1000 um from the target chip surface.

Before beginning micro nozzle fabrication, it was necessary to test possible nozzle designs using CFD simulations. Figures 2.2.4 and 2.2.5 show 2 different nozzle designs that were simulated using the CFD-ACE solver. Fluid enters from the appropriate location at the top of the figures (fixed inlet velocity) and exits along the top and sides (fixed exit pressure). The type A nozzle in figure 2.2.4 has more of a free jet configuration, where the fluid is allowed to recirculate in an open region next to the

7

nozzle. Type B nozzles have more of a confined jet design where the side walls of the nozzle are thicker, thus constraining the fluid as it flows away from the impingement point. These figures show the different nozzles with the same inlet velocity and at a H/D ratio of 0.5 (a 1mm nozzle that is 0.5 mm above the surface). Noting the similarity in the temperature distributions in both figures, it seems that there is no clear advantage in either design, numerically. These incompressible flow with heat transfer simulations were also conducted at other different H/D ratios (1 and 2) and injection velocities (20 m/s and 50 m/s), but similarly, no distinct advantage, based on temperature distribution, was observed.

Impinging Jet Efficiency Trend (CFD)

$y = -0.0014x + 2.7333$

y-axis: Nu slope (efficiency), x-axis: height (um)

Figure 2.2.3. Numerical result showing that heat transfer efficiency increases with decreasing nozzle height.

Noz A (3D) inlet = 10 m/s 1mm nozzle 0.5 mm height . 1 w/cm2
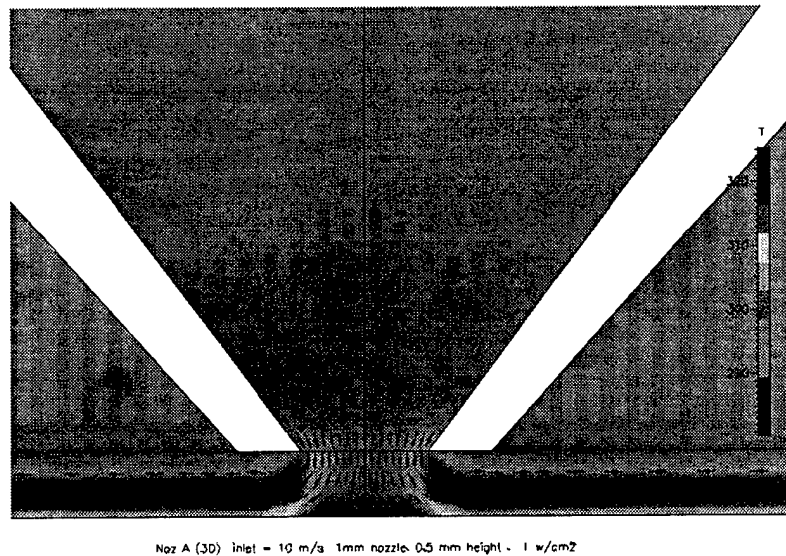
Figure 2.2.4. CFD result for a locally free jet-type micro nozzle with a h/D ratio of 0.5
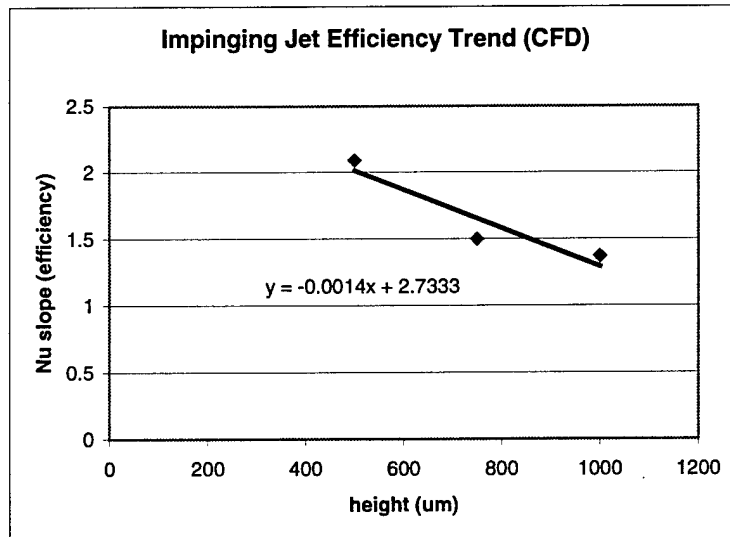
8

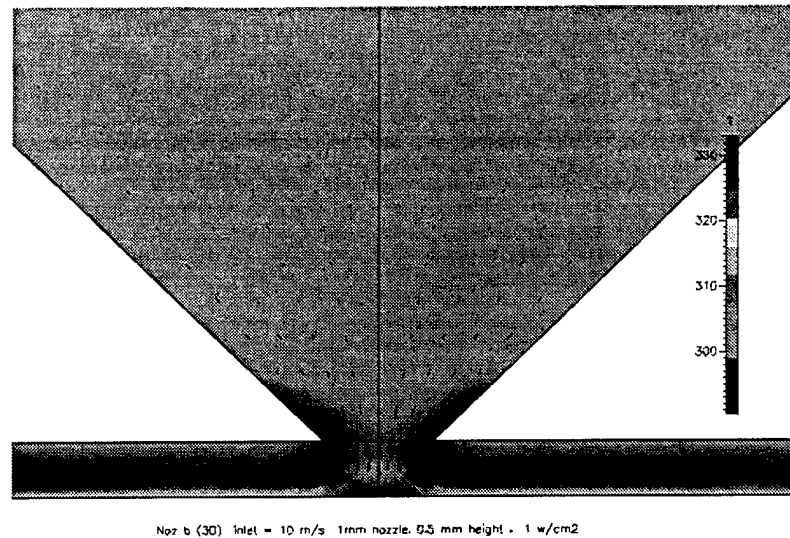Noz b (30) Inlet = 10 m/s 1mm nozzle. 0.5 mm height . 1 w/cm2

Figure 2.2.5. CFD result for a locally confined jet-type micro nozzle with a h/D ratio of 0.5

2.3 Design and Fabrication of MEMS Devices

2.3.1 First Generation MEMS Single Nozzle

Precisely formed nozzles with exit diameters in the range from 1 um to 500 um are not commercially available. In addition, glass pipettes and plastic tubing cannot be formed to the exact contours necessary for them to act as contraction region for sonic nozzles. This leaves MEMS as the leading technology candidate for the fabrication of micro nozzles. The following sections will outline the design and fabrication steps of micro nozzles appropriate for MEMS impinging jet heat exchanger.

MEMS single nozzles similar to the Type B configuration have been fabricated, shown in figure 2.3.1. The fabrication process, illustrated in figure 2.3.2, begins with a nitride layer deposited on both sides of a bare <100> Si wafer . Etch holes are patterned and opened in the backside nitride using RIE, and the 500 um thick wafer is then isotropically etched in KOH. An RIE etch is used to open a circular nozzle pattern on the front side nitride. This process is used to produce circular single jets with inlet diameters of 1.5 mm and outlet diameters ranging from 0.5 mm to 1.5 mm.

2.3.2 First Generation MEMS Slot Arrays

MEMS nozzle and slot arrays have also been fabricated. These arrays are made by bonding two separate chips together. The fabrication process of both chips is shown in figure 2.3.3. The wafer on the left defines the nozzles/slots and the wafer on the right defines the gas inlets. The two pieces are fabricated with the same process. Starting with <100> Si wafers, openings for the nozzles/slots are first etched in KOH. Then a 5000 Å thick thermal oxide is grown on both sides over the openings as a protective layer.

9

Etching windows are then opened in the oxide, and followed by KOH through-wafer etching. After dicing, the thermal oxide is removed using BHF. To make a final array chip, a pair of matching chips are then aligned and fusion bonded. Finally, the bonded array chip is deposited with a 4-µm-thick layer of Parylene. This Parylene layer serves two purposes. One is to seal any unbonded surfaces, and the other is to increase thermal insulation from the ambient.

Process Flow

Silicon Nitride

1. Silicon Nitride Deposition
2. Backside Window Opening

3. Etch through Wafer by KOH

4. Nozzle Opening on Si Membrane
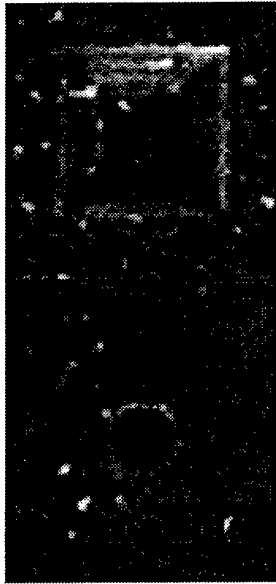
Figure 2.3.1. Prototype MEMS nozzle.   Figure 2.3.2. Prototype nozzle fabrication
process.

1. Gas Inlet and Outlet Patterning

2. Growth of Thermal Oxide   Thermal Oxide
3. Windows Opening for KOH

4. Wet Etch by KOH
5. Thermal Oxide Stripping

6. Si-Si Fusion Bonding   Parylene
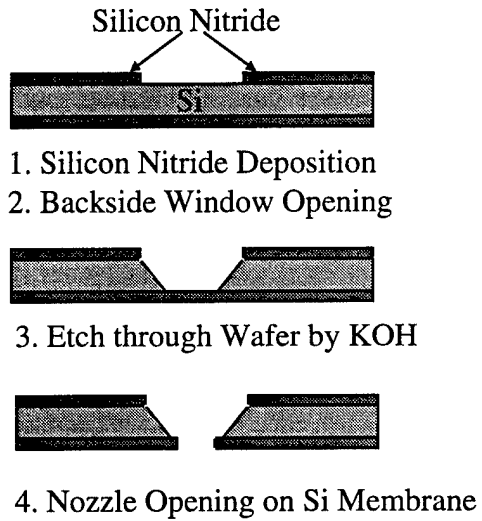
7. Parylene Coating
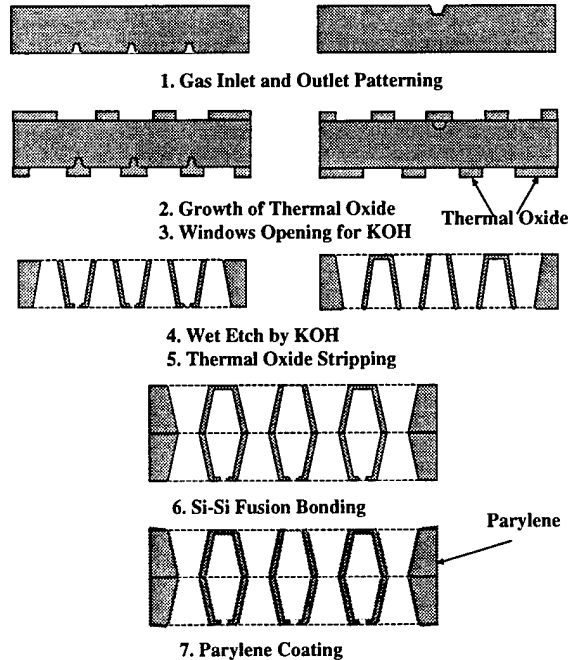
Figure 2.3.3. MEMS jet array process flow.

Figure 2.3.4 shows the finished nozzle and slot arrays. In the figure, the circular nozzles are in 1mm diameter, and the slots are 1mm wide and 8 mm long. Rows of nozzles/slots are spaced 2.5 mm apart from center to center. The entire structure is approximately 1mm thick.
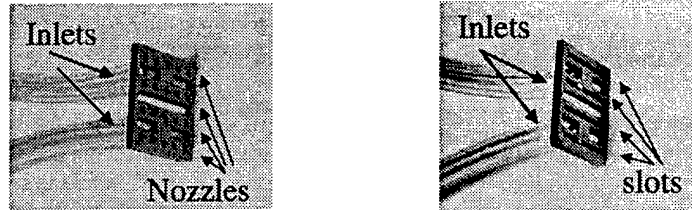
Figure 2.3.4. Micromachined nozzle and slot array.

2.3.3 Second Generation MEMS Single Nozzles and Nozzle Arrays

In order to reduce the confinement effect, the second generation MEMS single nozzles and nozzle arrays have been fabricated. Figures 2.3.5 and 2.3.6 show such 2nd generation MEMS single nozzle and nozzle arrays in 1 x 2, 2 x 2 and 10 x 10 arrangements. The nozzles (diameter D=0.5 mm) are made with two DRIE steps and have a thin wall (0.1 mm) to eliminate flow confinement between the nozzle and chip, improving heat transfer effectiveness. The fabrication process is shown in figure 2.3.7. Starting with a thermal oxide layer grown on both sides of a bare <100> Si wafer, thermal oxide was patterned to define nozzles. Then photoresist was spin coated and patterned for the nozzle wall. After the first DRIE for 200mm to initiate nozzles, thermal oxide was removed from most of the wafer except the underneath the photoresist, which defines the nozzle wall. The second step of DRIE is then applied to etch through the wafer to complete the nozzles.

Figure 2.3.5. MEMS single and 2 x 1 array nozzles.
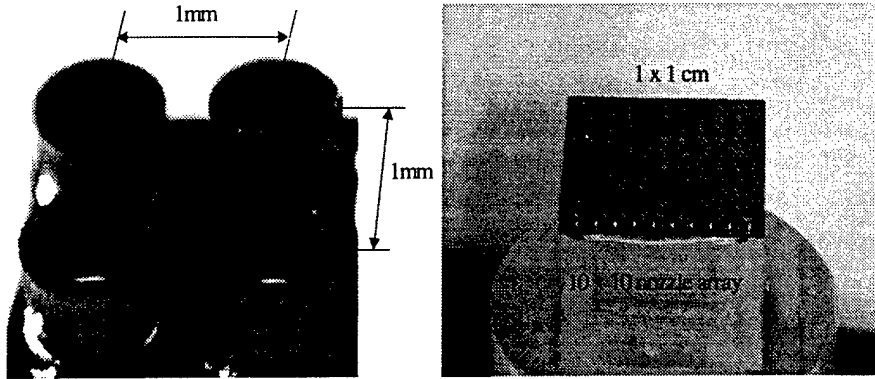
Figure 2.3.6. MEMS 2 x 2 and 10 x 10 array nozzles.
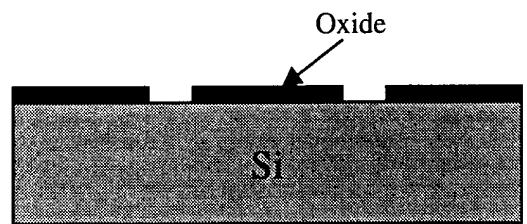
1. Thermal Oxidation.
2. Patterning oxide defines nozzles.
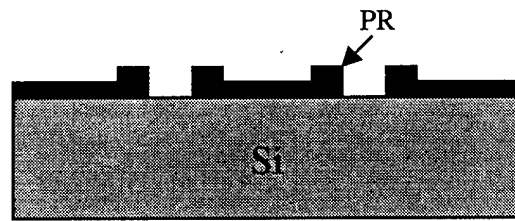
3. PR spinning and patterning nozzle wall.
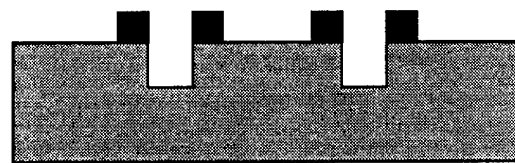
4. DRIE 200 μm to initiate nozzles.
5. Oxide etching.
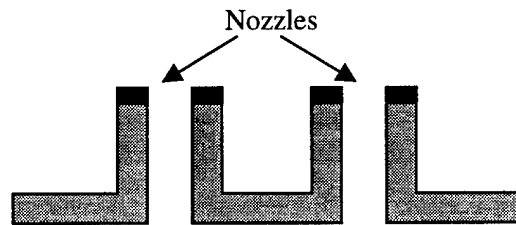
6. DRIE through-etching to complete nozzles.

Figure 2.3.7. Process Flow.

2.3.4 Polysilicon Thin Film Temperature Sensors

Both heavily and lightly doped polysilicon thin film temperature sensors have been designed as shown in figure 2.3.8. The lightly doped sensor can 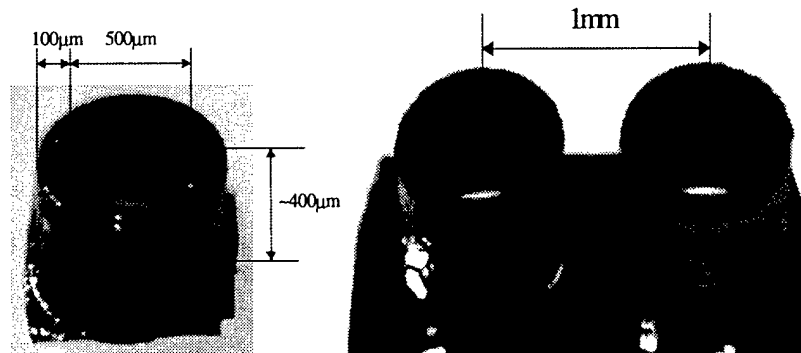be designed as small as a few microns in square, which is good for a local temperature measurement. The zip-zap shape of the heavily doped sensor can be arranged to cover a lager area, which is good to measure the average temperature of the covered area. The fabrication process is shown in figure 2.3.9. Starting from a bare silicon wafer, 0.5μm thick thermal oxide is grown for electrical isolation and then 0.2 μm thick low stress LPCVD silicon nitride is deposited as a passivation layer. 0.5 μm thick LPCVD polysilicon is deposited as the sensor material, then selectively doped with B^+ implantation followed by activation annealing at temperatures between 900 to1100°C for 30 minutes. After patterned by RIE, the sensor is protected by the deposition of another layer of 0.2μm thick low stress LPCVD silicon nitride. Finally, the contact area is opened by RIE, and 1 μm thick Al is deposited and patterned to provide leads for the sensor. Figures 2.3.10 and 2.3.11 show the pictures and temperature calibration of fabricated sensors.
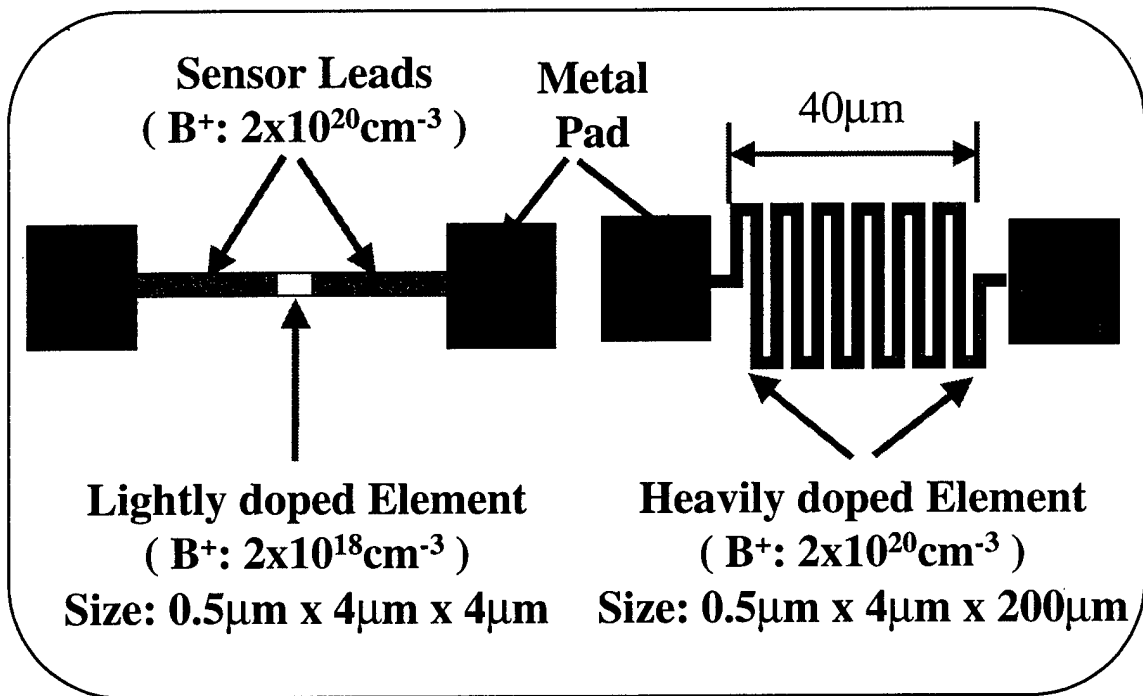
Figure 2.3.8. Designs of heavily and lightly doped polysilicon thin film temperature sensors.
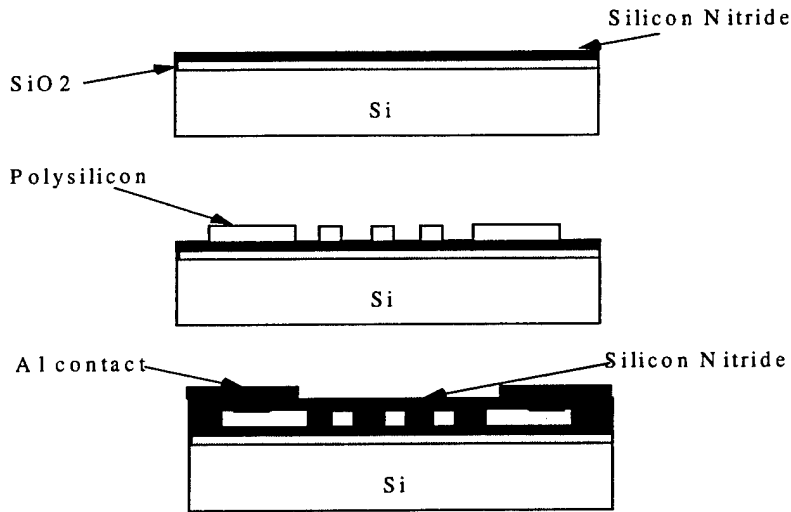
Figure 2.3.9. Process flow of a polysilicon thin film temperature sensor.
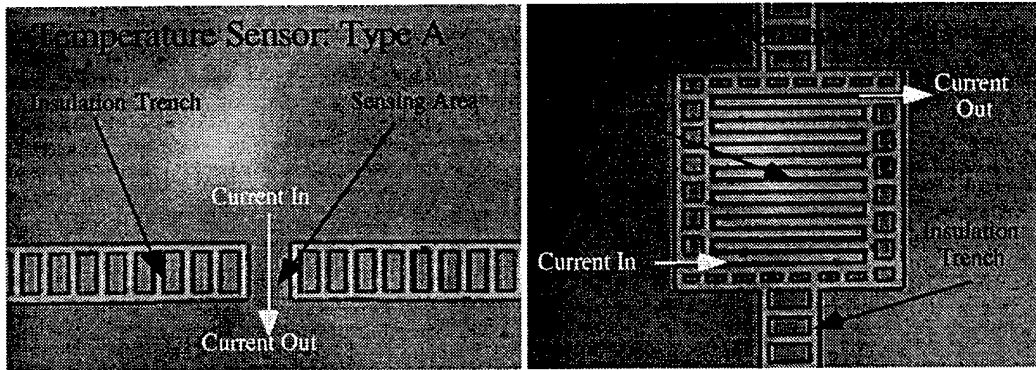
Figure 2.3.10. Pictures of fabricated polysilicon thin film temperature sensors.
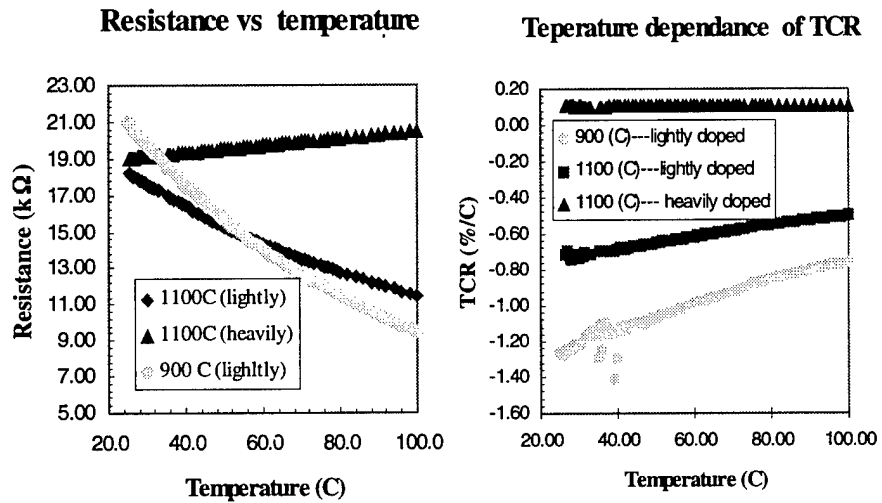
Figure 2.3.11. Temperature calibration of fabricated polysilicon thin film temperature sensors.

2.3.5 Polysilicon Thin Film Heater

Polysilicon thin film heaters have been designed to simulate the power source generated by electronic circuits. Figure 2.3.12 shows two different mask designs of B^+ doped (2×10^{20} cm^{-3}) polysilicon heaters: (a) A heater formed by polysilicon thin film sheet (0.5μm thick), and (b) A heater formed by many zigzag shaped polysilicon resisters in parallel. Both heaters have a resistance about 50Ω. The process of the heater is similar to that of polysilicon thin film temperature sensor as shown in figure 2.3.9.

A Polysilicon Sheet   **Metal Contacts**   **Polysilicon Resisters**

(a)   (b)
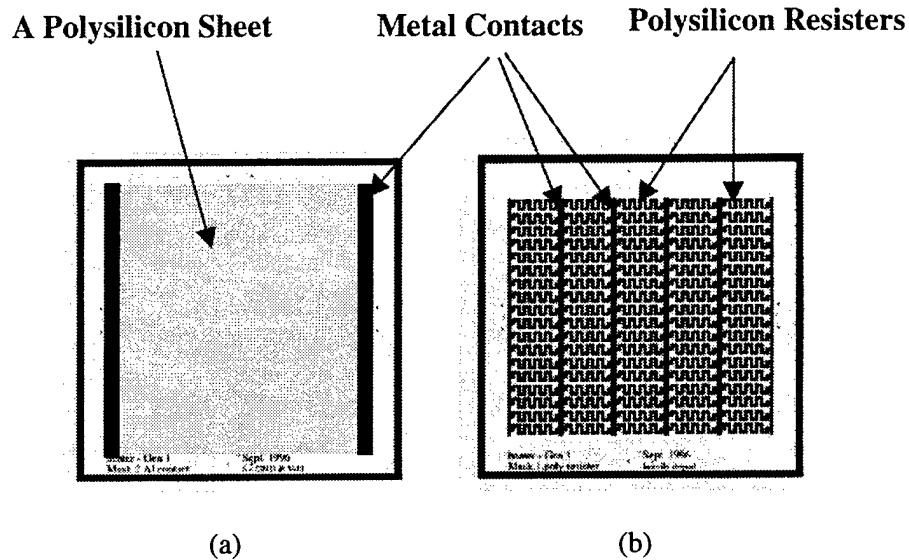
Figure 2.3.12. (a) Polysilicon thin film sheet Heater. (a) Parallel polysilicon resister heater.

2.3.6 Silicon Temperature Imager

A temperature imager or sensor-array chip, shown in figure 2.3.13, was fabricated in order to serve as a test target for the impinging jets. This 2 cm x 2 cm chip has an integrated polysilicon heater on the backside and 8x8 temperature sensors on the front side. The 64 thermistor-type polysilicon sensors, each 4 μm x 4 μm, are 500 μm apart and are placed in a 4 mm x 4 mm area at the center of the top surface. These polysilicon temperature sensors have a nominal room-temperature resistance of about 20 kΩ and a temperature resolution of 0.1 °C.

The fabrication process of the sensor chip is given in figure 2.3.14. Starting with bare <100> silicon, a 5000 Å thick layer of dry thermal oxide and a 2000 Å thick layer of LPCVD nitride are deposited. Then 5000 Å of LPCVD polysilicon is deposited for the sensors and doped with boron to a concentration of 5×10^{18} cm^{-3}. The sensors are then encased in another 2000 Å thick nitride layer that electrically isolates and protects the sensors. Finally contact holes are opened in the nitride by RIE and aluminum metalization finishes the sensor process. Here, the backside heater is fabricated similarly, with the only differences in masking and the backside polysilicon doping, i.e., heavily boron doped at 5×10^{20} cm^{-3}.
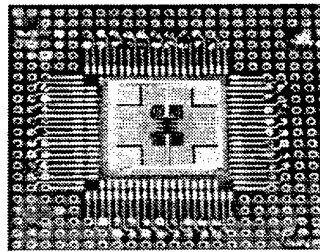
Figure 2.3.13. Temperature-sensor chip mounted on a PCB in a Plexiglas chuck.

Figure 2.3.15 shows preliminary calibration of 16 (four from each side) randomly selected sensors on the chip. Due to non-uniformities in the ion implantation or over etching of some sensors, the room temperature resistance ranges from approximately 12 $k\Omega$ to 28 $k\Omega$. Thus every sensor must be calibrated individually in an isothermal oven. In order to expedite the calibration process, a new, more stable constant current circuit has been designed.

1. Thermal Oxidation
2. LPCVD Nitride

3. LPCVD Poly
4. Ion Implantation
5. Sensor and Heater Patterning

6. LPCVD Nitride
7. Contact Hole Opening
8. Metalization
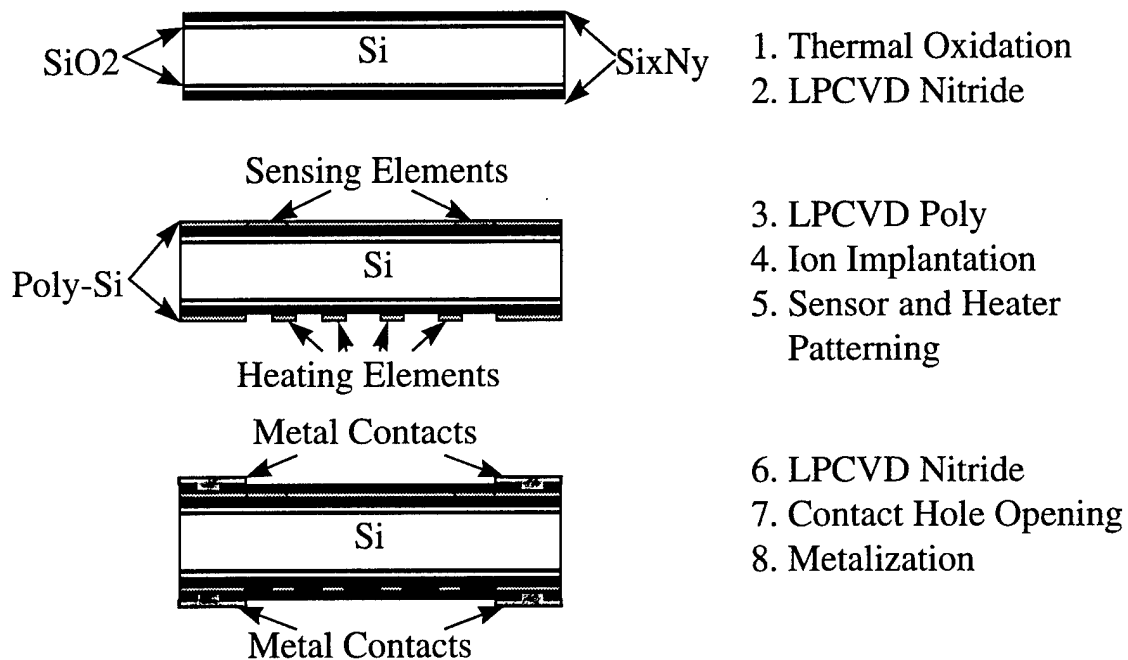
Figure 2.3.14. Process flow for a temperature-sensor chip with an integrated heater on the backside.
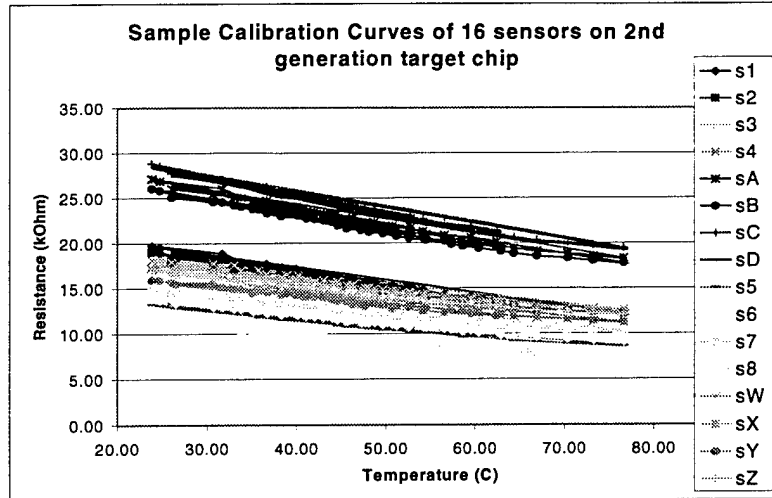
Figure 2.3.15. Calibration curves of the sensors on silicon target chip

2.3.7 Quartz Temperature Sensor Array Chip

A second-generation, temperature-sensor-array chip was successfully fabricated and used as a test target for the impinging jet system. This 2 cm x 2 cm device, fabricated on a quartz substrate, has integrated heating resistors on the bottom and 84 temperature sensors on the top. Figure 2.3.16 shows a completed 2nd generation chip embedded onto a PC board, which provides the necessary interconnects, and the entire setup is ready for mounting on a vacuum chuck for impinging jet testing. The uniformity of the surface temperature distribution produced by these backside heaters was verified by direct measurement from the calibrated surface sensors.

PC Board   Sensor Chip
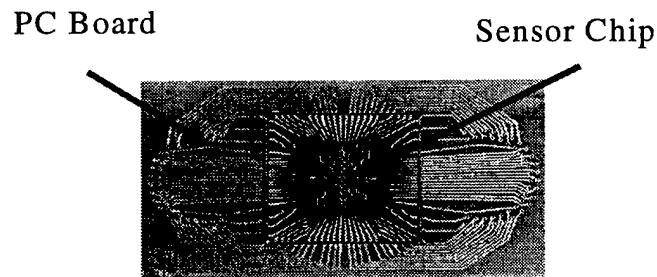
Figure 2.3.16. Quartz target test chip with integrated sensors and heaters mounted onto a PC board.

Quartz was used as a substrate because its thermal conductivity is two orders of magnitude lower than silicon (1.4 W/mK versus 148 W/mK). This should increase the thermal isolation of each temperature sensor embedded on the surface, as well as improve the acquisition of local temperature measurements. Each individual sensor is 4um x 4um in area, as pictured in Figure 2.3.17A. In addition, similar silicon based target chips were also fabricated. These chips incorporated all the integrated sensors and heaters of the

quartz design, plus the added bonus of having backside temperature sensors for heat flux measurements. The backside sensors are pictured in Figure 2.3.17B. Benefiting from experience with previous target chip designs, we arranged the sensors a semi-radial array from the center. As shown in Figure 2.3.18, near the center, the sensors are regularly spaced in a 5x5 square array. Further away, the remaining 59 sensors are separated in the theta-direction every 22.5 degrees. Their radial spacing has also been staggered in order to increase the concentration of sensors near the center, the jet impingement point. Also, the radial spacing gradually increases away from the center.
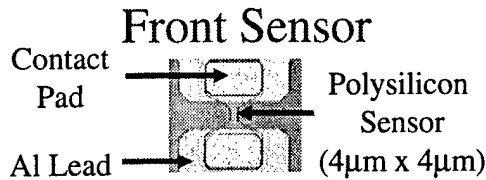
Figure 2.3.17A. Front side sensor.
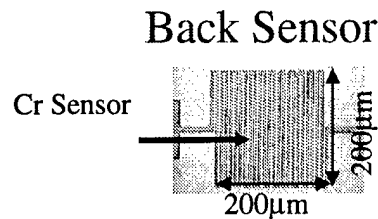
Figure 2.3.17B. Backside sensor.
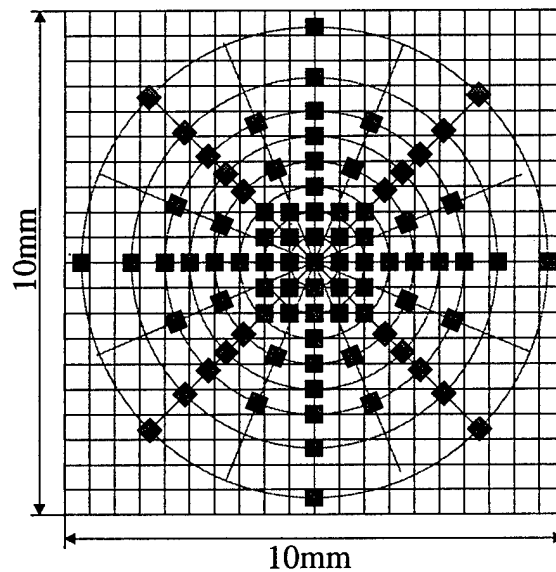
Figure 2.3.18. Sensor arrangement.

As illustrated in Figure 2.3.19, the process flow for the quartz based sensor array is similar to previous designs. Starting with a bare 4 in. diameter, 0.5mm thick quartz wafer, 0.5 um of polysilicon is LPCVD deposited. The poly is then masked and boron ions are implanted. The lightly doped poly, defining the sensors, is then remasked and ion implantation is repeated to yield the heavily doped, lower resistance contact leads for each sensor. The excess polysilicon is then patterned and removed by a RIE. Next, an approximately 1.5 um-thick layer of LTO is LPCVD deposited. The entire wafer is then annealed at 1050°C for 30 minutes. Then, RIE is used to open contact openings on the topside in the oxide. Processing of the topside is finished after the deposition of a 1um thick layer of aluminum contact pattern.

18
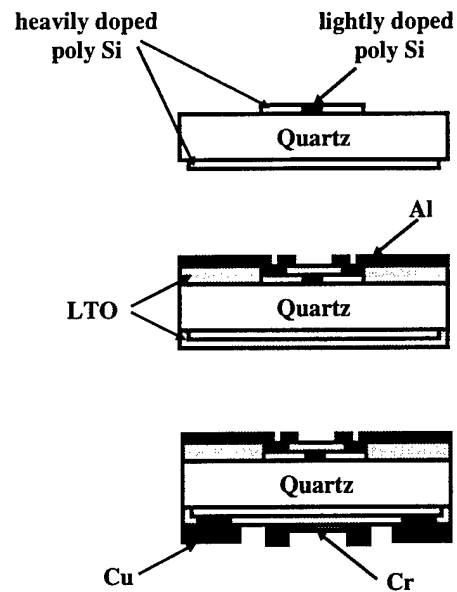
Figure 2.3.19. Quartz target sensor chip process flow.

Backside processing is then done with RIE that opens contacts through the oxide layer to the polysilicon. Then, a Cr/Cu metalization is done. Finally, the metal is patterned to define the heaters in the case of the quartz chip, or the backside sensors and heater in the case of the silicon chip.

2.4 Instrumentation

2.4.1 Experimental Setup

Figure 2.4.1 shows the experimental setup. The chip is mounted on a Plexiglas chuck for thermal isolation. The backside polysilicon heater has a nominal resistance of 55 Ω, and by varying the input voltage, we have a precisely controllable heat source using the Joule heating of this resistor. Most tests are conducted with approximately 1W of power. As shown, vacuum is always drawn on the backside of the chip to prevent downward heat loss. This is important because it is desirable to have all the heat transferred to the top surface. Above the sensor chip, filtered air is applied to drive an impinging-jet nozzle or array chip, which is then held above the sensor chip by an aluminum L-block that is attached to a 3-axis micro-positioner (Figure 2.4.2). The inlet air/gas system has sensors and valves to monitor and control the inlet pressure and the mass flow rate.

Each sensor on the chip is wire bonded to leads on a PCB mounted on the top surface of the Plexiglas chuck. The PCB is connected to a HP 34970A data acquisition system that has been set up to measure resistance. An environmental chamber is used to obtain sensor temperature calibration curves (second-order polynomial) used for data processing. These sensors are calibrated from room temperature to 80 °C.
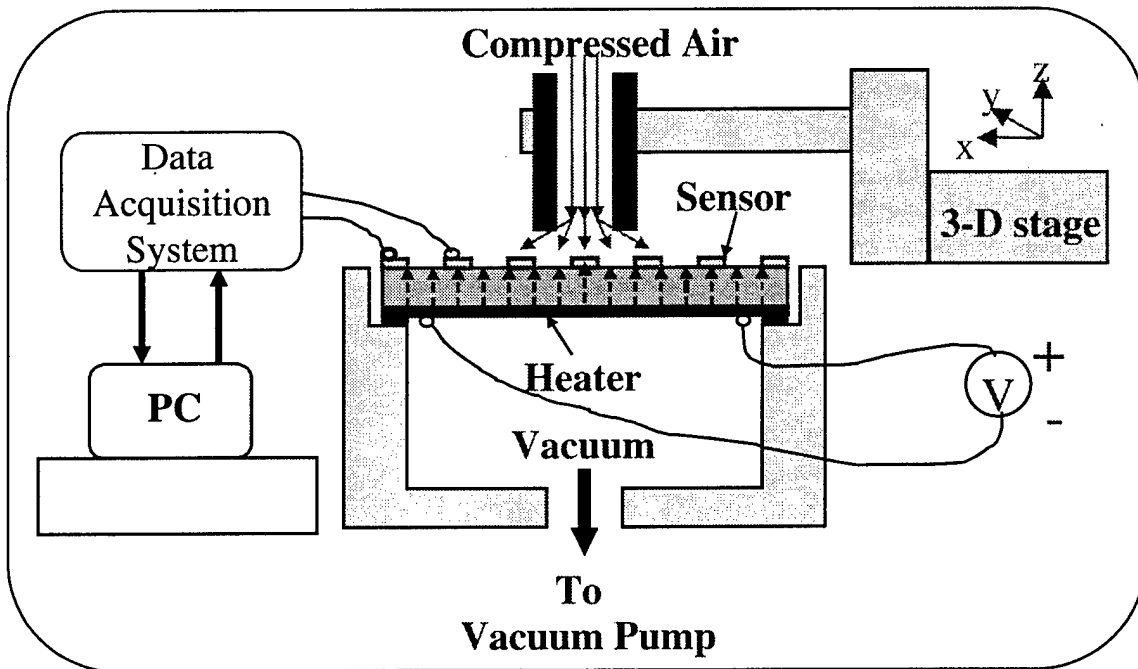
Figure 2.4.1. Experimental Setup.
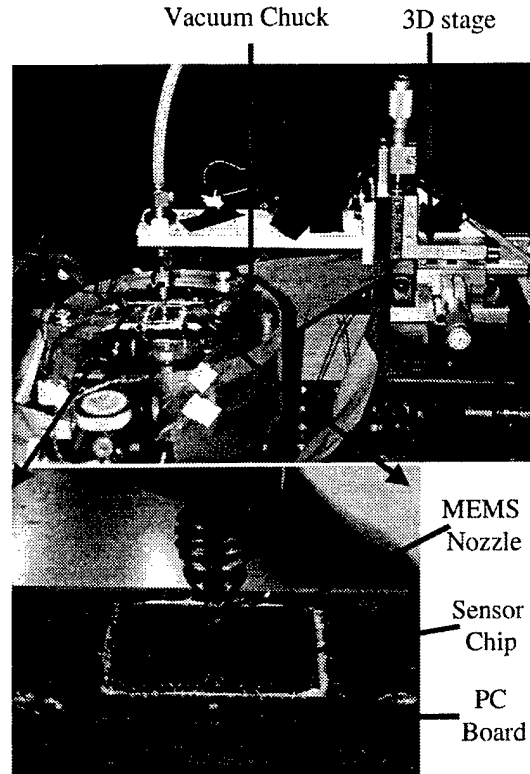
Figure 2.4.2. Picture of the experimental setup.

2.4.2 Constant Current Circuits

Circuits for Temperature Sensors

The original constant current circuit used to test the single sensor was simply a whetstone bridge with four similar resistances, with the differential output connected to an amplifier, as shown in Figure 2.4.3. The current passing through sensors is approximately 30uA. One problem with this simple circuit is the need for a very stable power source in order to achieve consistent measurements, so a new circuit designed with stable power supply is necessary for our application.
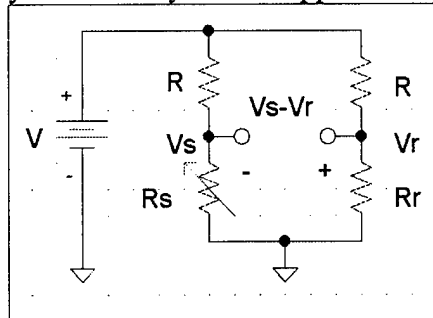
Figure 2.4.3. A bridge circuit for a temperature sensor.

Figure 2.4.4 is the circuit with the LM317 adjustable voltage regulator. An unregulated +15V can be inputted into LM317. The output voltage is controlled by the ratio of R1/R2, which in effects also controls the current. This highly stable voltage is then fed into a whetstone bridge. Above the sensor is a 1MΩ resistor that effectively appears to the sensor as a constant current source. This configuration is repeated on the other branches of the Whetstone Bridge but with a fixed 20kΩ resistor opposite to the sensor. An amplifier stage is not necessary since the ADC system has built-in preset gains.
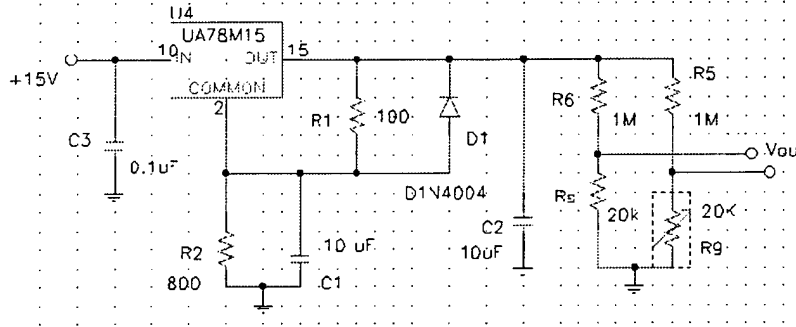
Figure 2.4.4. The constant current circuit with the LM317 adjustable voltage regulator

1st Generation Circuit for the Silicon Temperature Imager

Figure 2.4.5 shows the 1st Generation Circuit for the silicon temperature imager. The voltage divider on the left side sets the base bias voltage for the transistors. The voltage follower (Op-Amp) is used to buffer the rest of the circuit, from which the constant current is provided. The output of the operational amplifier can supply a very stable voltage regardless of changes in load (sensor resistance >> Z_{output}). The voltage across the emitter resistor and the base-emitter line of every PNP-transistor thus stays constant. If the base-emitter voltage (V_{BE}) is assumed to be constant (V_{BE} =0.6V), the voltage across the emitter resistor is also constant. This provides a constant emitter current (I_E) and, by neglecting the little base current (I_B) it also provides a constant load current (I_C).

With this circuit all the nodes can share a common potential. Another advantage is that the potentiometer, needed to adjust the current I_C, is used only once which decreases calibration effort.

To provide a current I_E=20μA, the voltage across the emitter resistor (U_{RE}) is chosen to be about U_{RE}=7V. This will provide a very stable current (the higher this voltage, the more stable the load current). To maintain the required value of I_E=20μA, the value for the emitter resistor (R_E) (e.g. R_4 in Fig. 2.4.6) is calculated to be

$$R_E = \frac{U_{RE}}{I_E} = \frac{7}{20 \cdot 10^{-6}} = 350 k\Omega$$

By using two resistors in parallel (1 MΩ and 500 kΩ), the overall resistor value of R_E=333.3kΩ is obtained. The actual voltage (V_E) calculates to be

$$V_E = +15V - R_E \cdot I_E = 15 - 333.3 \cdot 10^3 \cdot 20 \cdot 10^{-6} = 8.3V$$

As mentioned earlier, the base voltage can be calculated to be

$$V_B = V_E - 0.6 = 8.3 - 0.6 = 7.7V .$$

The values of the resistors for the voltage divider are calculated to be R_1=R_2=68kΩ. The potentiometer (POT-R_3) is chosen to be 10kΩ. Thus the requested value of (V_B) is within the adjusting range of (R_3).
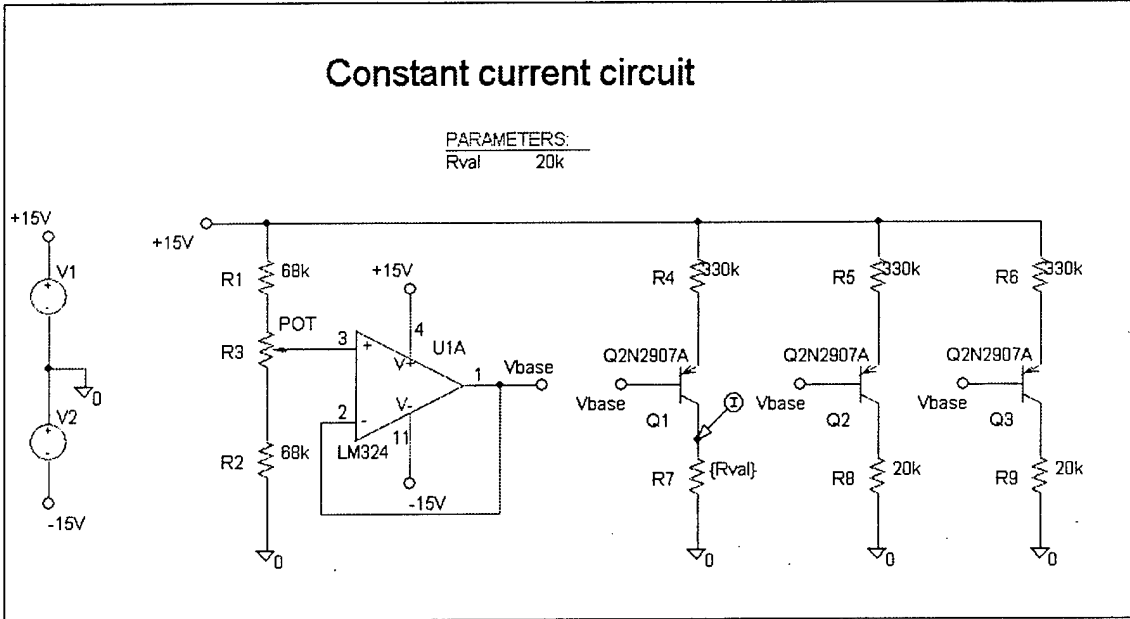
Figure 2.4.5. 1st generation constant circuit used in the silicon temperature imager.
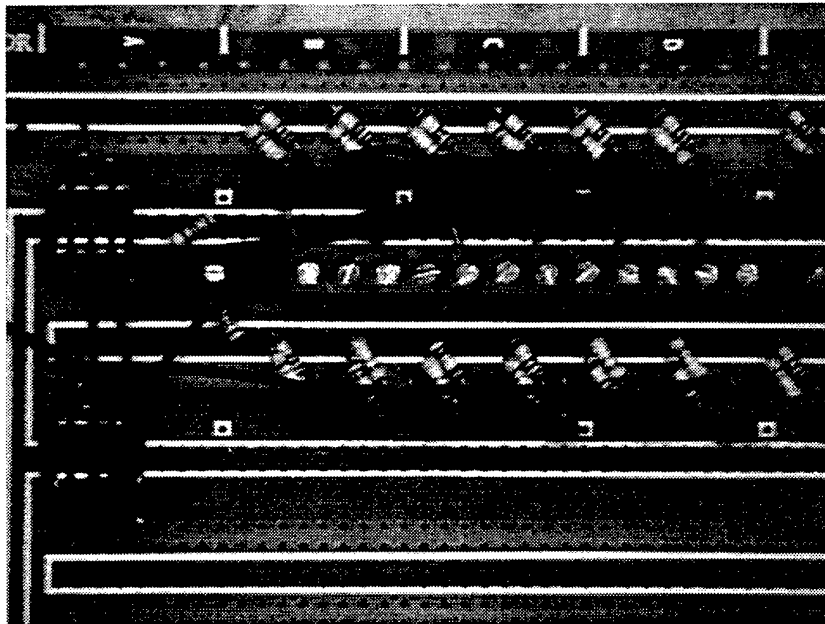
Figure 2.4.6. The picture of 2nd generation constant circuit.

Since there is a rather large number of channels (64) driven by one voltage follower, the issue of achievable output current has to be discussed: One OpAmp output can sink a maximum output-current of about 20mA. If there is a load with very high resistance, the transistor will operate in the saturation region, meaning that the emitter-collector voltage (V_{EC}) is lower than about 0.3V. In this operation mode, the base current can no longer be neglected. If even the load resistance is infinite, i.e. no sensor is connected to the transistor, the base current becomes equal to the emitter current: $I_E = I_B$. If too many of the sensor- collector junctions are left open, the OpAmp will no longer provide the stable voltage. The base voltage will drop, and the output current will no longer remain constant. In order to avoid this situation, one operation amplifier is for at most 10 sensors as shown in Figure 2.4.6. With this design, such improper operation will not occur.

2nd Generation Circuit for Silicon and Quartz Temperature Imagers

In our setup for the silicon and quartz temperature imagers, we used the LM334 constant current source IC and IC current mirrors to provide constant current bias to the sensors (as shown figure 2.4.7). Since the LM334 has a positive tempco, we used an extra resistor and diode to cancel out the temperature drift. R1 and R2 set the current for the IC. Detail information can be found in the LM334 data sheet provided by National Semiconductor. The CC circuit, the C50 data acquisition board (14 bit), and the sensors form a complete system with a resolution limited only by the LSB of the C50 board. The noise level is of order 1 LSB, which translates to a temperature resolution of at least 0.1°C.
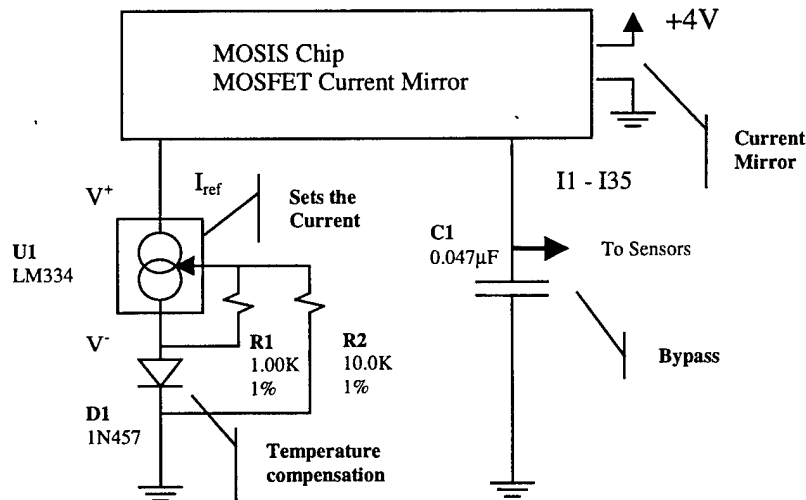
Figure 2.4.7. Conceptual diagram of 2nd generation constant current circuit.

2.4.3 Keithley DAS 1800 A/D Card:

The Keithley DAS 1800 A/D Card was used to take measurement data of single temperature sensor and silicon temperature imager in the beginning. The following configuration options were chosen:

- Single ended Mode: All input channels refer to the same ground, there are several grounding modes possible.
- Bipolar: In order to check possible connection errors as soon as possible (negative output).
- Low Level Ground Mode: Chosen grounding mode.
- Internal settings: IRQ #5, DMA #5.

The configuration for the VTX software has to be done in MS-DOS mode to configure the drivers for the data acquisition card and further, must be done in Windows 95 mode. Otherwise improper operation can occur. The correct operation of the card can be confirmed by running the Keithley Control Panel. This program allows the user to test distinct channels.
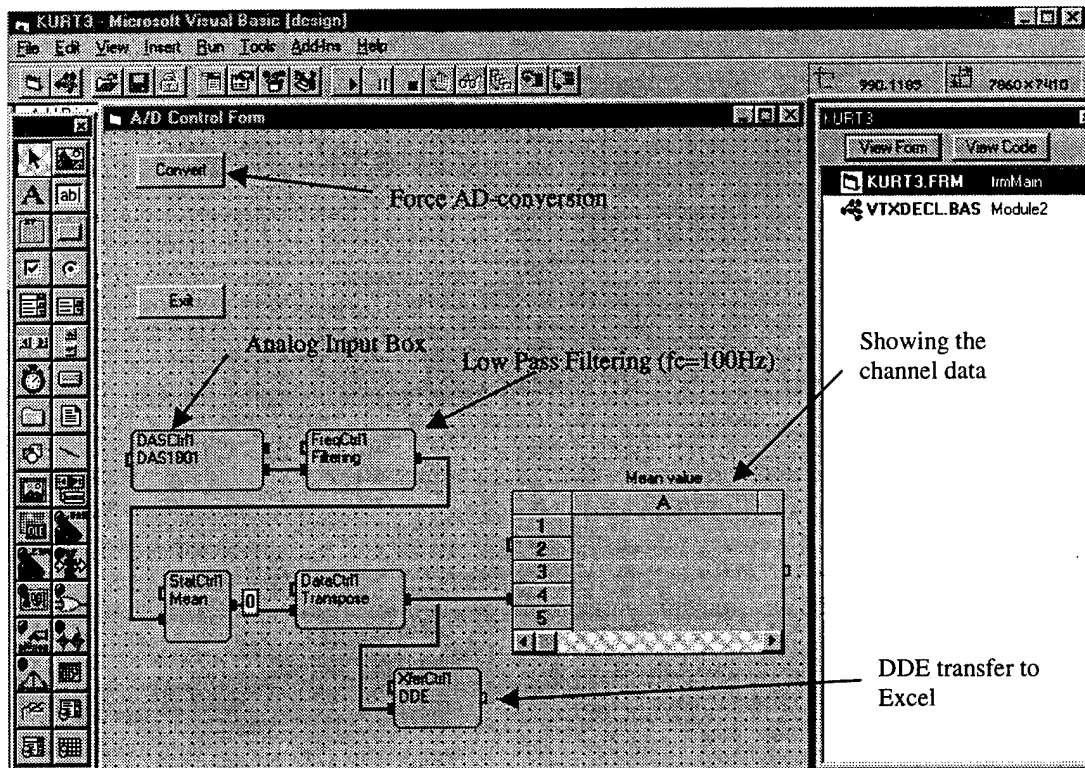
Fig. 2.4.8: Control Form in Visual Basic Developer Studio for data acquisition

Once all the channels are configured correctly, singles block "Analog Input" can be inserted in the Program Form to retrieve data from a particular channel of the Keithley board in Visual Basic. Fig. 2.4.8 shows the A/D Control Form for the Visual Basic data acquisition program.

The Convert-button forces data acquisition to occur. The Analog Input block, takes 100 samples in one conversion period from every channel. From these values the mean is calculated. In some applications it can be useful to feed the incoming signal into a lowpass filter in order to eliminate high frequency interference.

Having created a row vector of input voltages (with the Transpose block), this vector is further automatically passed to a worksheet in MS-Excel. In this way, with each conversion of the ADC, a new row in the Excel worksheet is created.

This data acquisition program is very simple, yet it improves the process of measuring considerably. After running the program, the data can conveniently be processed in the Excel Worksheet. This will be described in the next section.

2.4.4 HP 34970A Data Acquisition System

HP34970A data acquisition/switch unit (as shown in Figure 2.4.9) was used to sample experimental data for the sensors on a temperature imager. Along with three HP 34901A channel multiplexers (as shown in Figure2.4.10), it can scan as many as 60 channels.

Figure 2.4.9. HP34970A data acquisition/switch unit

By HP BenchLink Data Logger software, a PC will control the HP data acquisition system and store sampled data into its hard disk. The system can be

configured to measure voltage, current and resistance. It has 6.5-digit (22bits) DMM and 0.01% basic 1-year accuracy.
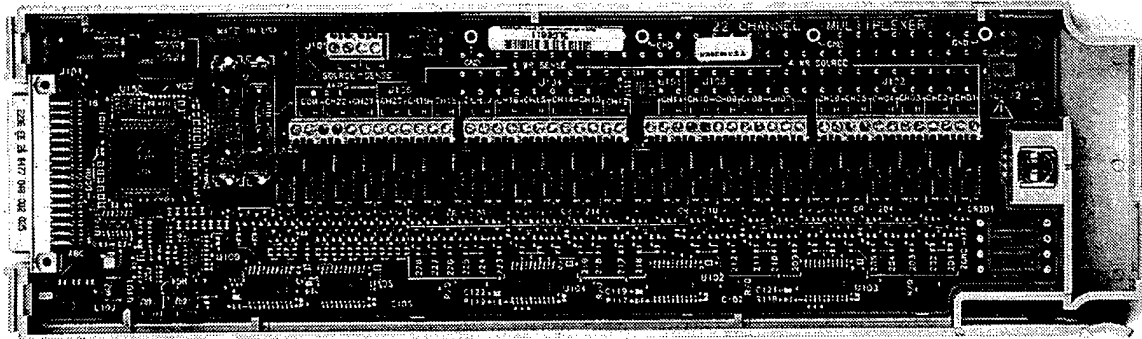
Figure 2.4.10 HP 34901A 20 Channel Multiplexer (2 / 4 -wire).

2.4.5 200-Channel Data Acquisition System.

200-Channel Data Acquisition System has been built in Caltech Micromachining Laboratory. Figure 2.4.11 is the block diagram of the data acquisition and control. As many as 200 sensor outputs are multiplexed and input to a high-resolution (14 bits) A/D converter. The digitized signal data points for each sensor are transfer to store in a PC which also control the whole system. This system has faster speed and provides more available channels than HP34970 system.
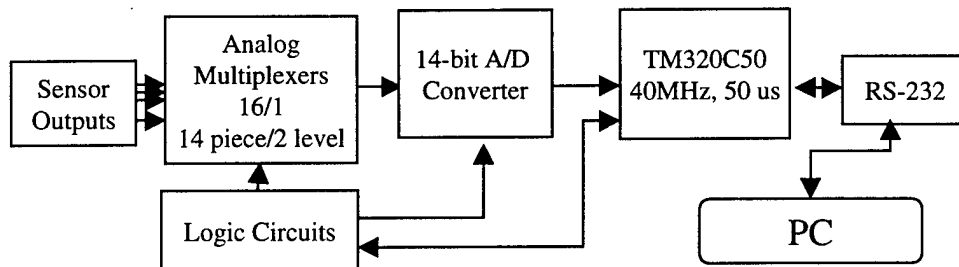
Figure 2.4.11. The block diagram of the 200-channel data acquisition system.
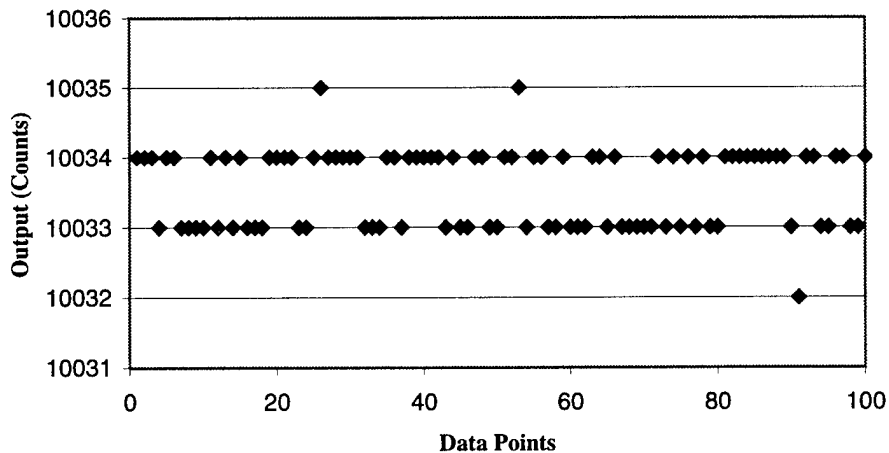
Figure 2.4.12 System output noise level by measuring battery voltages.

Figure 2.4.12 shows the ystem output noise level below ±1.5LSBpp (±0.4 mVpp) or 1LSBrms (0.25 mVrms) of the 14-bit A/D converter with a input range of 0 – 4 V. This is good enough for us to achieve the temperature resolution better that 0.1°C.

2.5 Heat Transfer Test Data and Discussion

2.5.1 Heat Transfer of 1st Generation MEMS Single-Nozzle and Array Jets with Silicon Temperature Imager

A single glass nozzle, a MEMS single nozzle, a MEMS nozzle array and a MEMS slot array were tested at a height range from 100 μm to 3000 μm and a pressure range from 0.5psi to 5psi.

Temperature Distribution Measurement

Temperature distribution measurements must be performed first to confirm the functionality of the sensor chip by using a MEMS single jet which is 750 μm away from the sensor chip and driven by 2 psig compressed air. Fig. 2.5.1 shows some typical data imaged in this fashion. The sensor chip must be able to identify and track the jet as it is moved around as in Fig. 2.5.1. Otherwise, the chip does not function properly.

(a) Jet on the left   (b) Jet at center   (c) Jet on the right
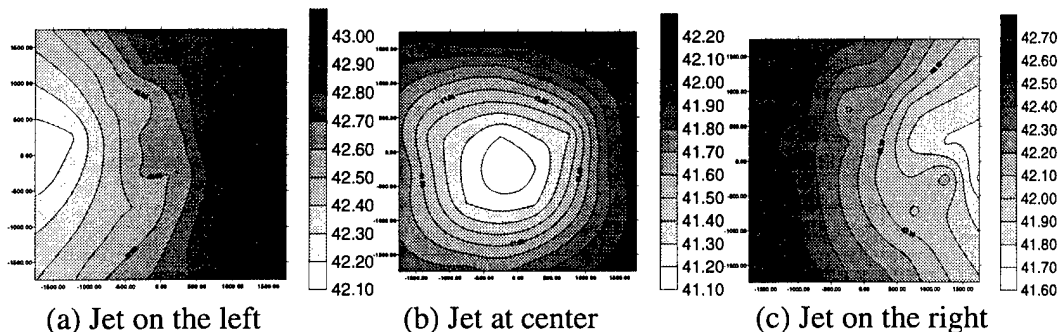
Figure 2.5.1. Contour temperature plots indicating that the sensor image correctly identifies and tracks an impinging jet.

Single Impinging-Jet Cooling

Figure 2.5.2 is a composite of the sensor chip temperature profiles constructed from instantaneous sensor array data for each of the three cases. First, the temperature profile, shown as the bottom plane, was measured in the room temperature without any heating and cooling. The uniformity (±0.1 °C) of the measured temperatures from time to time shows good system reliability. The top plane is the temperature profile measured with 1.12 W applied via the backside heaters and no cooling on the frontside. The uniform temperature implies heat was evenly generated by the MEMS heater across the chip. The middle plane is the temperature profile under cooling by a 500 μm diameter MEMS

28

nozzle which is 750 µm above the surface and driven by 5 psi compressed air . A large total temperature drop (>35 °C) after the applied cooling shows the high cooling efectiveness by a impinging jet. A small temperature variation across the sensing area implies a large effective cooling area, enough to cause a measureable temperature profile even considering the large thermal conductivity of silicon.
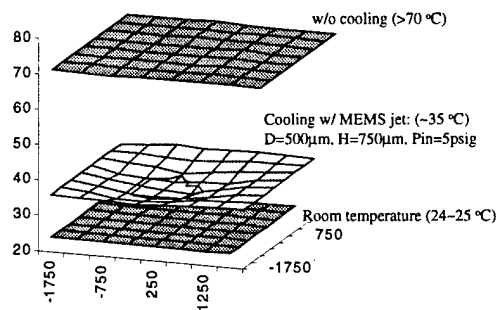
Figure 2.5.2. Composite illustration showing the effectiveness of impinging jet cooling.

Utilizing the silicon target sensor chip, temperature distributions at various nozzle heights and inlet pressures were obtained. Figure 2.5.9 is a sample temperature distribution taken with a 1st generation silicon target chip. These surface temperature distributions were then used as boundary conditions in numerical simulations, using the finite element analysis code ABAQUS, in order to calculate the local heat flux which, in turn, could be used to calculate the local heat transfer coefficient, h. As illustrated in Figure 2.5.3, it is known that the MEMS jet is 500um in diameter and 750um above the target surface. The inlet pressure is 5 psig and there is a controlled heat flux of 1.12 W into the entire 4 cm^2 area of the 1st generation silicon target chip.
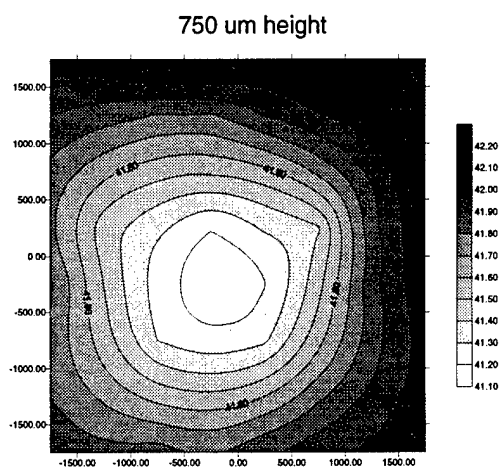
Figure 2.5.3. Sample surface temperature profile and computed local heat transfer coefficient based on the surface temperature data.

Figures 2.5.4 and 2.5.5 show the average temperature vs. spacing between a jet and the sensor chip at different air pressure conditions. The backside heater powered by

8V gave about 1.12W of heat generation. The surface temperature distribution due to the free jet at various heights is relatively stable. This is due to the fact that the free jet can easily entrain local cold air and circulate it over the heated test chip. In the case of the MEMS jet, it is more of a confined jet situation. Since the MEMS jet is a hole fabricated into an approximately 4 mm by 4 mm silicon chip, at heights less than 1mm the top wall combines with the bottom sensor chip to produce a channel flow effect. This reduces the volume of cold air available next to the MEMS nozzle to be entrained and circulated past the heated bottom chip. These leads to a higher measured surface temperature for similar height and pressure conditions when compared to the free jet. However, at larger heights, this confined flow effect is greatly reduced and the MEMS jet cooling effectiveness is comparable to the free jet, as evident by the heat transfer coefficients calculated in Figure 2.5.6 for the MEMS jet. The heat transfer coefficient for the free jet is approximately constant at 0.032 W/cm^{2}K at 5 psi and 0.025W/cm^{2}K at 3 psi. Thus the MEMS jet (with an approximately 16 mm^2 chip area) has similar cooling characteristics to a free jet when the H/D ratio is greater than 3. Comparison of Reynolds numbers indicates the observed results agree with the expected flow regime. The Reynolds number for H/D less than 1 for the MEMS jet should scale with the height since it is now the minimum opening in the system. These yield values of Re as low as 1300, which is in the lower end of the transition region near laminar flow, which is known to have poorer heat transfer qualities than turbulent flow.
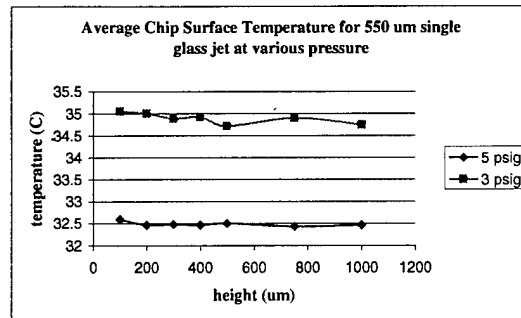
Figure 2.5.4. Average sensor chip temperature at various heights for a given inlet pressure of a single jet.
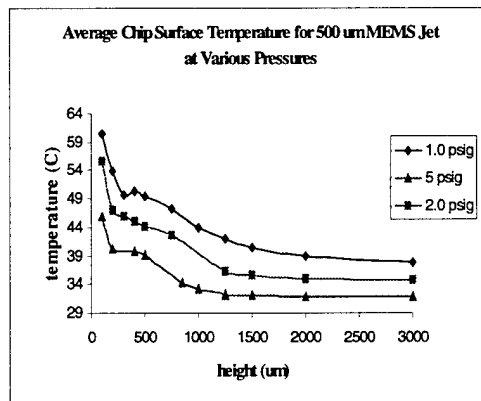
Figure 2.5.5. Average chip temperature at various heights for a 500 μm diameter. MEMS single nozzle.

30

Jet cooling efficiency, defined as heat transfer coefficient normalized by the kinetic energy of the impinging gas, has been calculated and plotted in Figure 2.5.6 and 2.5.7 show for the single free jet and MEMS jet respectively. For both types of jet, a low gas driving pressure gives a high cooling efficiency. This gives us a practical guide for cooling system design: Low gas pressure is preferred if the gas source and power limitation is the constraint. Otherwise, high pressure and high speed jets can be used to achieve low surface temperature.
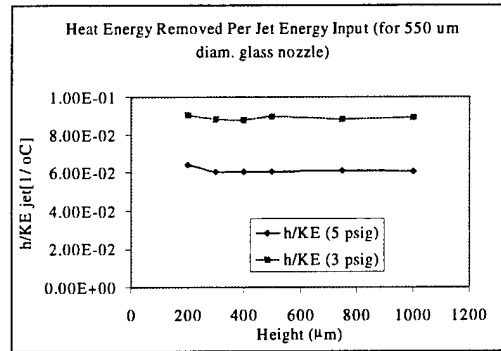
Figure 2.5.6. Cooling efficiency at various heights for a given inlet pressure of a free single jet
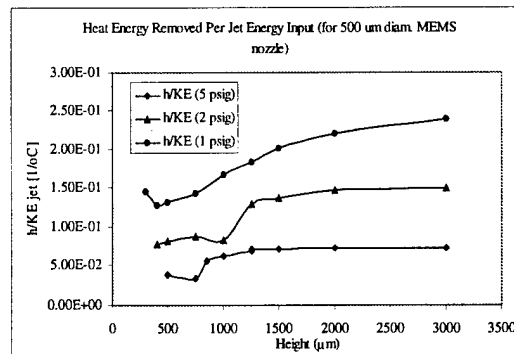
Figure 2.5.7. Cooling efficiency at various heights for a given inlet pressure of a MEMS single jet

MEMS Jet Array

Preliminary data images with a nozzle array and slot array are presented in Figures 2.5.8 and 2.5.9. Although the temperature images are not as simple as the image of a single jet because of the more complicated gas flow pattern, the temperature distribution is more uniform than any single jet.

There seems to only be one major minimum in temperature. This is due to the fact that the 2 mm gas inlet on the backside of the chip is centered only over the center exit jet in each row. Since there is only 1 temperature sensor every 500 μm, we do not have enough spatial resolution so most of the exit flow from the 2 center jets appear as a single larger elliptical impingement region.
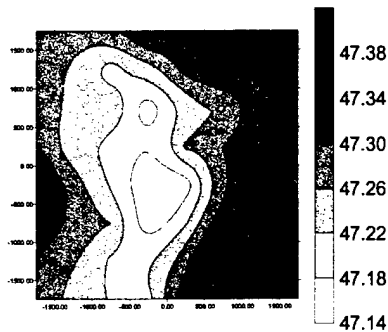
Figure 2.5.8. Temperature distribution recorded from a nozzle array at 500 μm height, Pin = 0.5 psig, and power in = 1.12 W.
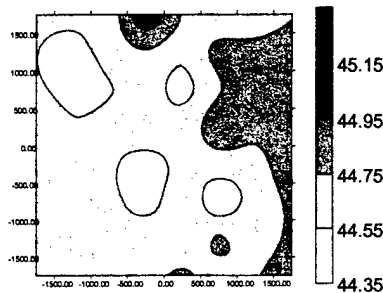
Figure 2.5.9. Slot array temperature distribution at height = 1000 μm, Pin = 1 psig, and an input power of 1.12 W.

The slot nozzle data in Figure 2.5.9 also indicates peculiarities in the prototype nozzle design. It seems that the inlets are acting as nozzles and the slots serve to confine the flow along the slot direction. According to turbulent impinging jet theory, boundary layer flow separation and recirculation can occur 2 nozzle diameters down from the centerline inlet. This region can give rise to secondary maximums in heat transfer. The smaller cool regions correspond to this location. The lack of symmetry in the secondary cooling peak can be explained by the fact that the inlet is not precisely aligned with the exit slots, so the jet from the inlet is deflected, creating an oblique exit jet which is then confined by the slot. Hence there should be local secondary minimums on the left side, but they appear to be on the low momentum side of the oblique jet so separation occurs at a larger distance away from the impingement point, which is out of the sensor area.

In practice, cooling fans can only provide a limited pressure gradient for electronic cooling. Since it is assumed that standard PC-level cooling fans will be eventually interfaced with these MEMS devices, in practice, it is reasonable to evaluate cooling effectiveness by comparing surface temperature as a function of inlet pressure, irregardless of total mass flow rate. With this consideration in mind, a quick comparison method between the single nozzle and nozzle array is available, as evident in Table 2.5.1.

From Table 2.5.1, it is apparent that if one design parameter is a small available pressure drop, then a MEMS nozzle array is the optimal cooling configuration

32

	Single MEMS Jet	Single Glass Jet	Slot Array	Nozzle Array
Gas Pressure (psig)	2.0	1.0	0.7	0.5

Table 2.5.1. Comparison of pressure required to cool the test chip to approximately 47 °C with Q = 1.12 W and height = 500 μm.

2.5.2 Heat Transfer of 1st Generation MEMS Single-Nozzle and Array Jets with the Quartz Temperature Imager

The heat transfer measurement using the silicon target chip, as described in Section 2.5.1, yielded interesting results. However, the Section 2.5.1 results also indicated that the silicon target chip did not provide sufficient information on the temperature distribution because of the limited area covered by the sensor array. In addition, the high thermal conductivity of silicon made the temperature gradients in the chip rather small, significantly reducing the relative precision of temperature measurement. In view of these observations, we designed and fabricated a quartz temperature imager, as described in Section 2.3.7, and used it to perform further measurement of impinging-jet heat transfer with the 1st generation MEMS single nozzle and nozzle arrays.

Single-Jet Results.

The temperature distribution on the top surface of the quartz target chip has been measured. Compared with measurements with the silicon target chip, this data is available in a larger area of the quartz chip's top surface (1 cm x 1 cm), and is highly indicative of the jet nozzle geometry. Figure 2.5.10 shows temperature contours on the front side of the quartz chip under MEMS single-nozzle jets, respectively. The local heat transfer versus radial distance from the impingement point has been computed and is graphed in Figure 2.5.11, for different H/D ratios at an inlet pressure of 0.6 psig. Similar trends were observed at other jet inlet pressures. These results show that for localized cooling within the diameter of the nozzle, the MEMS impinging jet results offer an order of magnitude improvement in heat transfer rate over a conventional (larger diameter) impinging jet. From Figure 2.5.12, which plots the local heat transfer for various inlet pressures at a jet height of 0.75 mm, h increases at higher jet velocities as expected. As shown in Figure 2.5.10(a), the chip surface temperature for H=1 mm possesses poor axisymmetry beyond a smaller radial distance (1 mm) from the jet center, and the temperature profile is indicative of the square shape of the MEMS nozzle chip's boundary. As H increases to 1.5 mm, the axisymmetry of the temperature profile improves significantly. This quite clearly demonstrate the confinement effects between the surfaces of the temperature imager and MEMS nozzle chips. Figure 2.5.11 shows that as H increases from 0.75 mm to 1.5 mm, the heat transfer coefficient increases. This

phenomenon would seem to indicate that at this geometry, the beneficial effects of colder fluid entertainment couples favorably with the excess total fluid momentum near the impingement point to penetrate the boundary layer in order to transfer the hotter fluid away from the surface.

(a)   (b)
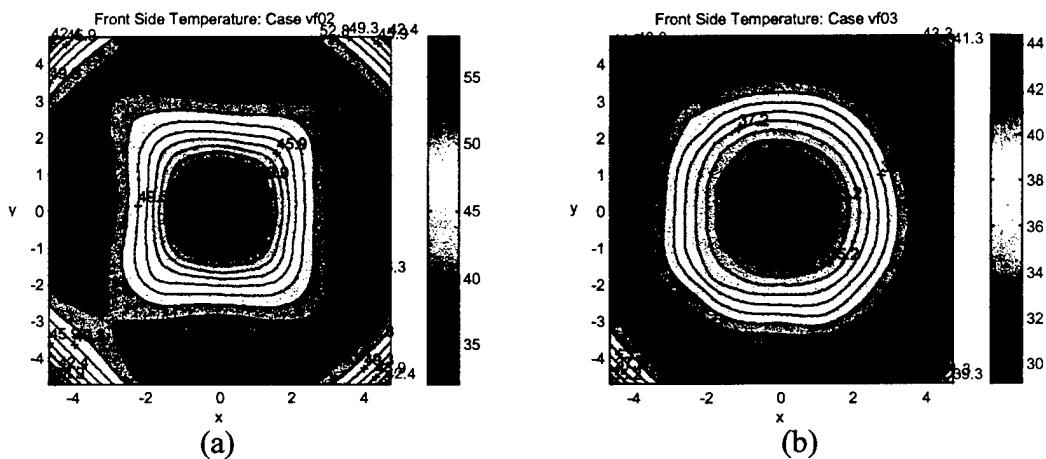
Figure 2.5.10. Surface temperature profiles of a 1st generation MEMS single jet (p=0.6 psig) measured using the quartz temperature imager. (a) H = 1 mm; (b) H = 1.5 mm.
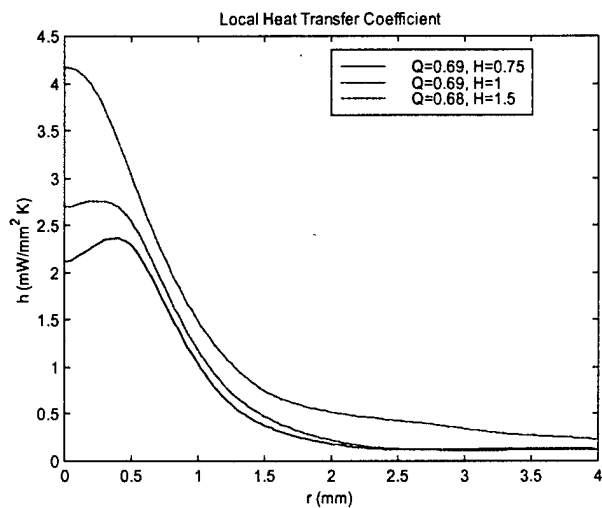
Figure 2.5.11. Radial local heat transfer coefficient for different values of H/D.
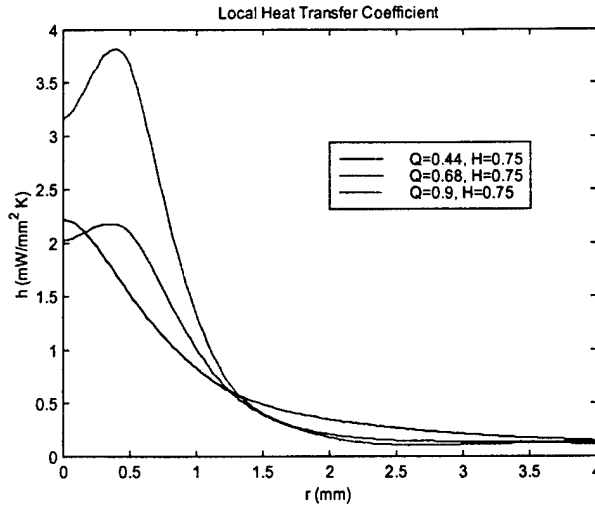
Figure 2.5.12. Radial local heat transfer coefficients for different inlet pressures.

Capillary-Jet-Array Results.

From previous experiments that compared a MEMS confined jet configuration with a glass free jet configuration, the increased heat transfer benefits of fluid entrainment were observed. An improved impinging-jet array design that incorporates the advantages of free jet entrainment is shown in Figure 2.5.13. This impinging jet array is seven, 540um-inner-diameter, capillary tubes bundled together. This capillary jet array design was able to decrease the target chip temperature locally to less than 27 °C at a total jet mass flow rate of 3.08 slpm, at a height of 1.0 mm above the target chip. With a power of 0.866W applied to the chip, this gives a thermal resistance of 2.3°C/W for this situation. This is much better than the cooling provide by commercial PC fans, which typically have thermal resistances on the order of 10 °C/W. The instantaneous quartz target chip temperature profile for this situation is plotted in Figure 2.5.14.
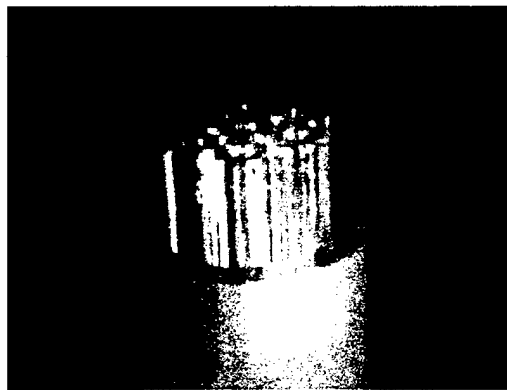
Figure 2.5.13. Seven capillary tubes bundled together to form a jet array.
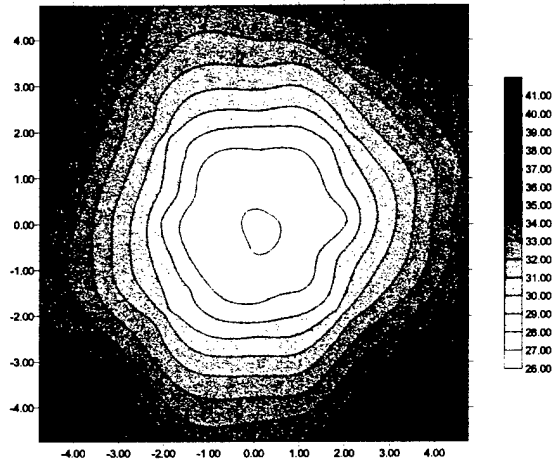
Figure 2.5.14. Temperature distribution of the capillary jet array, as measured by the 2nd generation quartz chip.

1st Generation MEMS Impinging Jet-Array Results

Using the quartz temperature imager, we measured the temperature distribution on the imager chip's front side, which was under the impingement of a 1st generation MEMS jet array. Figure 2.5.15 displays the temperature distribution for a 2x3 MEMS jet array. We can see that the temperature distribution is rather non-uniform. Meanwhile, Figure 2.5.16, which shows, h, the heat transfer coefficient distribution over the chip surface, indicates that h is also rather non-uniformed distributed – in the region bounded by the nozzles, the value of h is considerably smaller than in the regions near the nozzles. It is suspected that the confinement effect of the flow in the nozzle-bounded region contributed significantly to the non-uniformity. While the contours in Figure 2.5.16 clearly shows the presence of 6 nozzles, the heat transfer associated with the nozzles in not even. We believe that the most important reason for this unevenness is that the air actually flows through a complicated path from the inlet to the outlet the array nozzles, which differs for different nozzles and causes uneven air flows through these nozzles. The peak value of h under each nozzle ($\leq$ 1.5 mW/mm^{2}K) is much smaller than that achieved by a single-nozzle jet with a comparable flow rate (see the curve in Figure 2.5.11 for Q = 0.69 SLPM and H = 1 mm). This appears to be due to the unfavorable interference between jets from neighboring nozzles. As will be demonstrated in Section 2.5.3, our improved nozzle array design offers significant improvement in these aspects. In fact, favorable interference between jets from adjacent nozzles have been observed with the new nozzle design.

36
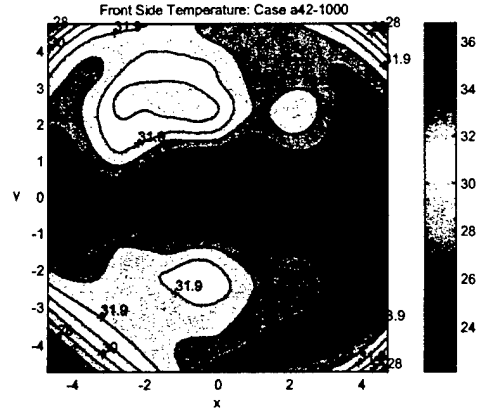
Figure 2.5.15. Temperature distribution on the front side for a 1st generation 2x3 MEMS jet array.
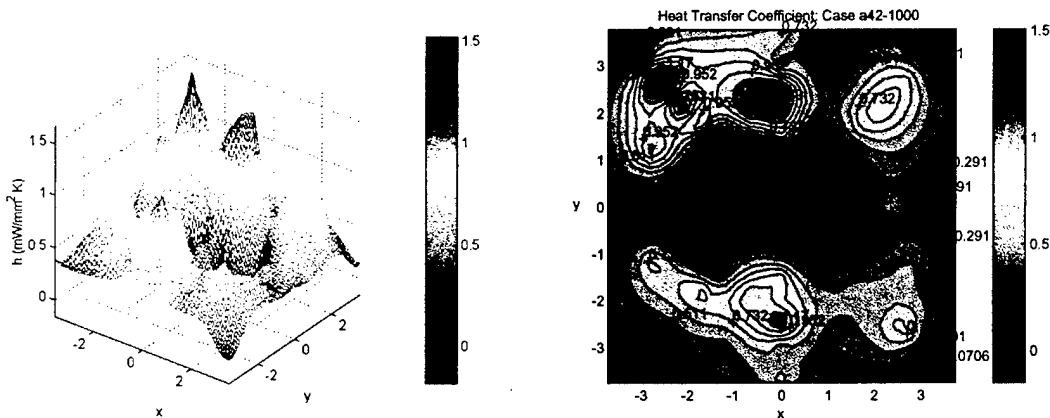
Figure 2.5.16. Heat transfer coefficient for a 1st generation 2x3 MEMS jet array.

2.5.4 Heat Transfer of 2nd Generation MEMS Single-Nozzle and Array Jets with the Quartz Temperature Imager

2nd Generation Single Jet Results.

The temperature sensors give the imager chip's frontside temperature, T. The single-jet temperature measurement data have been processed with a more accurate method. This method determines the axisymmetric temperature distribution on the front side of the temperature imager due to single-jet impingement by a least-squares curve fitting using cubic splines. Since the precise location of the jet center is not known, we start with a guessed jet center location. The radial distances from the temperature measurement points to the guessed center location are computed, and a least-squares cubic spline curve fitting is performed to these data points under the constraint that the slope of the temperature distribution vanish at the guessed jet center. The root-mean-square error of this fitting is then computed, and used to determine an improved jet center location. A new fitted curve is then obtained with a smaller fitting error. This process is iteratively repeated until the fitting error is minimized.

The axisymmetric front side temperature distribution, obtained from the above iterative curve fitting scheme, is used along with the known back side uniform heat flux to compute the heat flux from the chip's front side to the jet. This information is finally used to find the jet-impingement heat transfer coefficient h. The ABAQUS finite element package is again used in the computation.

The results are shown in Figs. 2.5.15-2.5.22. For single-jet impingement, Fig. 2.5.15 displays the temperature distribution for p = 0.6 psig (comparable with that shown in Fig. 2.5.10) and H = 0.5 mm. It can be seen that at H = 0.5 mm, which is much smaller than the jet height of 1 mm used in Fig. 2.5.10, the temperature is quite axisymmetrically distributed. This demonstrate that the new nozzle design is quite successful in addressing the asymmetry which is significantly present in the 1st generation nozzles. Axisymmetry is important for heat transfer analysis of jets emerging from round nozzles, and is also useful for the nozzles to be used to produce jet arrays. Fig. 2.5.16 depicts a 3D plot of h over the chip surface. The variation of h with the distance from the jet center, r, is shown in Figs. 2.5.17 and 2.5.18 for different pressure drops (p) and nozzle-to-chip spacings (H), respectively. Fig. 2.5.19 illustrates the influence of H and p on the average heat transfer coefficient, h_{av}. Generally in agreement with macro-jet data [2], h is highly localized near the center, and its maximum shifts off center as p increases. Further, h (or h_{av}) is fairly insensitive to H, while increasing significantly as p is increased.
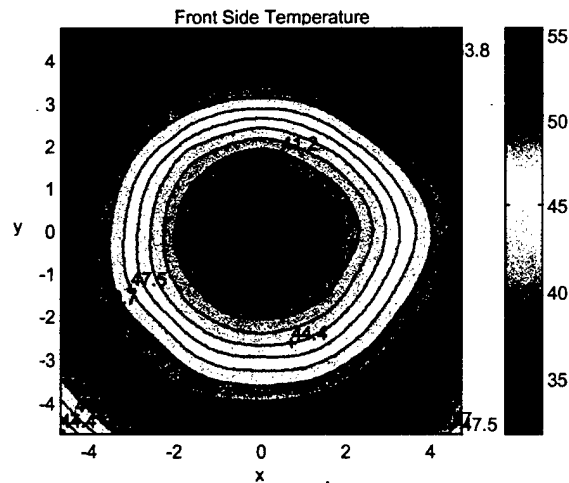
Figure 2.5.15. Temperature distribution for a 2nd generation MEMS single jet (p=0.6psig, H=0.5 mm).
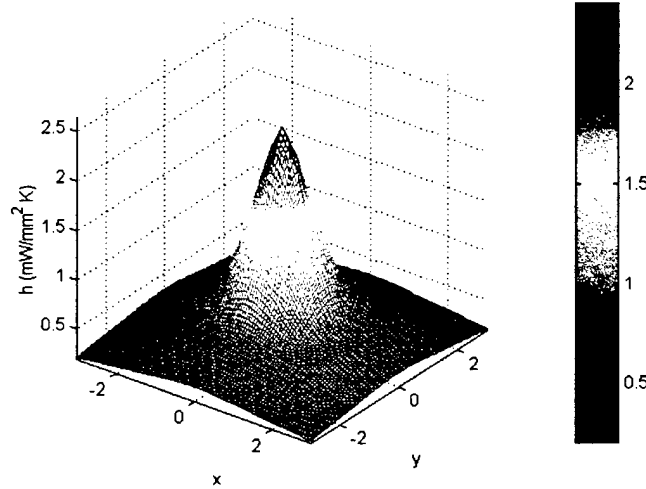
Figure 2.5.16. 3D plot of local heat transfer coefficient of a MEMS single jet (p=1.8psi, H/D=1).
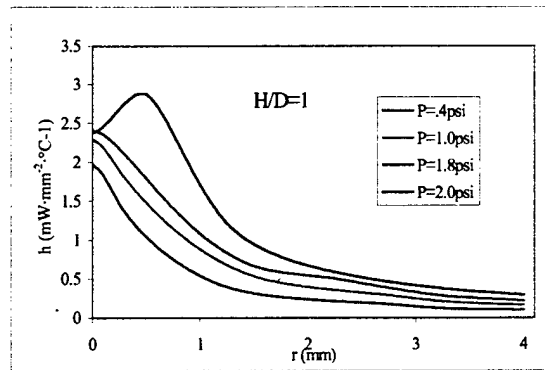
Figure 2.5.17. Local heat transfer coefficient of a MEMS single jet for different p.
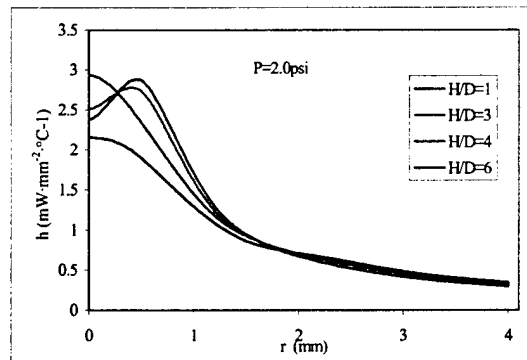
Figure 2.5.18. Local heat transfer coefficient of a MEMS single jet for fixed pressure for different H.
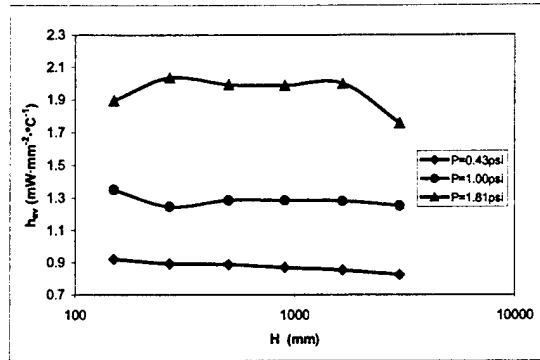
Figure 2.5.19. Average heat transfer coefficient of a MEMS single jet for different *p*.

2nd Generation MEMS Impinging Jet-Array Results

We have studied 2×1, 2×2 and 10×10 MEMS impinging-jet arrays. For the 2×1 array, the temperature and heat transfer coefficient distributions are displayed in Figs. 2.5.20 and Figs. 2.5.21, respectively. It can be seen that these distributions do bear the signature of a 2×1 jet array, possessing two extreme values at the nozzle centers. The dependence of the average heat transfer coefficient h_{av} on the jet-to-jet spacing, *a*, is shown in Figs. 2.5.24 and 2.5.25. It can be seen that h_{av} depends weakly on *a*, but increases with the flow rate *Q*. Moreover, contrary to the single-jet case, h_{av} also increases significantly as the nozzle-to-chip spacing *H* decreases. The interaction between the jets may have enhanced the heat transfer (this is also generally true for the 2×2 jet array, as will be shown below by Fig. 2.5.24). The temperature and heat transfer coefficient variations over the chip surface for the 2×2 jet array are shown in Figs. 2.5.22 and 2.5.23. These variations have 4 extreme values at the nozzle centers, and are again indicative of the characteristics of the 2×2 jet array. It is also worth noting that the temperature and heat transfer coefficient distributions are reasonably uniform across the region covered by the jet nozzles, and have comparable extreme values at the nozzle centers. This is a significant improvement compared with the performance of the 1st generation jet array as discussed in Section 5.2.2. For the 2×2 jet array, the heat transfer coefficient similarly increases with a decreasing jet height. However, there is an optimum between *H*=0.25 to 0.5 mm that gives the best cooling. Note that such favorable interference between adjacent jets is also in contrast to what was observed for the 1st generation jet arrays (see Section 2.5.2).

Finally, our preliminary investigation with the 10×10 jet array indicates that with a flow rate of 6 L/min one can achieve h_{av} =1 mW/mm² over the 1-cm² area covered by the array. This is 5 times the h_{av} value obtainable by a macro single jet of the same total nozzle area and flow rate. A sample heat transfer coefficient distribution over temperature imager chip surface is shown in Fig. 2.5.27.

In conclusion, with the second generation single nozzle and nozzle arrays and the quartz temperature imager, we have produced extensive microscale impinging-jet heat transfer data that have never been previously reported, and demonstrated the promise of heat exchangers that use MEMS impinging-jet arrays.

40
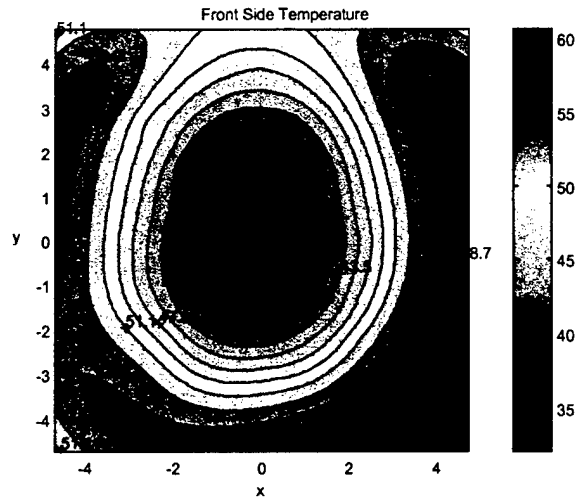
Figure 2.5.20. Temperature distribution for a 2x1 jet array (Q=1.4 SLPM, H/D=3.3, a=1.5mm).
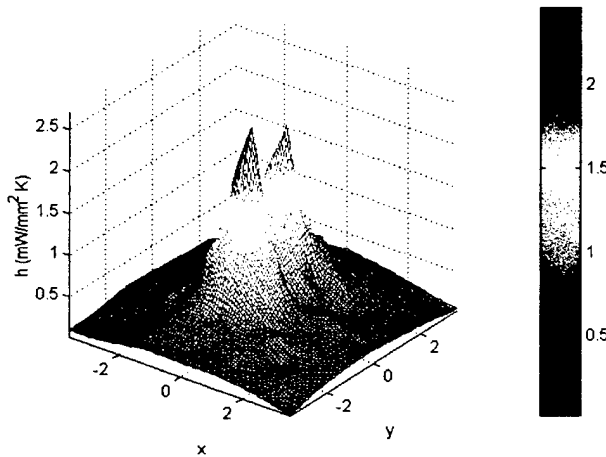
Figure 2.5.21. 3D plot of local heat transfer coefficient of a 2x1 jet array (Q=1.4 SLPM, H/D=3.3, a=1.5mm).
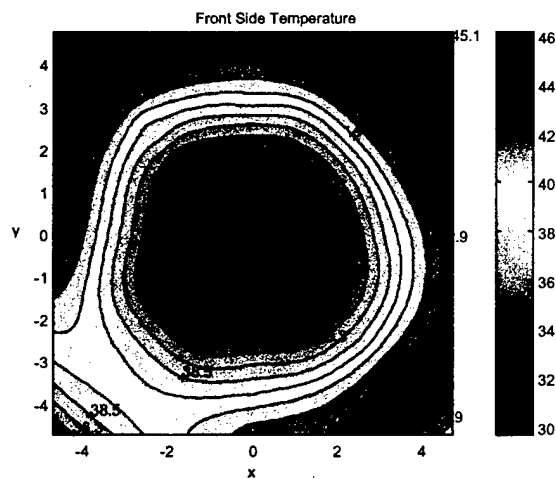
Figure 2.5.22. Temperature distribution for a 2x2 jet array (Q=3.3 SLPM, H/D=3.3).
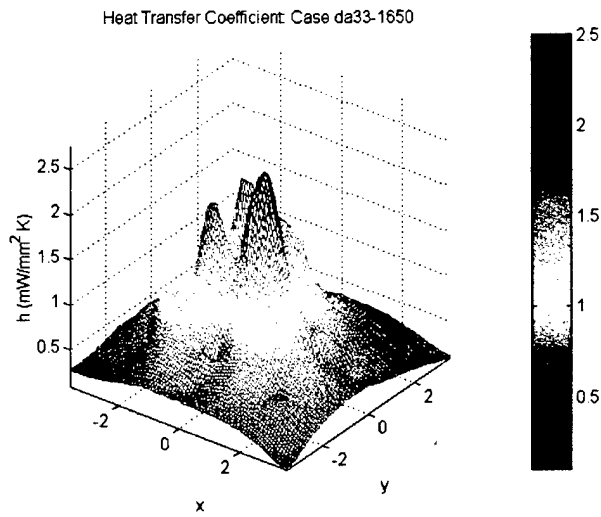
Figure 2.5.23. 3D plot of local heat transfer coefficient for a 2x2 jet array (Q=3.3 SLPM, H/D=3.3).
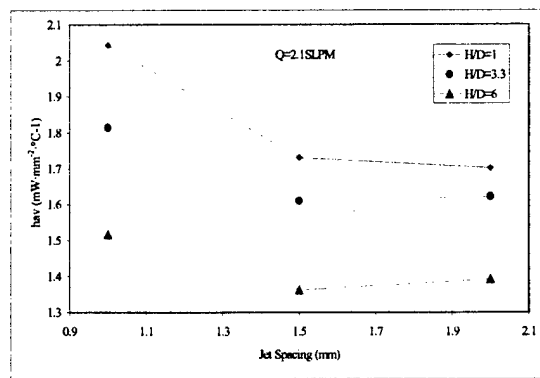
Figure 2.5.24. Average heat transfer coefficient of a 2 x 1 jet array for different H.
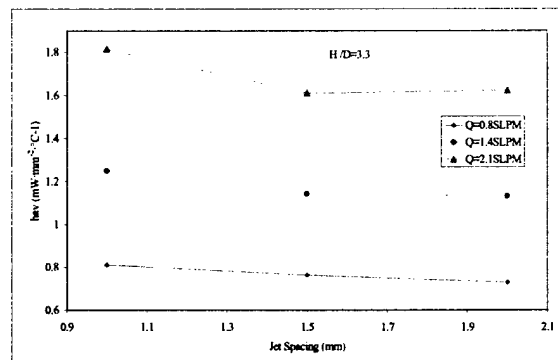
Figure 2.5.25. Average heat transfer coefficient of a 2 x 1 jet array for different Q.
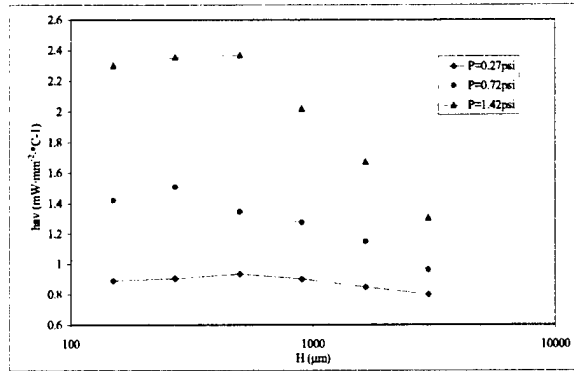
Figure 2.5.26. Average heat transfer coefficient of a 2 x 2 jet array for different p.
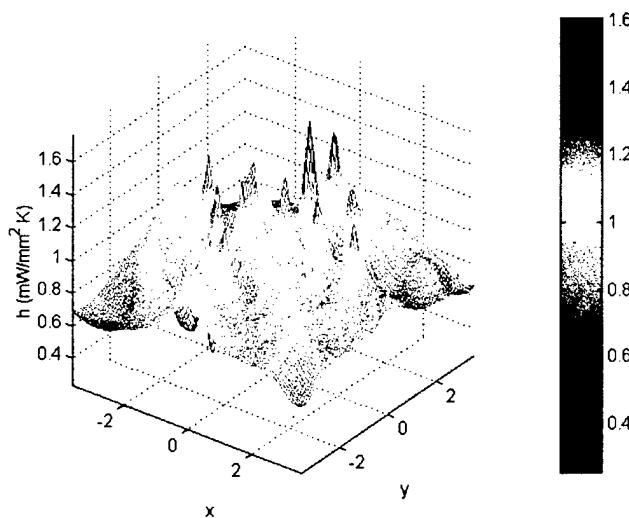
Figure 2.5.27. Average heat transfer coefficient of a 10 x 10 jet array (Q = 6 SLPM, H = 0.25 mm, P = 11 W).

2.5.4 Unsteady Measurements

As previously stated, for a steady flow, it has been found that a free jet geometry maximizes fluid entrainment which greatly improves the heat transfer coefficient. If the available inlet gas pressure drop and high power efficiency is a design constraint, then a MEMS impinging jet array with a low inlet pressure is the optimum configuration. Otherwise, a single MEMS jet can achieve a low surface temperature if a high inlet pressure is available.

We next attempted to utilize unsteady forcing of the jet flow in order to generate flow structures that would have an analogous effect on localized cooling, specifically by increasing local entrainment and mixing of hotter gas near the chip surface with cooler gas further way from the boundary layer. Unsteady temperature measurements have been taken of a nitrogen jet issuing from a MEMS nozzle and impinging onto the custom fabricated MEMS silicon target chip with an array of 64 integrated thermistor-type

sensors. Using a mechanical valve to perturb the flow at various static pressure amplitudes (0.05 psi to 0.36 psi peak-to-peak), and at frequencies from 20 Hz to 100 Hz, we tested a 500 um diameter MEMS nozzle positioned 500um to 1.5 mm above the surface.

Under specific applied pressure fluctuation conditions, the measured surface temperature over a wide region of the target chip is noticeably lower than the temperature at corresponding steady conditions. As seen in Figure 2.5.24, when a large amplitude (0.36 psi, peak-to-peak) pressure disturbance, at a 20 to 40 Hz low frequency actuation is applied, the measured temperature distribution radially from the impingement point is approximately 4°C less than the steady case, at the same average gas mass flow rate of 0.65 slpm . Figure 2.5.25 shows the expected decrease in absolute surface temperature in every situation (steady and unsteady) as the H/D ratio increases and more fluid entrainment is possible. In addition, the temperature difference between the steady and unsteady cases is also again observed in Figure 2.5.25 as the MEMS jet is raised from 500um to 1mm above the target chip. This would suggest a jet issued form a MEMS nozzle can be utilized to take advantage of flow instabilities that can lead to the generation of large-scale eddy or vortex structures, which are generally accepted as a major factor in improving localized convective heat transfer. [4]
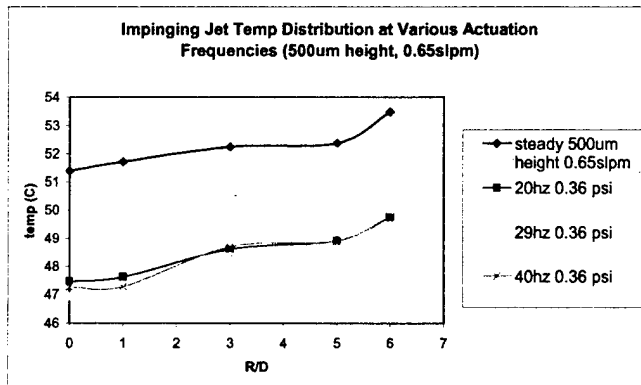
Figure 1. Steady and unsteady impinging jet temperature distribution at 500um height.
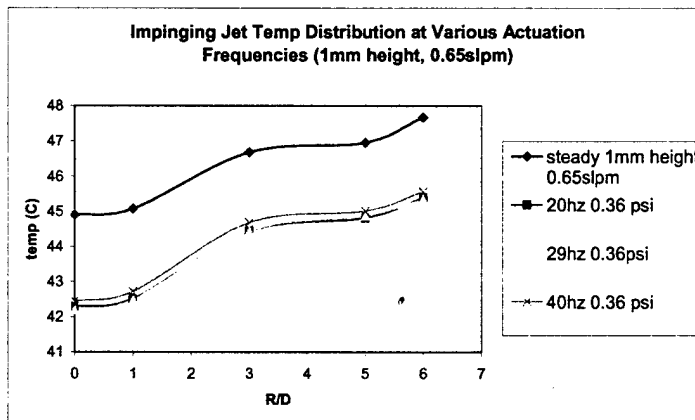
FIgure 2.5.25 Steady and unsteady impinging jet temperature distribution at 1mm height.

By changing the mass flow rate, we identified the optimal conditions that yield the maximum improvement in heat transfer over the steady conditions. Figure 2.5.26 shows that this maximum occurs at an average mass flow rate of approximately 0.65 slpm for large amplitude pressure fluctuations at 20hz, with the MEMS nozzle 500um above the surface.

Temperature Difference at Impingment Point
(500um height,20hz, constant Δ P)
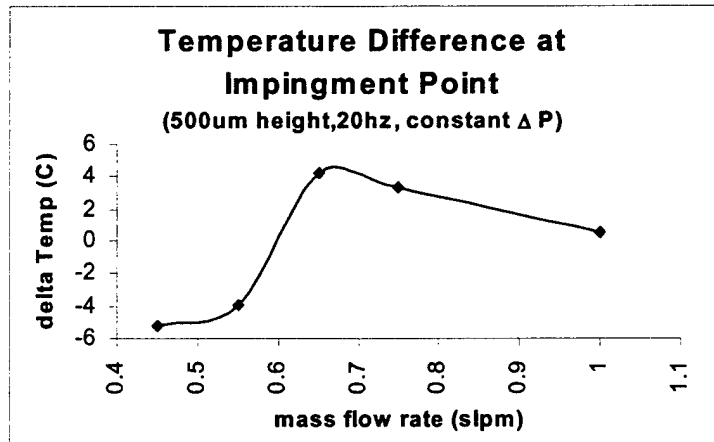
Figure 2.5.26 Identification of the unsteady actuation and flow parameters which yields the maximum temperature difference between the steady and unsteady case.

Based on a matrix of tests, the functional dependence of the enhanced heat transfer on the mean jet speed, perturbation level and perturbing frequency has been established, and the local maximum conditions identified. In summary, so far, a comparison of steady and perturbed flow situations show that the temperature difference between the two situations increases at low perturbation frequencies and at high fluctuation pressure levels. In order to analyze why local maximums were not observed at higher actuation frequencies, the power frequency spectrum of the surface temperature distribution is examined so that insight into the coupling of flow structure and regions of enhanced convective heat transfer can be understood.

Figure 2.5.27 is the power spectrum of the temperature signal from a sensor 500um away from the impingement point. Although the actuation frequency (red line) is 20Hz, Figure 4 shows that there is still a coherent flow structure passing this sensor location at a slightly higher frequency of approximately 25Hz. This coherent flow structure is observed at other temperature sensor locations in the 20Hz, large amplitude actuation case. Figure 5 is the power spectrum at 50 Hz actuation (red line), but there is no longer a coherent temperature signal, and hence fluid structure at any of the expected nearby frequencies. (excluded line noise around 60 Hz).
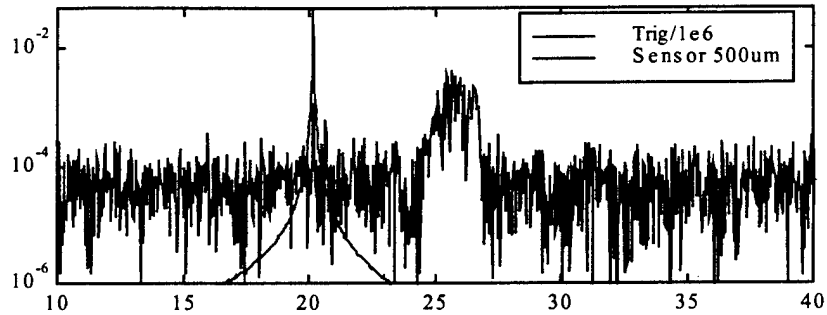
Figure 2.5.27. FFT of sensor signal (blue) and actuation (red) at 20hz actuation frequency, 500um from impingement point.
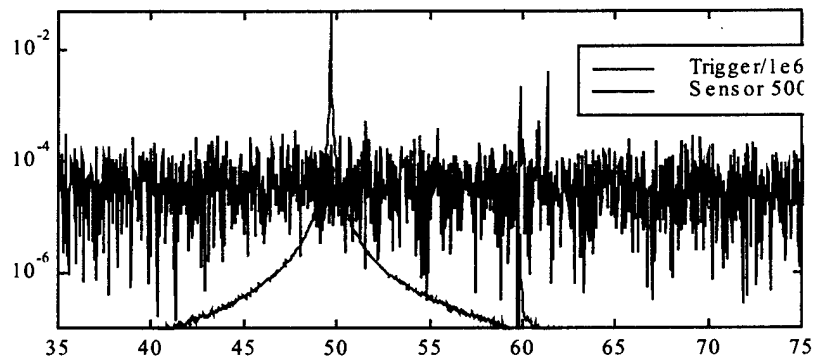
Figure 5. FFT of sensor signal (blue) at 50hz actuation frequency, 500um from impingement point.

Although not conclusive until we are able to visualize this micro flow, it is hypothesized that the enhanced heat transfer in this situation is due to the generation of flow structures associated with the self-sustained low-frequency components in an impinging shear layer, as observed by Knisely and Rockwell [5]. Self-sustained oscillations can arise due to the presence of a downstream travelling wave and its associated vortex formation, its impingement upon a corner, and the upstream influence of this vortex-corner interaction on the original travelling wave. In our situation, it must be remembered that the MEMS impinging jet is not a free jet configuration but rather a semi-confined jet with the silicon wafer extending approximately 2 mm away from the nozzle exit, which forms the "top" wall of the confined jet. Then any vortices formed at the nozzle exit could interact with any vortices formed at the perimeter edge of the wafer "top"wall, and possibly generating a situation where self-sustained oscillations could continuously cycle hotter gas up from the boundary layer and mix with cooler fluid from the nozzle and edge vortices, thus enhancing the local heat transfer in the chip region between these edges.

2.6 Conclusion

The study of MEMS impinging-jet cooling has yielded a MEMS-based heat transfer measurement paradigm, as well as extensive experimental data on jet-impingement heat transfer. The MEMS-based measurement paradigm successfully integrates sensing and heating, and allows measurement in a significantly large area at a very high spatial resolution. The heat transfer data demonstrate the excellent promise of micro-impinging-jet heat transfer, and provide useful rules for designing impinging-jet-based micro heat exchangers.

The MEMS-based heat transfer measurement paradigm includes a technology for MEMS device fabrication, an experimental setup well suited for micro scale thermal study, and an accurate and an efficient data processing technique. In the technology aspect, we have developed silicon nozzles and nozzle arrays for jet generation, as well as silicon and quartz temperature imagers with integrated micro heaters and temperature sensors made of polysilicon thin films. The heaters have excellent heating uniformity, and the temperature sensors are very small in size (4 μm x 4 μm), are distributed over a significantly large area (1 cm x 1 cm) and offer good temperature resolution (0.1°C). Due to integration of the heaters and sensors, the temperature imagers can be easily fabricated, are highly reliable, and causes virtually no disturbances to the flow. The small size of temperature sensors enable the temperature imagers to have unmatched spatial resolution. This is especially true for the quartz-based imager for the low thermal conductivity of quartz allows for significantly large temperature gradients in the chip and hence excellent relative precision. The high spatial resolution and large sensor-distributed area enabled us to perform accurate measurement of microscale local temperature distributions. This was never possible before with conventional temperature sensors, whose large size and demanding assembly needs only allow measurement in an average sense, with limited reliability and possibly significant disturbances to the jet flow.

In terms of the experimental setup, a vacuum chamber thermally insulated the backside of the temperature imagers. This thermal insulation was very important for eliminating the heat loss from the backside to media other than the imager chip, and ensures measurement accuracy. The jet nozzles and imager chip were placed inside a metal enclosure to eliminate disturbances to the jet flow. As for the data processing technique, we determined the axisymmetric temperature distribution on the front side of the temperature imager due to single-jet impingement by performing a spline-based least-squares curve fitting. The front side temperature distribution (for both single- and array-jet impingement) and backside uniform heating were used as input for finite element analysis to compute the heat transfer coefficient.

Our innovative thermal measurement paradigm has allowed us, for the first time, to obtain detailed information on the 2-D temperature distribution over the surface impinged upon by single or array jets. We use such information to identify optimal nozzle configurations for a given set of design constraints (available inlet pressure or maximum allowable surface temperature).

In the single-jet experiments, we observed a significant decrease in global chip surface temperature (averaged over a 2 x 2 cm2 area) using MEMS impinging-jet cooling. This impressive preliminary result inspired us to extensively investigate the micro jet cooling. In our further experiments, we saw the jet cooling effect of our 1st generation MEMS nozzle start to greatly decrease when the gap between the nozzle and the impingement surfaces became smaller than one half of the gaseous path length between the two surfaces. This phenomenon was not observed in the capillary jet experiments. Our calculation showed that the relatively long and small path confines the gas flow in the laminar region and increases flow resistance, leading to a poor heat transfer rate. This is clearly undesirable in practical heat exchanger design, since the higher driving pressure required is a significant burden. Our 2nd generation MEMS nozzle, fabricated by DRIE in stead of KOH silicon anisotropic etching, resembles a capillary nozzle with its relatively thin-walled structure ($100\mu m$ in thickness and $400\mu m$ in length). The thin wall greatly reduces confinement effects. More importantly, the extra space between the bulk of the nozzle chip and impingement surface allows vortex generation around the high-speed jet (Ho 1985) to further enhance heat transfer.

The heat transfer coefficient results computed from our data show the peak value of heat transfer coefficient can as large as 0.3 W/cm^2K (several times larger than conventional jets), as well as an approximate effective cooling range of $r/D \approx 1.5$. This demonstrates the excellent effectiveness of micro impinging jets for local spot cooling, and provides a guideline for designing efficient micro heat exchangers.

From the single-jet experiments with the 2nd generation nozzle, it was observed that the higher the driving pressure, the higher the heat transfer coefficient. This is easy to understand because the mass flow rate increases with the driving pressure, allowing the heat to be transferred away more effectively. The stronger turbulence level due to the corresponding increase of the gas speed also enhances the heat transfer. While the pressure greatly influences the heat transfer, the different jet heights (H/D varied from 1 to 6) investigated in our experiments did not have a significant effect on the heat transfer rate. This shows that the flow confinement with the 1st generation MEMS nozzle was successfully eliminated, and that a relatively large tolerance in the jet height is allowed in practical heat exchanger design.

Our experiments with micro impinging-jet arrays have yielded useful results on the influence of the jet-to-jet spacing, the flow rate, as well as the jet height on the heat transfer rate. The jet-to-jet spacing appears to have an insignificant effect on the heat transfer, while higher flow rates result in higher heat transfer rates. It has been shown that the jet height influences the heat transfer quite significantly. As the jet height decreases up to an optimal value, the average heat-transfer coefficient increases. This phenomenon is in contrast to the single-jet case, where the jet height has a much more insignificant effect. We believe that the interference between adjacent jets may have contributed favorably to enhance the heat transfer. To demonstrate applications of impinging-jet arrays to micro heat exchangers, we experimented with a 10 x 10 jet array. The resulting data show that a considerably uniform heat transfer coefficient, on the order of 0.1 W/cm^2K, can be achieved. This rate, approximately 5 times that achievable by a

comparable macro single jet, shows that micro impinging-jet-array based heat exchangers are quite promising.

Finally, the investigation of cooling effects using an unsteady impinging jet has been performed. Our investigation has demonstrated that unsteady impinging jets can further improve heat transfer, which will be well suited for micro heat exchanger design.

3. MICRO CHANNEL FLOW

3.1 Introduction

Micromachining is a rapidly emerging technology in which micron-scaled fluidic devices are possible for the first time. For example microchannels may be used in a variety of applications such as for cooling of electronic circuits, transport of gases in micro chromatography, and microfluidic control. In order to design and fabricate such micro devices effectively, the physical laws governing fluid flow in small conduits need to be understood. Such flow differs from its macroscopic counterpart in that non-continuum effects for a gas or polar mechanics effects for a liquid may not be negligible due to the small scale of the flow.

The field of micromachining is still new, and thus it is that only in recent years, microchannel flow has attracted considerable attention. Pfahler, et al. [6] estimated experimentally the friction factor for gas and liquid flow in small channels. Nevertheless, Arkilic et al. [7] considered the effect of compressibility in a microchannel flow. The most detailed studies up-to-date were conducted by Pong et al. [8] and Shih et al. [9] who measured not only the overall pressure drop and flow rate, but also the pressure distribution along the microchannel. However, they were only able to obtain data for relatively low inlet pressures because of the low operating pressure in these first generation devices [10]. They showed that by considering slip and compressible effects, the flow rate could be accurately determined.

There are only a few theoretical studies addressing compressible, viscous, steady laminar flow in small uniform conduits. Prud'homme et al. [11] calculated the mass flow rate of gas through a long tube for an ideal gas. Van den Berg [12] presented a detailed study using perturbation methods to calculate the mass flow rate of a gas through a cylindrical capillary. They clearly identified the effects of compressibility, acceleration and non-parabolicity of the velocity profile. Harley et al. [13] attempted to analyze the same flow in a microchannel, but as they stated, their model is mathematically inconsistent. Here we present an experimental study of gas and liquid flow through a microchannel under high inlet pressures. We compare the results with an analytical model developed for capillary flow that accounts for 2-D, slip and compressibility and corrects for flow acceleration and non-parabolicity. We show that under very high pressures, the resulting change in channel geometry needs to be considered.

Data for liquid flow through a microchannel is scare since not only a much higher pressure is required to obtain measurable values but also the channels are easily blocked by particles. This project then shows that the robust design of the present microchannels, together with the careful set-up of the external flow handling system, allows us to carry out accurate measurement of a liquid flow rate under high inlet pressure.

In addition, several investigations have been done to study heat transfer in microchannels [8], but no experimental data on the temperature distribution along a microchannel is available. This information is required to understand the heat transfer

process and to develop a complete set of analytical models. This is the motivation behind the development of a suspended microchannel with integrated temperature sensors.

3.2 Fundamental of Micro Channel Flow

Micro channel flow is fully investigated on the bases of fluid mechanics. Starting from continuity equation, momentum equation and energy equation, General equations have been derived after several appropriate simplifications.

3.2.1 Parameters in Micro-channel Flow Model

In the analysis of micro-channel flow, two size parameters arise. One is the height-to-length ratio, δ, and the other is the width-to-length ratio, Δ. Since the geometry of the micro channel is 1.2μm high, 40μm wide, and 4000μm long, the two size-parameters in this case become:

$$\delta \equiv \frac{H_d}{L} = 3 \times 10^{-4}, \quad and \quad \Delta \equiv \frac{W_d}{L} = 1 \times 10^{-2}$$

Therefore, it is adequate to assume that,

$$\delta \ll \Delta \lesssim O_r(1) \tag{3.2.1}$$

It is known that, the parameter Δ controls the three-dimensional effect. Under our assumption in equation (3.2.1), we didn't limit $\Delta \ll 1$ (i.e. Δ could be close to 1). That is, we still allow the 3-D effect in our following analysis. Note that, for the channel we used, the flow can be reduced to two-dimensional since W_d is two orders of magnitude smaller than L.

In addition to the size parameter, two other controlling parameters must also be addressed, and they are defined as:

$$K \equiv (-\frac{\Delta P}{P_0}) \equiv \frac{\overline{\mu}_0}{\overline{\rho}_0 U_* L} \frac{1}{\delta^2} \frac{\overline{\rho}_0 U_*^2}{P_0}, \qquad \widetilde{M}_*^2 \equiv \frac{U_*^2}{R\overline{T}_0} = \frac{\overline{\rho}_0 U_*^2}{P_0},$$

where $\overline{\rho}_0, P_0, \overline{T}_0$ are the density, thermodynamic pressure, and temperature at the inlet of the channel. $\overline{\mu}_0$ is the dynamic viscosity of the fluid at $\overline{T}_0$. R is the universal gas constant. ΔP is defined as $P_{out} - P_{in}$, i.e., the pressure difference between the inlet and outlet of the channel. $\widetilde{M}_*$ is the reduced Mach number, and U_* is the typical reference velocity defined as

$$U_* \equiv (-\frac{\Delta P}{L})\frac{(\delta L)^2}{\tilde{\mu}_0}$$

In terms of K and $\tilde{M}_*$, the Reynolds number, based on U_* and channel length L, becomes:

$$Re_* = \frac{1}{K}\frac{\tilde{M}_*^2}{\delta^2},$$

and the Knudsen number, based on the outlet atmospheric condition, is:

$$Kn_{atm} = \left[\frac{\sqrt{2\pi}}{2}\right]\frac{K}{1-K}\frac{\delta}{\tilde{M}_*}.$$

3.2.2 Normalized Governing Equations

In order to have a clear view of the analysis, we normalized the variables in the governing equations. The nondimensional variables are shown as followed (refer to Figure 1),

$$x = \frac{X}{L}, \qquad y = \frac{Y}{\delta L}, \qquad z = \frac{Z}{\Delta L}, \qquad t = \frac{\bar{t}}{L/U_*}$$

$$u = \frac{U}{U_*}, \qquad v = \frac{V}{\delta U_*}, \qquad w = \frac{W}{\Delta U_*}$$

$$p = \frac{P}{P_0}, \qquad \rho = \frac{\bar{\rho}}{\rho_0}, \qquad H = \frac{\bar{H}}{C_p\bar{T}_0}, \qquad T = \frac{\bar{T}}{T_0}, \qquad \mu = \frac{\bar{\mu}}{\mu_0},$$

where t is the nondimensional time normalized by the flow transit time L/U_*. $\bar{H}$ is the total enthalpy defined as $\bar{H} = C_p\bar{T} + (U^2 + V^2)/2$, and C_p is the specific heat at constant pressure.

With the nondimensional variables above, the general governing equations, including continuity, momentum, and energy equations, become

continuity equation:

$$\frac{\partial\rho}{\partial t} + \frac{\partial}{\partial x}[\rho u] + \frac{\partial}{\partial y}[\rho v] + \frac{\partial}{\partial z}[\rho w] = 0 \qquad (3.2.2)$$
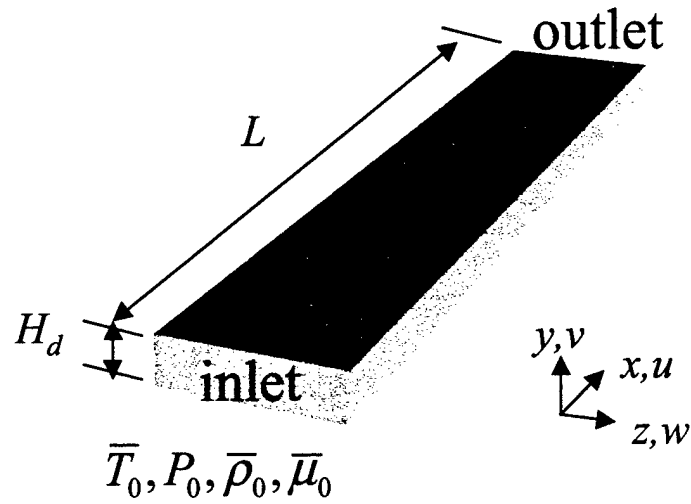
Figure 3.2.1 The variables in micro channel analysis.

momentum equations in x, y, and z direction, (Navier-Stokes equations):

$$\frac{\partial}{\partial t}[\rho u] + \frac{\partial}{\partial x}\left\{\rho u^2 + \frac{p}{\widetilde{M}_*^2} - \frac{2\mu}{3}\left[K\frac{\delta^2}{\widetilde{M}_*^2}\right]\cdot\left[2\frac{\partial u}{\partial x} - \frac{\partial v}{\partial y} - \frac{\partial w}{\partial z}\right]\right\}$$

$$+ \frac{\partial}{\partial y}\left\{\rho uv - \mu\left[K\frac{1}{\widetilde{M}_*^2}\right]\cdot\left[\frac{\partial u}{\partial y} + \delta^2\frac{\partial v}{\partial x}\right]\right\} \tag{3.2.3a}$$

$$+ \frac{\partial}{\partial z}\left\{\rho uw - \mu\left[K\frac{\delta^2}{\Delta^2\widetilde{M}_*^2}\right]\left[\frac{\partial u}{\partial z} + \Delta^2\frac{\partial w}{\partial x}\right]\right\} = 0,$$

$$\frac{\partial}{\partial t}[\rho v] + \frac{\partial}{\partial x}\left\{\rho uv - \mu\left[K\frac{1}{\widetilde{M}_*^2}\right]\cdot\left[\frac{\partial u}{\partial y} + \delta^2\frac{\partial v}{\partial x}\right]\right\}$$

$$+ \frac{\partial}{\partial y}\left\{\rho v^2 + \frac{p}{\delta^2\widetilde{M}_*^2} - \frac{2\mu}{3}\left[K\frac{1}{\widetilde{M}_*^2}\right]\cdot\left[2\frac{\partial v}{\partial y} - \frac{\partial u}{\partial x} - \frac{\partial w}{\partial z}\right]\right\} \tag{3.2.3b}$$

$$+ \frac{\partial}{\partial z}\left\{\rho vw - \mu\left[K\frac{\delta}{\Delta\widetilde{M}_*^2}\right]\left[\frac{\delta}{\Delta}\frac{\partial v}{\partial z} + \frac{\Delta}{\delta}\frac{\partial w}{\partial x}\right]\right\} = 0,$$

53

$$\frac{\partial}{\partial t}[\rho w] + \frac{\partial}{\partial x}\left\{\rho uw - \mu\left[K\frac{\delta^2}{\Delta^2 \tilde{M}_*^2}\right]\left[\frac{\partial u}{\partial z} + \Delta^2\frac{\partial w}{\partial x}\right]\right\}$$

$$+ \frac{\partial}{\partial y}\left\{\rho vw - \mu\left[K\frac{\delta}{\tilde{M}_*^2}\right]\cdot\left[\frac{\delta}{\Delta}\frac{\partial v}{\partial z} + \frac{\Delta}{\delta}\frac{\partial w}{\partial y}\right]\right\} \qquad (3.2.3c)$$

$$+ \frac{\partial}{\partial z}\left\{\rho w^2 + \frac{p}{\Delta^2 \tilde{M}_*^2} - \frac{2\mu}{3}\left[K\frac{\delta^2}{\Delta^2 \tilde{M}_*^2}\right]\cdot\left[2\frac{\partial w}{\partial z} - \frac{\partial u}{\partial x} - \frac{\partial v}{\partial y}\right]\right\} = 0,$$

energy equation:

$$\frac{\partial}{\partial t}\left[\rho H - \frac{R}{C_p}p\right] + \frac{\partial}{\partial x}\left\{
\begin{array}{l}
\rho uH - \frac{2\mu u}{3}\left[K\delta^2\frac{R}{C_p}\right]\left[2\frac{\partial u}{\partial x} - \frac{\partial v}{\partial y} - \frac{\partial w}{\partial z}\right] - \mu v\left[K\delta^2\frac{R}{C_p}\right]\left[\frac{\partial u}{\partial y} + \delta^2\frac{\partial v}{\partial x}\right] \\
- \mu w\left[K\delta^2\frac{R}{C_p}\right]\left[\frac{\partial w}{\partial x} + \frac{\partial u}{\partial z}\right] - \frac{\mu}{P_r}\left[K\frac{\delta^2}{\tilde{M}_*^2}\right]\frac{\partial}{\partial x}\left[H - \frac{u^2 + \delta^2 v^2 + \Delta^2 w^2}{2}\right]
\end{array}
\right\}$$

$$+ \frac{\partial}{\partial y}\left\{
\begin{array}{l}
\rho vH - \mu u\left[K\frac{R}{C_p}\right]\left[\frac{\partial u}{\partial y} + \delta^2\frac{\partial v}{\partial x}\right] - \frac{2\mu v}{3}\left[K\delta^2\frac{R}{C_p}\right]\left[2\frac{\partial v}{\partial y} - \frac{\partial u}{\partial x} - \frac{\partial w}{\partial z}\right] \\
- \mu w\left[K\delta\Delta\frac{R}{C_p}\right]\left[\frac{\delta}{\Delta}\frac{\partial v}{\partial z} + \frac{\Delta}{\delta}\frac{\partial w}{\partial y}\right] - \frac{\mu}{P_r}\left[K\frac{1}{\tilde{M}_*^2}\right]\frac{\partial}{\partial y}\left[H - \frac{u^2 + \delta^2 v^2 + \Delta^2 w^2}{2}\right]
\end{array}
\right\}$$

$$+ \frac{\partial}{\partial z}\left\{
\begin{array}{l}
\rho wH - \mu u\left[K\frac{\delta^2}{\Delta^2}\frac{R}{C_p}\right]\left[\frac{\partial u}{\partial z} + \Delta^2\frac{\partial w}{\partial x}\right] - \mu v\left[K\frac{\delta^3}{\Delta}\frac{R}{C_p}\right]\left[\frac{\delta}{\Delta}\frac{\partial v}{\partial z} + \frac{\Delta}{\delta}\frac{\partial w}{\partial y}\right] \\
- \frac{2\mu w}{3}\left[K\delta^2\frac{R}{C_p}\right]\left[2\frac{\partial w}{\partial z} - \frac{\partial u}{\partial x} - \frac{\partial v}{\partial y}\right] - \frac{\mu}{P_r}\left[K\frac{\delta^2}{\Delta^2 \tilde{M}_*^2}\right]\frac{\partial}{\partial z}\left[H - \frac{u^2 + \delta^2 v^2 + \Delta^2 w^2}{2}\right]
\end{array}
\right\} = 0.$$

$$(3.2.4)$$

Before we go any further, it is worthwhile to point out that we can also use δ and $\tilde{M}_*$ to classify flow regimes instead of Knudsen number. In our case, the order of magnitude between $\tilde{M}_*$ and δ is

$$\delta \ll \tilde{M}_* \ll O_r(1) \qquad (3.2.5)$$

and the flow is classified as in the lower end of translational nonequilibrium regime, i.e. the slip effect is not strong. In this regime, the classical small slip-wall boundary conditions, which will be discussed later, are adequate. However, while $\delta/\tilde{M}_* = O_r(1)$, the flow is in the translational nonequilibrium regime, and the NS equations with small slip-wall boundary conditions are not applicable. As we mentioned before, A higher-order term is needed to correct the nonequilibrium effect in this case. In fact, all the arguments above are similar to the classification by Knudsen number since the Knudsen number is proportional to the ratio, $\delta / \tilde{M}_*$.

Along with the assumptions of equation (3.2.1) and (3.2.5), we also assume $K \equiv \left(-\Delta P / P_0\right)$ is in the order of one, i.e.,

$$K \equiv \left(-\Delta P / P_0\right) = O_r(1) \tag{3.2.6}$$

In the next several sections, equation (2.5) and (2.6) will be used to simplify the governing equations. Afterward, we are able to obtain the isothermal condition and general solutions.

3.2.3 Isothermal Condition

In the study of Arkilic *et al*, Beskok *et al*, and Shih *et* [7,10], an assumption of isothermal condition was made. In this section, the isothermal condition will be derived from the energy equation, and it shows the assumption is not necessary. With the isothermal condition, the N-S equations and continuity equation can be further simplified.

With the three assumptions, equation (3.2.1), (3.2.5), and (3.2.6), to the leading order, the energy equation can be reduced to

$$\frac{\partial}{\partial y} \mu \frac{\partial T}{\partial y} = 0 + O_r\left[\tilde{M}_*, \delta^2, \frac{\delta^2}{\Delta^2}\right] \approx 0$$

After integrating once with respect to y, this becomes

$$\mu \frac{\partial T}{\partial y} = c \tag{3.2.7}$$

where c is an integration constant and a function of *x,z,t*. Since the experiment is conducted under room temperature, with no heating/cooling generated to the channel walls, the walls should maintain at the same temperature as that of the surrounding environment. Hence, the temperature T is symmetric with respect to the symmetry plane, *y=0.5*, that is, $\partial T / \partial y = 0$ at *y=0.5*. By applying this condition to Equation (2.7), we found the integration constant, c, equals to zero, and the nondimensional variable T becomes constant, i.e.,

$$T = 1.$$

Thus, to the leading order, the flow field in the micro channel is in the *isothermal* state, and the isothermal assumption made in the previous study is justified. In fact, the reduction to isothermal condition is not too surprising, because the reduced Mach number is quite small ($\tilde{M}_* \ll 1$). The flow does not have enough convection energy to provide the heat transfer along the channel. However, if the experiment is conducted under the condition such that $\tilde{M}_* = O_r(1)$, then not only the convection terms in energy equation are

important, but also the temperature jump at the wall will play an important role in determining the flow-field behavior in the micro channel.

It is worthwhile to point out that the *isothermal* condition remains valid, to the leading order, in the transnational non-equilibrium regime since the only difference is in $\delta \approx \tilde{M}_* << O_r(1)$. Even for the unsteady case, as long as the time scale is comparable to the flow-transit time L/U_*, the isothermal condition is still valid.

3.2.4 Classical Small Slip Boundary Condition and General Solutions

After substituting the continuity equation into Navier-Stokes equations and taking out the higher order terms, the Navier-Stokes equations become,

$$\frac{\partial p}{\partial x} - \mu \frac{\partial^2 u}{\partial y^2} \cdot K = 0 + O_r \left[\delta^2, \frac{\delta^2}{\Delta^2} \right] \qquad (3.2.8a)$$

$$\frac{\partial p}{\partial y} = 0 + O_r \left[\delta^2, \frac{\delta^4}{\Delta^2} \right] \qquad (3.2.8b)$$

$$\frac{\partial p}{\partial z} - \Delta^2 \frac{\partial^2 w}{\partial y^2} \cdot K = 0 + O_r \left[\delta^2, \delta^2 \Delta^2 \right] \qquad (3.2.8c)$$

Also, with the isothermal condition, the normalized dynamics viscosity μ becomes

$$\mu = 1 + O_r \left[M_*^2, \delta^2, \frac{\delta^2}{\Delta^2} \right] \quad ,$$

and the equation of state $(p = \rho T)$ reduces to

$$p = \rho + O_r \left[M_*^2, \delta^2, \frac{\delta^2}{\Delta^2} \right] \quad .$$

Employing these two conditions above and assumption (3.2.1), (3.2.5) and (3.2.6), the leading-order governing equation (2.2) and (2.8a-c) become

Continuity equation:

$$\frac{\partial p}{\partial t} + \frac{\partial}{\partial x}[pu] + \frac{\partial}{\partial y}[pv] + \frac{\partial}{\partial z}[pw] = 0 \qquad (3.2.9)$$

Momentum equations:

$$\frac{\partial p}{\partial x} = K\frac{\partial^2 u}{\partial y^2} + O_r\left[\delta^2, \frac{\delta^2}{\Delta^2}\right] \qquad (3.2.10a)$$

$$\frac{\partial p}{\partial y} = 0 + O_r\left[\delta^2, \frac{\delta^4}{\Delta^2}\right] \qquad (3.2.10b)$$

$$\frac{\partial p}{\partial z} = K\Delta^2\frac{\partial^2 w}{\partial y^2} + O_r\left[\delta^2, \delta^2\Delta^2\right] \qquad (3.2.10c)$$

Here, two boundary conditions are considered; one is nonslip boundary condition, and the other is classical small wall-slip boundary condition. For nonslip condition, the fluid on the wall is at rest $(u = v = w = 0)$, and the temperature is on the prescribed value $(T = T_w)$. For small wall-slip condition, it allows velocity slip and temperature jump on the wall, namely,

$$u = C\frac{\mu}{\rho\sqrt{T}}\frac{\partial u}{\partial N} \qquad (3.2.11a)$$

$$w = C\frac{\mu}{\rho\sqrt{T}}\frac{\partial w}{\partial N} \qquad (3.2.11b)$$

$$T = T_w + C\frac{2\gamma}{P_r(\gamma+1)}\frac{\mu}{\rho\sqrt{T}}\frac{\partial T}{\partial N} \qquad (3.2.11c)$$

where N is the normal outward direction of the wall, and C is defined as

$$C \equiv \left[\frac{2-\alpha}{\alpha}\frac{\sqrt{2\pi}}{2}\right]\left[K\frac{\delta}{\tilde{M}_*}\right]$$

α, γ, and P_r are accommodation coefficient, specific heat ratio, and Prandtl number, respectively. The slip boundary condition is derived from Maxwell's theory. Note that, this boundary condition is adequate if the slip effect is not too large. As you can see in equation (2.11), it is determined by the coefficient C, controlled by parameter $(K\delta/\tilde{M}_*)$. In the previous section, we have known $\delta << \tilde{M}_*$, $K \approx O_r(1)$, and $\tilde{M}_*$ and δ can determine the flow regime. It is not hard to understand that the values of slip coefficient are controlled by them. Also note that, the boundary condition can be related to the Knudsen number, since

$$Kn \equiv \frac{\overline{\lambda}}{H_d} = \left[\frac{\sqrt{2\pi}}{2}\right]\left[K\frac{\delta}{\widetilde{M}_*}\right] \quad \propto \quad C.$$

With respect to y, we can integrate equation (3.2.10a) and (3.2.10c) twice to obtain the general solution of the streamwise and spanwise velocity. After applying the slip boundary conditions, equation (3.2.11a,b), at y=0,1, it yields

$$u = \frac{1}{2K}\frac{dp}{dx}(y^2 - y - \frac{C}{p}), \qquad (3.2.12a)$$

$$w = \frac{1}{2K\Delta^2}\frac{dp}{dz}(y^2 - y - \frac{C}{p}), \qquad (3.2.12b)$$

The equations above are not in the similarity form because p is a function of x,z,t, thus, C/p can not be scaled out. As the slip effect is weaker, the correction term, C, becomes smaller. To the extreme case, C equals to zero, and the solution of u can be reduced to the classical Poiseuille flow, and the similarity solutions exist.

Applying the solutions of *u* and *w* (equation (2.12a,b)) into continuity equation (equation (2.9)), we can obtain

$$\frac{\partial v}{\partial y} = -\frac{1}{2K}\left\{\begin{array}{l}\left[\left(y^2 - y - \frac{C}{p}\right)\frac{\partial^2 p}{\partial x^2} + \left(\frac{\partial p}{\partial x}\right)^2\frac{y^2 - y}{p}\right] + \\ \frac{1}{\Delta^2}\left[\left(y^2 - y - \frac{C}{p}\right)\frac{\partial^2 p}{\partial z^2} + \left(\frac{\partial p}{\partial z}\right)^2\frac{y^2 - y}{p}\right]\end{array}\right\} - \frac{1}{p}\frac{\partial p}{\partial t}$$

and it can be simplified as

$$\frac{\partial v}{\partial y} = -\frac{1}{2Kp}\left[\frac{1}{2}\left(\frac{\partial^2 p^2}{\partial x^2} + \frac{1}{\Delta^2}\frac{\partial^2 p^2}{\partial z^2}\right)(y^2 - y) - C\left(\frac{\partial^2 p}{\partial x^2} + \frac{1}{\Delta^2}\frac{\partial^2 p}{\partial z^2}\right) + 2K\frac{\partial p}{\partial t}\right]$$

after an integration with respect to y,

$$v = -\frac{1}{K}\frac{1}{p}\left\{\frac{1}{4}\left(\frac{y^3}{3} - \frac{y^2}{2}\right)\left(\frac{d^2 p^2}{dx^2} + \frac{1}{\Delta^2}\frac{d^2 p^2}{dz^2}\right) - y\left[\frac{C}{2}\left(\frac{d^2 p}{dx^2} + \frac{1}{\Delta^2}\frac{d^2 p}{dz^2}\right) - K\frac{\partial p}{\partial t}\right]\right\} + D,$$

where D is an integration constant. Here, v is assumed to be anti-symmetric with respect to the symmetry plane (y=0.5), i.e., v=0 at y=0.5. Substitute this condition into the equation above, and it becomes

$$v = -\frac{1}{K}\frac{1}{p}\left\{\frac{1}{4}\left(\frac{y^3}{3}-\frac{y^2}{2}+\frac{1}{12}\right)\left(\frac{d^2p^2}{dx^2}+\frac{1}{\Delta^2}\frac{d^2p^2}{dz^2}\right)-\left(y-\frac{1}{2}\right)\left[\frac{C}{2}\left(\frac{d^2p}{dx^2}+\frac{1}{\Delta^2}\frac{d^2p}{dz^2}\right)-K\frac{\partial p}{\partial t}\right]\right\},$$

also, v has to be zero at the wall, i.e., $v=0$ at $y=0$. By applying this boundary condition, we finally can get the general expression of pressure p as

$$\frac{\partial p}{\partial t}-\frac{1}{24K}\left[\frac{\partial^2}{\partial x^2}+\frac{1}{\Delta^2}\frac{\partial^2}{\partial z^2}\right]\left[p^2+12C\cdot p\right]=0 \qquad (3.2.13)$$

If we substitute equation (2.17) back to the transverse velocity equation above, and we will have a more compact expression of v without the time derivative term. (eq. (3.2.14))

$$v = -\frac{1}{24Kp}\left[2y^3-3y^2-y\right]\left[\frac{\partial^2 p^2}{\partial x^2}+\frac{1}{\Delta^2}\frac{\partial^2 p^2}{\partial z^2}\right] \qquad (3.2.14)$$

As we can see in equation (3.2.12) and (3.2.14), the solution of u, v, and w are gauged by the parameter K, which is the only controlling parameter in the case of nonslip. In the case of slip, another parameter, C, is included as a correction term. It is obvious that, instead of Reynolds number, K is a more explicit parameter related to the flow behavior in the micro-channel study.

In the experiments, the flow is assumed fully developed and steady. Therefore, equation (2.13) can be rewritten as

$$\left[\frac{\partial^2}{\partial x^2}+\frac{1}{\Delta^2}\frac{\partial^2}{\partial z^2}\right]\left[p^2+12C\cdot p\right]=0 \qquad (3.2.15a)$$

or

$$\left[\frac{\partial^2}{\partial x^2}+\frac{1}{\Delta^2}\frac{\partial^2}{\partial z^2}\right]\hat{P}=0 \qquad (3.2.15b)$$

where $\hat{P}=p^2+12C\cdot p$.

Besides, due to the geometry of the micro channel, we can reduce the flow into 2-D flow in our study, and the equation (3.2.15b) is reduced to

$$\frac{\partial^2 \hat{P}}{\partial x^2}=0 \qquad (3.2.16)$$

Furthermore, in order to make the analysis easier, we rewrite equation (3.2.16) in the similarity form,

$$\frac{\partial^2 \widetilde{P}}{\partial x^2} = 0 \qquad (3.,2.17)$$

where $\widetilde{P} \equiv \dfrac{\hat{P} - \hat{P}_{out}}{\hat{P}_{in} - \hat{P}_{out}}$.

And the solution to equation (2.17) becomes

$$\widetilde{P} = 1 - x \qquad (3.2.18)$$

As noted, for nonslip-wall case, the streamwise velocity u reduces to that of classical Poiseuille flow, and similarly, it results in a vanishing transverse velocity. However, as contrary to $d^2 p / dx^2 = 0$ for incompressible flow, the pressure equation will reduce to $d^2 p^2 / dx^2 = 0$ or $d^2 \widetilde{P} / dx^2 = 0$, owing to the fluid compressibility.

3.2.5 General Solution for Flow Rate

In the previous section, we have already derived the streamwise velocity in equation (3.2.12). Here, we can obtain the expression of mass flow rate by $\dot{m} = \rho A U$, where ρ is density, A is cross section area, and U is the streamwise velocity. The mass flow rate becomes,

$$\dot{m} = \left(\frac{P}{R\overline{T}_0} \right) \left(H_d \cdot W_d \right) \int_0^1 U.udy \qquad (3.2.19)$$

substitute equation (3.2.12a) into (3.2.19),

$$\dot{m} = \frac{1}{24} \frac{1}{R\overline{T}_0 \overline{\mu}_0} \frac{W_d H_d^3}{L} \cdot P_0^2 \left[-12p \frac{\partial p}{\partial x} \left(\frac{1}{6} + \frac{C}{p} \right) \right] \qquad (3.2.20)$$

According to equation (3.2.16), $\hat{P}$ is a linear function of x, i.e. $p^2 + 12Cp = -ax + b$. The values of a and b are experimentally determined. Since the pressure distribution is available in the experiment, the a and b can be obtained by least-square curve fitting. After taking the derivative w.r.t. x on both side, it becomes

$$12p \frac{\partial p}{\partial x} \left(\frac{1}{6} + \frac{C}{p} \right) = -a$$

Therefore, from equation (3.2.20), the final expression of mass flow rate is,

$$\dot{m} = \frac{1}{24} \frac{1}{R\overline{T}_0 \overline{\mu}_0} \frac{W_d H_d^3}{L} \cdot P_0^2 \cdot a \qquad (3.2.21)$$

3.3 MEMS Device Design and Fabrication

3.3.2   1st Generation Suspended Micro Channel with Integrated Temperature Sensors

The freestanding microchannels with integrated thermal sensors were fabricated using surface micromachining techniques, while the thermal isolation cavity as well as the inlet and outlet bores were bulk micromachined.

The fabrication process, schematically shown in Figure 3.3.1, started with low pressure chemical vapor deposition (LPCVD) of a 1 μm thick nitride layer on a bare <100> oriented silicon wafer, followed by the patterning of the channel inlet and outlet. Next, a 2 μm LPCVD PSG sacrificial layer, which defines the microchannel length, width, and height, was deposited on the topside of the wafer. Another 0.5 μm thick layer of LPCVD nitride was deposited on the PSG to define the channel boundaries, i.e. sidewalls and ceiling. A 0.5 μm layer of LPCVD polysilicon was then deposited and patterned to form the temperature sensors on top of the microchannel. Selective boron ion implantation was used to control the electrical properties of the polysilicon. The sensor element, 4 μm x 4 μm in size, was lightly doped with boron ($5 \cdot 10^{18}$/cm^3) giving the sensor a nominal room temperature resistance of 30 kΩ. The polysilicon contact lines to the sensor that were heavily boron doped ($5 \cdot 10^{20}$/cm^3) to lower the resistance of the sensor leads. A RIE was performed to open holes through the nitride to the PSG in order to facilitate etching. The sacrificial etching of the microchannels in a 49% HF solution to remove the PSG layer immediately followed.

The newly formed microchannels were re-sealed by uniformly depositing a 0.5 μm layer of LPCVD nitride. This completed the fabrication of the microchannels with the channels having 1 μm thick walls. An anisotropic TMAH solution was used to bulk etch the channel inlet and outlet bores, and a second RIE step was then used to open contacts through the nitride to the polysilicon underneath. Metalization formed bonding pads for connections between the macro-world and the sensor elements and, finally, thermal isolation of the channel was achieved by isotropically bulk micromachining the silicon underneath the channel. A photoresist mask was used to protect the channel and its suspension stringers from a BrF$_3$ dry etch [9], which resulted in a cavity 80 μm deep and about 500 μm wide. The channel used in all the experiments documented in this report, see photograph in Figure 3.3.2, was 4.4 mm long, 1.85 μm high, and 19 μm wide. These dimensions were obtained using an Alpha Step Profiler. The microchannels are suspended by 200 μm long stringers on each side spaced approximately 500 μm apart. The temperature sensor contact lines run from the center of the channel out along the stringers, as shown in Figure 3.3.3 and 3.3.4, and to the bonding pads next to the isolation cavity
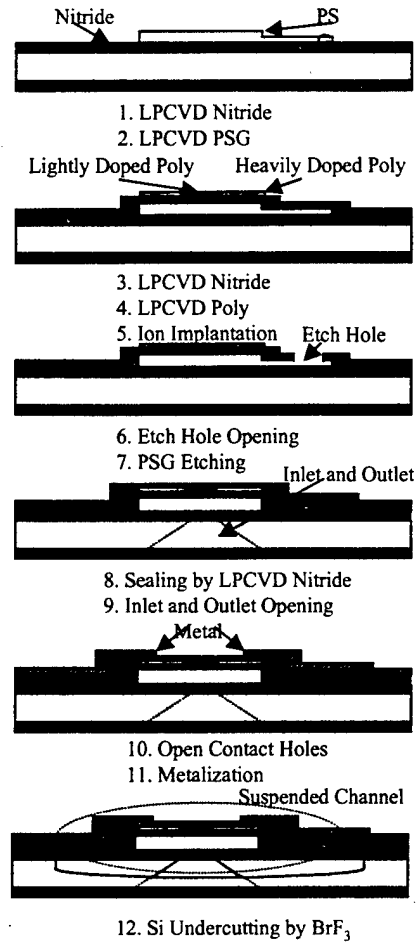
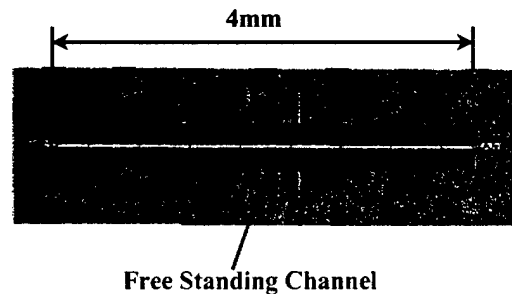Figure 3.3.1. Fabrication Process for 1st generation suspended micro channel.

Figure 3.3.2. Top view of suspended micro channel with integrated temperature sensors

Figure 3.3.3 and 3.3.4. Cross sectional electron micrographs of suspended channel and integrated sensor.

3.3.3 2nd Generation Suspended Micro Channel with Integrated Temperature Sensors

The fabrication process is similar to the first generation design except the polysilicon layer is sandwiched between two low temperature oxide depositions. The oxide is later sacrificially etched to produce the freestanding sensor inside of the nitride channel as shown in Figure 3.3.5.
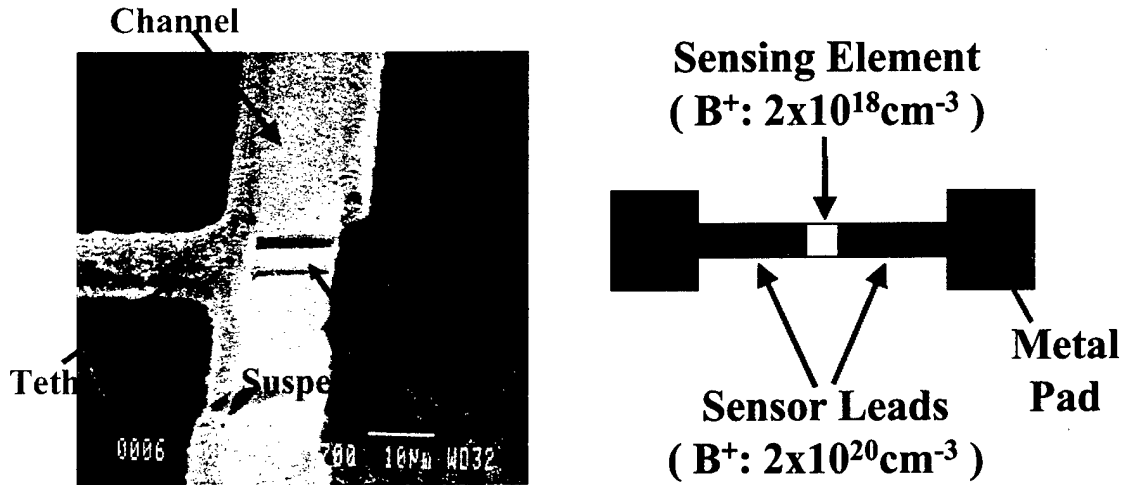

Figure 3.3.5. Second generation micro channel with suspended temperature sensor inside.

3.3.4 MEMS Fluidic Coupler

Since these channels routinely undergo high pressure testing, it is of paramount importance to design a fitting that can withstand these rigors. The fitting pictured in figures 3.3.6 and 3.3.7 is 1 mm x 1mm square and can accommodate tubing with diameters up to 0.7mm.
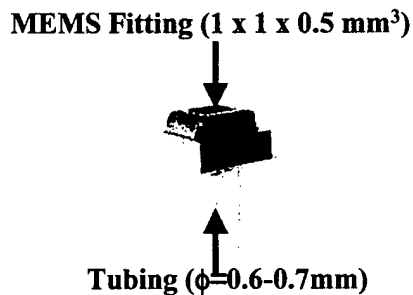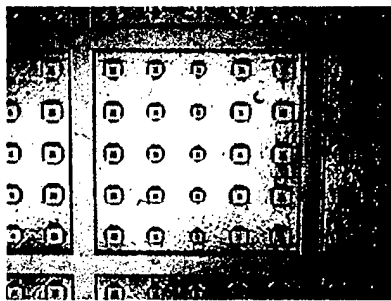
Figures 3.3.6 and 3.3.7. Fitting before dicing (left) and fitting connected to glass tubing. (right).

The fitting acts to position the tubing correctly over the channel inlet, and when used with epoxy, provides a gas tight seal. The fabrication process flow is outlined in Figure 3.3.8. An isotropic etch defines the gas inlet. The tubing rests inside a DRIE bulk etched pit.

1. Mask Material growth
2. Patterning for wet etch

3. Si anisotropic etch
4. Patterning for DRIE

5. Pit Etching by DRIE
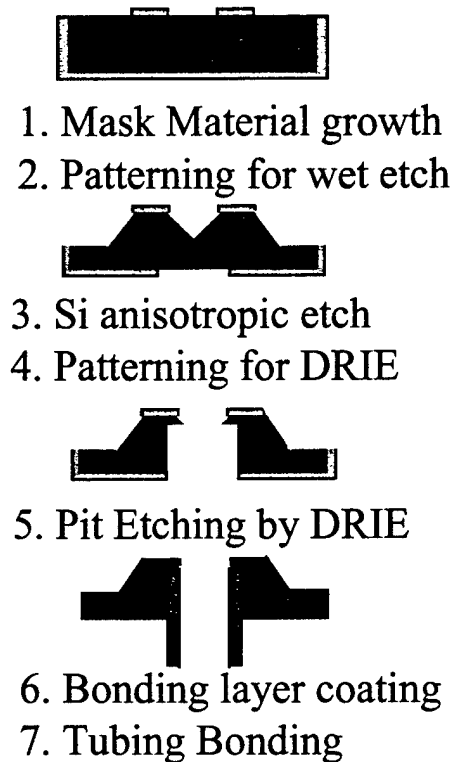
6. Bonding layer coating
7. Tubing Bonding

Figure 3.3.8. Fabrication process flow for MEMS fitting.

3.3.5 Micro Channel with Integrated Nano-Flow Sensor

We have fabricated three types of nano-flow sensors, which consist of polysilicon heaters and temperature sensors fabricated with silicon-nitride channels. Figure 3.3.9 shows the top view of a fabricated device and the cross sections of three designs. The microchannels have a dimension of 2mm x 20µm x 2µm. The polysilicon sensor is built on the nitride channel wall [1]. In one design, the channel is built directly on the substrate, while in another, the channel is suspended from the substrate using BrF_3 undercutting of Si [2], as shown in figure 3.3.10.
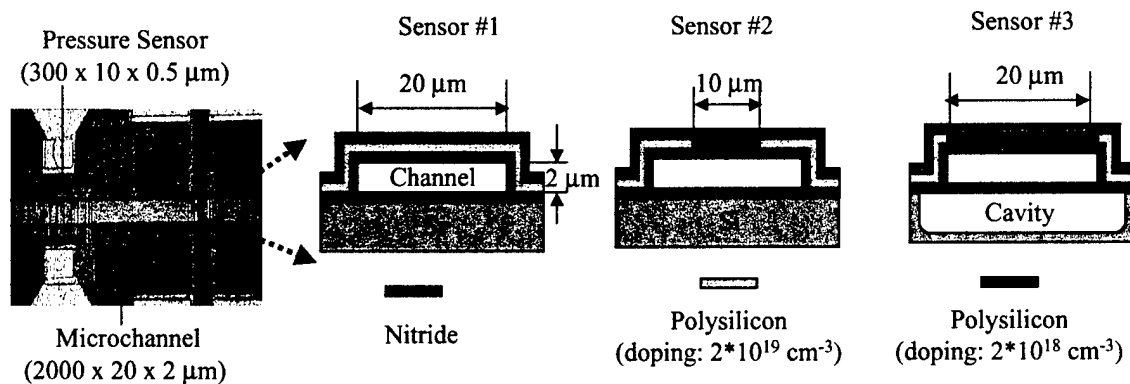

Figure 3.3.9. Photograph of pressure sensor and flow sensors integrated in a micro channel, and cross sections of three different designs of flow sensors

Process Flow

1. LPCVD nitride deposition (1μm)
2. LPCVD PSG deposition and
   patterning (~2μm)

3. LPCVD nitride deposition (0.5μm)
4. Etching PSG sacrificial layer

5. LPCVD polysilicon deposition (0.5μm)
6. B$^+$ implantation and sensors patterning

7. LPCVD polysilicon deposition (0.5μm)
8. Contact hole opening and metallization
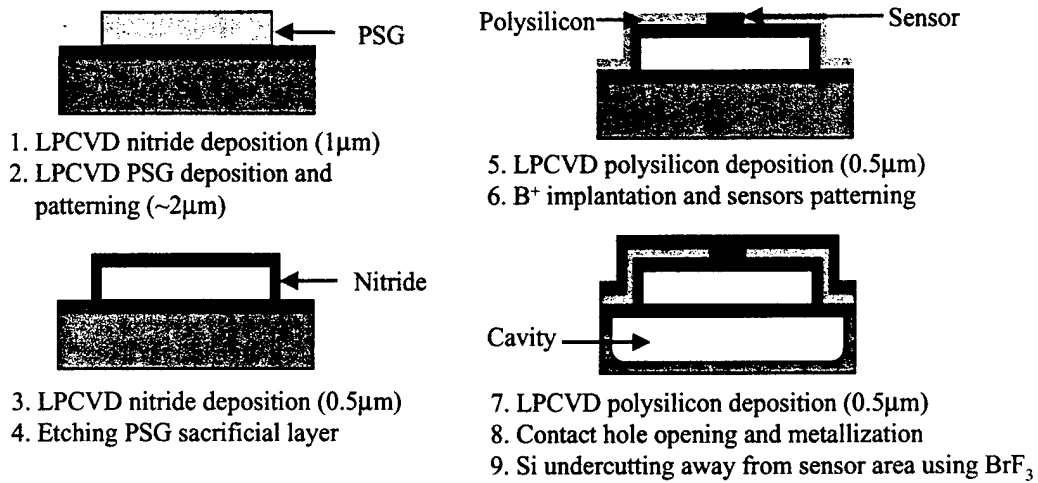9. Si undercutting away from sensor area using BrF$_3$

Figure 3.3.10. Process flow of a flow sensor integrated to a micro channel.

3.4 Test Procedures and Setup

These devices have been subjected to a series of rigorous tests in order to investigate the fluid dynamics of micro channel flow for inlet pressures up to 600 psig. These tests yielded results for inlet pressures that are orders of magnitude greater than any previous micro channel results available in the literature. The results from these tests have led to the formulation of a detailed flow model that takes into account several effects usually ignored in classical channel flow analysis.

Both gas and liquid flow measurements were conducted in the apparatus illustrated in figure 3.4.1. Microelectronic grade N_2 from a pressurized canister was passed through HPLC tubing into the suspended micro channel. An Omega type PX120 pressure transducer was used to monitor the inlet pressure, and an Omega model HHP-3200 digital manometer measured the exit pressure (with an uncertainty of 1.0 and 0.1 psia, respectively). Volume flow rates were measured using various calibrated glass tubes approximately 1.1 meter in length, and from 3 mm to 8 mm in (outer) diameter, depending on the flow rate being investigated. The volume flow rate in the tube was measured optically by monitoring the water meniscus as it moved past marked gradations and recording the time taken. Data for each set of flow parameters (at various inlet and outlet pressures) took from thirty minutes (for a gas) to four hours (for a liquid) to ensure steady state conditions. In addition, a vacuum/compressor pump was connected to the settling chamber at the end of the measurement tube. This allowed the exit pressure to be lowered to a maximum vacuum of -12 psig, or pressurized up to 20 psig.

Temperature calibration of the embedded sensors was conducted inside a Delta Design Model 2300 isothermal oven. The resistance was measured using a HP Model 34401A multimeter, and accurate temperature measurements, better than 0.01 °C, were obtained by an Omega DP-251 precision thermometer utilizing a calibrated RTD sensor element.
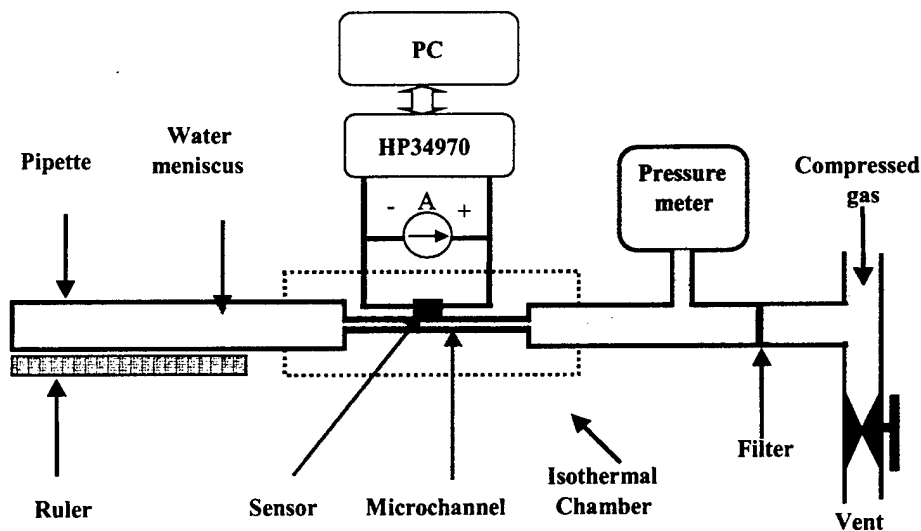
Figure 3.4.1. Experimental Setup for Channel Flow Study

3.5 Measurement Data and Discussion

3.5.1 Sensor Calibration

The micro channel is intended for high-pressure heat transfer experiments, and lightly doped polysilicon displays piezoresistive properties. Therefore, it is important to not only calibrate the sensor resistive output as a function of temperature, but also to compensate for any pressure effects. The data shows that the sensor temperature sensitivity is independent of pressure in the range between 0 and 300 psig. Figure 3.5.1 displays the nonlinear resistance dependence on temperature of three embedded sensors. Furthermore, the curves converge to each other, showing good uniformity of sensitivity to temperature among different sensors. Similarly, Figure 3.5.2 shows the sensor resistance change due to variations in pressure. The resistance sensitivity of the sensor to pressure is almost linear in the tested range, and is independent of temperature in between $10^{\circ}C$ and $40^{\circ}C$. Thus, the overall sensor sensitivity, parabolic with temperature and linear with pressure, can be expressed as:

$$(R-R_o)/R_o = \alpha_2(T-T_o)^2 + \alpha_1(T-T_o) + \beta(P-P_o) \tag{3.5.1}$$

where α_1, α_2, and β are experimentally determined to be approximately equal to $0.009\ ^{\circ}C^{-1}$, $6 \cdot 10^{-5}\ ^{\circ}C^{-2}$, and $10^{-5}\ psi^{-1}$, respectively.
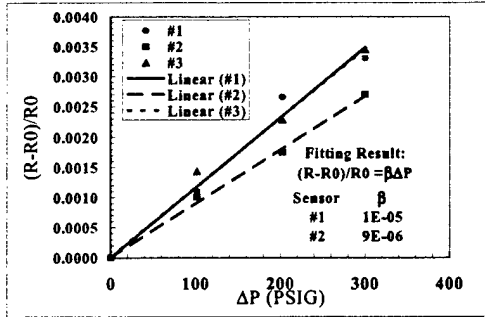
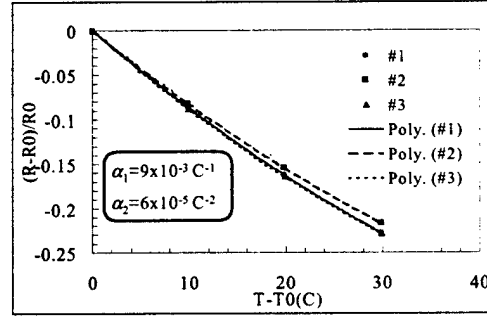Fig 3.5.1. Sensor sensitivity to temperature.   Fig 3.5.2. Sensor Sensitivity to pressure

3.5.2 Liquid Flow Rate Measurements

We first investigated the behavior of liquid micro channel flow, since the behavior of liquids is still incompressible even at elevated pressures. Classical analysis of steady, two-dimensional channel flow begins with the streamwise momentum equation. For fully-developed flow, $\partial u/\partial x=0$, the velocity profile is parabolic in y:

$$u = \frac{1}{2\mu}\frac{\partial P}{\partial x}(y^2 - \frac{h^2}{4}) \tag{3.5.2}$$

Then the volumetric flow rate can be derived by integration over the channel cross section:

$$Q_v = \int_{-h/2}^{h/2} uw\,dy = w\int_{-h/2}^{h/2}\frac{1}{2\mu}\frac{\partial P}{\partial x}(y^2 - \frac{h^2}{4})dy = -\frac{wh^3}{12\mu}\frac{\partial P}{\partial x} \tag{3.5.3}$$

where h, w, and L are the channel height, width and length, respectively, and μ is the fluid viscosity. Fully-developed incompressible flow implies a linear pressure distribution along the channel. Thus, the volume flow rate of DI water through the microchannel, Q_v, is expected to be linear with the pressure drop between the channel inlet and outlet.

$$Q_v = \frac{h^3 w}{12\mu L}\Delta P \tag{3.5.4}$$

Figure 3.5.3 displays data for the volume flow rate of DI water in the channel under various inlet pressures, which is nonlinear. This suggests that the channel deforms under high pressure since the experimental results deviate from the theoretical values calculated using Equation (3.5.4), as illustrated by the dashed line in Figure 3.5.3. We investigate this hypothesis by modifying the height term in the volume flow rate equation, accounting for the wall-deflection effect due to pressure, such that:

$$h = h_0[1 + \gamma P(x)] \tag{3.5.5}$$

where h_o is the nominal channel height of 1.85 μm at standard conditions, and $P(x)$ is the local pressure. By substituting Equation (3.5.5) into Equation (3.5.3), and assuming that $\gamma P(x) \ll 1$ so that higher order terms can be ignored, we get:

$$Q_v = -\frac{wh_0^3}{12\mu}[1 + \gamma P(x)]^3 \frac{\partial P}{\partial x} \approx -\frac{wh_0^3}{12\mu}[1 + 3\gamma P(x)]\frac{\partial P}{\partial x} \qquad (3.5.6)$$

After integrating along the channel and assuming $\Delta P \gg P_{out}$ in the case of very high input pressure, the following approximation for volume flow rate is obtained:

$$Q_v = \frac{h_0^3 w}{12\mu L}(P_{in} - P_{out})\left[1 + \frac{3}{2}\gamma(P_{in} + P_{out})\right] \approx \frac{h_0^3 w}{12\mu L}\Delta P\left(1 + \frac{3}{2}\gamma\Delta P\right) \qquad (3.5.7)$$

By comparing Equation (3.5.7) to Equation (3.5.3), we can define a correction term due to bulging as

$$\eta_{def} = (3/2)\,\gamma\Delta P \qquad (3.5.8)$$

Evidently, this geometric correction introduces a parabolic dependence on the pressure drop and explains the non-linearity of the data observed in Figure 3.5.3. Fitting the experimental data with Equation (3.5.7) yields $\gamma = 0.000132$ psig^{-1}. The effective deflection experienced at 500 psig for each channel wall is approximately 0.7% of the width, or 7% of the height, which corresponds to about 0.13 micron. Thus, fabricating channels with thicker walls can reduce the bulging effect.
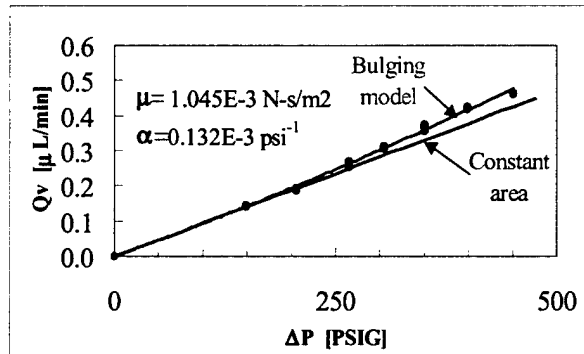

Figure 3.5.3. Modeling of micro channel deflection effects on high pressure gas flow, using a correction factor obtained from water flow data.

3.5.3 In Situ Deflection Measurements

The presence of bulging was confirmed using in-situ deflection measurements obtained from a WYKO model RST Plus optical profiler. Interferometric scans of magnified sections of the channel were taken in the WYKO's vertical scanning imaging (VSI) mode. A 30nm layer of Au-Pb was sputtered onto the channel in order to

circumvent the detrimental transparency of the nitride roof. Images at different input pressures, but at identical locations were digitally subtracted from each other in order to obtain the resulting deflection in the channel for a given pressure difference. The images were taken at 400 times magnification with an interrogation area CCD camera resolution of 256 x 256, yielding a resolution of about 0.24 um per pixel. Figure 3.5.4 is a computer calculated image which illustrates the resulting beam deflection near the inlet when an image at 300 psig is subtracted from an image at 0 psig. The maximum deflection measured is approximately 60 nm at $\Delta P = 300$ psig, which yields a $\gamma = 0.0001426$ psig^{-1}. Here γ is close to the value from the fit of the incompressible water measurements. This shows that the model is suitable to modify the water flow rate through the channel under high pressure.
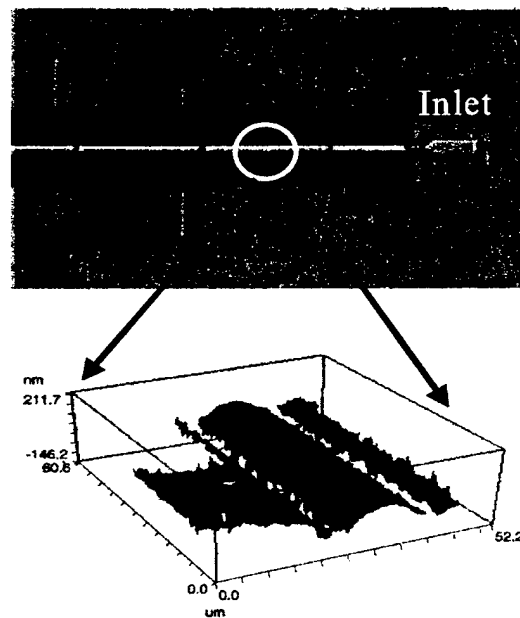

Figure 3.5.4. Sample processed 3-D WYKO image showing beam deflection near the inlet at 300 psig.

The maximum deflection measured, shown in Figure 3.5.4, is approximately 75 nm at $\Delta P = 300$ psig, which yields a $\gamma = 0.000178$ psig^{-1}. Here γ is close to the value from the fit of the incompressible water measurements [6]. Although the WYKO deflection results are consistantly lower than values obtained from fits of the volumetric flow data, we now have experimental evidence that the model is suitable for explaining high pressure deflection effects on the suspended micro channel's dimensions to within reasonable error.

Figure 3.5.4 shows high pressure deflection data along the channel. As expected, the deflection is highest the near the inlet, but channel structures such as stringers and knobs also have noticeable effects on the observed deflection, as illustrated by data near the 750 μm (knob) location. Stringers are connectors between the suspended channel and electrodes along the side. Temperature sensors are located at each stringer/micro channel

intersection, and they are spaced approximately 500 µm apart. Knobs refer to small protrusions near the midpoint between stringers that originally served as HF inlet ports to facilitate PSG etching of the channel.

3.5.4   Gas Flow in Micro Channel

Low-pressure gas flow

Before proceeding to high pressure gas flow, we tested the validity of the experimental procedure by investigating low pressure flow, in order to compare our results to previous results available in the literature. Nitrogen gas was passed through the microchannel at low and high pressures. We regard low pressure as being under 60 psia, which is comparable to the pressure range already investigated [7,8,9,13]. By assuming a parabolic velocity profile and neglecting the convection term, the mass flow rate for compressible flow with slip boundary condition is given by [7]:

$$Q_m = \frac{h_0{}^3 w P_{out}^2}{24RTL\mu}\left[\left(\left(\frac{P_{in}}{P_{out}}\right)^2 - 1\right) + 12Kn_{out}\left(\frac{P_{in}}{P_{out}} - 1\right)\right] \qquad (3.5.9)$$

where Kn_{out} is the Knudsen number at the channel exit and R is the specific gas constant.
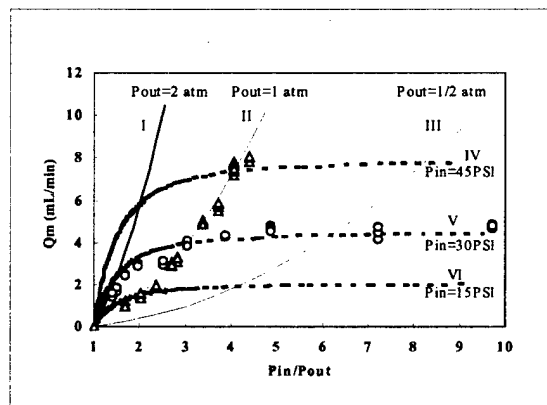

Fig. 3.5.5. Theory curves and experimental data for low pressure N_2 flow.

Two families of curves are plotted in Figure 3.5.5. The family shown in Figure 3.5.5 is the standard method of illustrating Equation (3.5.9), where the outlet pressure is kept constant; for example curve II is for P_{out}=1 atm. However, if P_{out} is fixed at a different level, curves I and III are sample results. Traveling left to right from curve I to III, the outlet pressure decreases from 2 to 0.5 atm. On the other hand, curves IV, V, and VI in Figure 3.5.5, also calculated using Equation (3.5.9), allow comparison of trends with fixed inlet conditions. Experimental data at a fixed outlet pressure of 1 atm is compared to curve II, while data for a fixed inlet pressure of 30 psig is compared to curve IV. Within experimental error, these data points fit well to the generally accepted low-pressure theoretical predictions. The agreement between the experimental results and the

theoretical calculations verify that the present setup provides an appropriate system to reliably obtain extremely small volume flow rate measurements. Furthermore, these results support the argument that flow acceleration and non-parabolicity effects are negligible at low pressures, and flow rate predictions taking into account only compressible and slip flow effects are accurate.

High-pressure Gas Flow

In order to estimate the influence of the flow terms ignored so far in this analysis, we refer to the work of van den Berg, et al.[10] for guidance. They derived equations for mass flow rate which takes into consideration the non-parabolicity of the velocity profile, as wells as the convection (acceleration) term of the momentum equation. However, their analytical study was for a capillary with a circular cross-section. Using hydraulic diameter arguments, we assume that the relative contributions of these effects for pipe flow are on the same order of magnitude for channel flow. Therefore, the factors contributing to the total mass flow rate can be estimated as follows

$$Q_m = Q_{mi} [1 + \eta_c + \eta_s](1 - \eta_a)(1 - \eta_p) \qquad (3.5.10)$$

where Q_{mi}, the incompressible mass flow rate, is equal to the volume flow rate in Eq 3.5.4, multiplied by the average density of the gas with respect to the average pressure. Hence the compressibility correction is expressed as

$$\eta_c = \frac{1}{2} \left(\frac{P_{in}}{P_{out}} - 1 \right) \qquad (3.5.11)$$

the correction due to slip effects is

$$\eta_s = 6 \, Kn \qquad (3.5.12)$$

the contribution from the convection term is

$$\eta_a = \frac{Q_{mi}}{6\pi\mu L} \ln \frac{P_{in}}{P_{out}} \qquad (3.5.13)$$

and the contribution of a non-parabolic velocity profile has an effect on the order of

$$\eta_p = \frac{Q_{mi}}{12\pi\mu L} \ln \frac{P_{in}}{P_{out}} \qquad (3.5.14)$$

Substituting in values, for η_a and η_p, it is apparent that these terms are much less than 1, so higher order terms can be neglected and Eq. 3.5.7 can be rewritten as

$$Q_m = Q_{mi} [1 + \eta_c + \eta_s](1 - \eta_a - \eta_p) \qquad (3.5.15)$$

It is readily apparent that when the acceleration effect and the effect due to the non-parabolic velocity profile are taken into consideration, this should actually result in a lower theoretical mass flow rate. For example, the difference between the usual non-slip curve and the curve with takes into account acceleration and non-parabolicity is about 6% at 600 psig (pressure ratio is about 40), as seen in Figure 3.5.6.

In Figure 3.5.5, at higher-pressure ratios the data deviates from the lower curve, which takes into consideration acceleration and a non-parabolic velocity profile. This discrepancy between measured and theoretical values calculated from Eq. 3.5.15 can now only be attributed to deformations in the channel geometry due to high pressure of the channel. An effective mass flow rate can be written as Eq. 3.5.16,
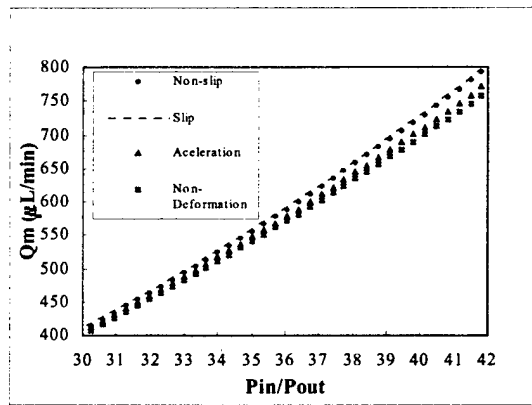

Fig. 3.5.5. Mass flow rate vs. inlet pressures, with curves at various exit pressures, slip and no slip theoretical curves, and a curve with acceleration effects.

$$Q_{effective} = Q_m \left(1 + \eta_{def}\right) \tag{3.5.16}$$

which takes into consideration flow acceleration and non-parabolicity, as well as geometry. In Eq 13, the deformation correction term is given by

$$\eta_{def} = \alpha P_{in} \left[1 - \left(\frac{P_{out}}{P_{in}} \right)^3 \right] \tag{3.5.17}$$

which is derived from the gas flow momentum equation by using Eq 3.5.7 again to model the high-pressure deflection .

Figure 3.5.7 illustrates that the measured data fits the mass flow rate theory when flow acceleration, non-parabolic flow velocity profile, and channel deformation due to high pressures is taken into consideration.
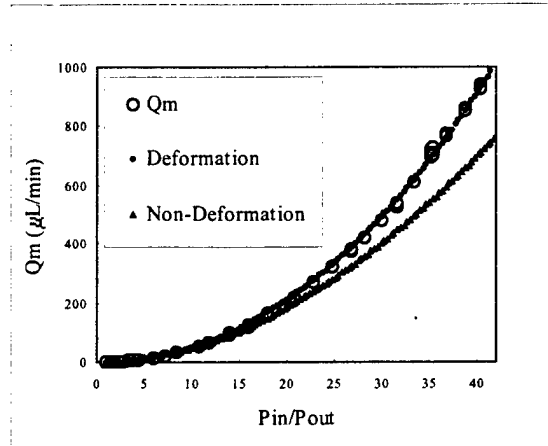
Fig. 3.5.7 Mass flow rate vs inlet pressure..

3.5.5 Temperature Measurements along Micro Channel with High-Pressured Gas Flow

Having previously characterized the flow inside the channel, we proceed to examine the temperature profile along the channel for various inlet pressures. Figure 3.5.8 shows the temperature profile at various inlet pressures, as measured by the 8 free standing temperature sensors within the 2nd generation micro channel. Even at 300 psig, there is no appreciable temperature difference (less than 0.1 $^\circ$C) along the length of the channel. This would indicate that either heat conduction in thin film nitride is greater than heat generation by the flow or that the energy loss due to the conversion of flow energy into viscous frictional energy is negligible in this micro channel configuration.
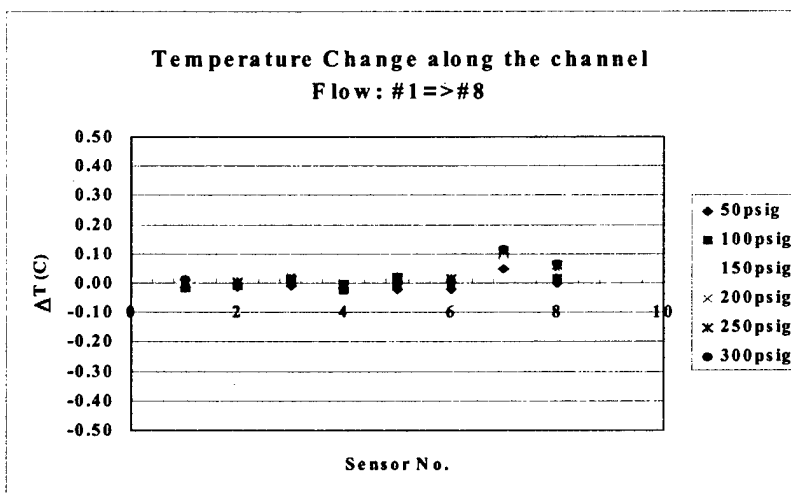

Figure 3.5.8. Temperature distribution within a micro channel at various inlet pressures.

3.5.6 Nano-Flow Sensor Test Results

We have successfully demonstrated a polysilicon channel-flow sensor for measuring small liquid channel flow with an unprecedented resolution better than 10nL/min. The sensing mechanism is based on micro/nano thermal heat transfer between the channel fluid and the heater/sensor. More interestingly, we further confirmed that micro bubbles going through the channel can also be detected. This is a unique and crucial advantage because bubble detection is important issue for microfluidics. Finally, we have devised a thermal model of our sensor that allows us to simulate the flow meter operation. The results are in good agreement with experimental data.

The basic operation principle of the flow sensor utilizes the micro convective heat transfer that occurs from a heated polysilicon temperature sensor to the fluid. We started with a test design where a medium-doped polysilicon sensor is embedded in the nitride wall of a microchannel. Later, we improved the sensor into a suspended channel with embedded lightly doped polysilicon sensors, resulting in better sensitivity. Accordingly, we have improved our sensor resolution from 100nL/min to 10nL/min.

Our experimental results can be summarized in figures 3.5.9 - 3.5.11. Figure 3.5.9 shows the temperature calibration and TCR's of -0.17%/K, -0.56%/K, -0.76%/K respectively for each successive generation of flow sensor design. Figure 3.5.10 and 3.5.11 show the sensor response to mass flow rate in the channel. The suspended channel flow meter shows improved sensitivity when compared to the other two designs. From figure 3.5.12, we see that for the same given power (140μW), the suspended flow sensor gives the best response (0.0263 °C/nL/min), about 5 times better than the first two sensors.
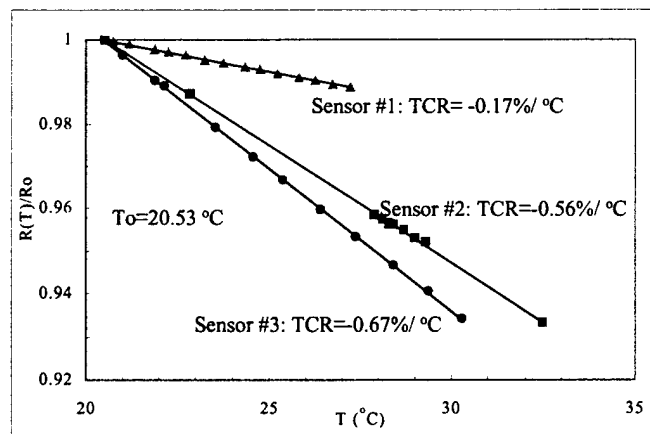

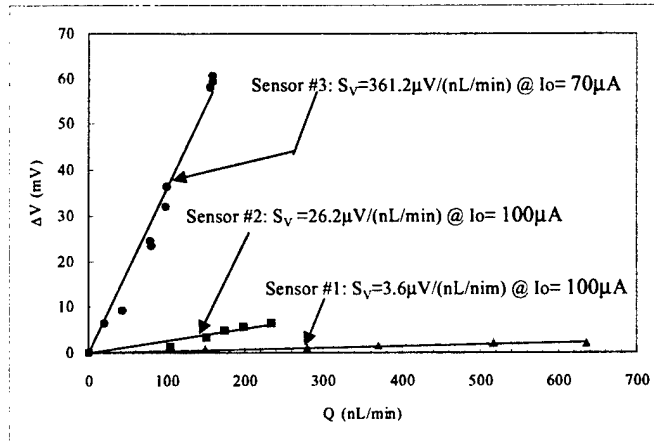Figure 3.5.9. Temperature dependence of three types of sensors.

Figure 3.5.10. Characteristics of the flow sensors with three different designs.
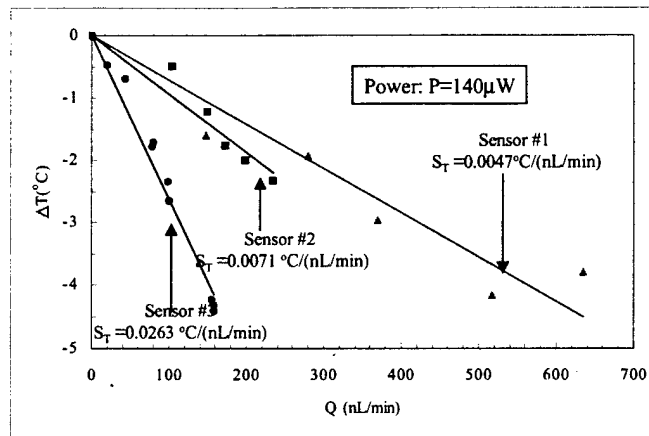

Figure 3.5.11. Temperature change of the sensors due to liquid flow.

3-D FE simulations using ABAQUS were performed to model our channel flow meter. We have built a model that addresses the coupled conduction-convection within the flowmeter. Heat conduction is considered for the nitride walls, the embedded polysilicon heater/sensor, and the surrounding air, while forced convection is considered for the liquid flow. Figure 3.5.12 shows the simulated temperature distribution along the flowmeter channel at a flow rate of 100 nL/min. The calculated and measured average sensor temperatures as a function of flow rate are shown in Figure 3.5.13. From this figure it can be observed that the agreement between theory and experiment is quite good. The discrepancies may be due to uncertainties in the channel geometry, heat loss along the polysilicon leads to the substrate, and free convection of air.
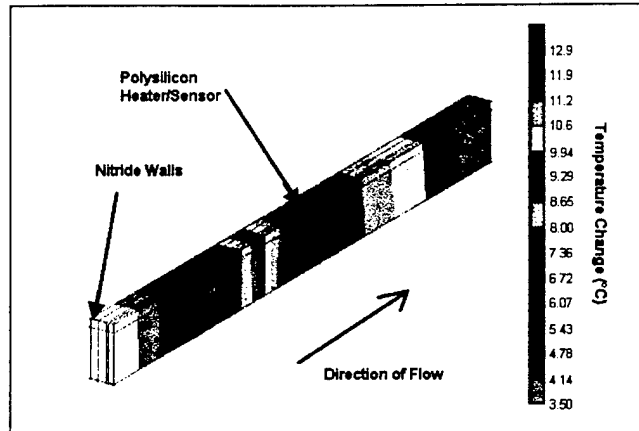
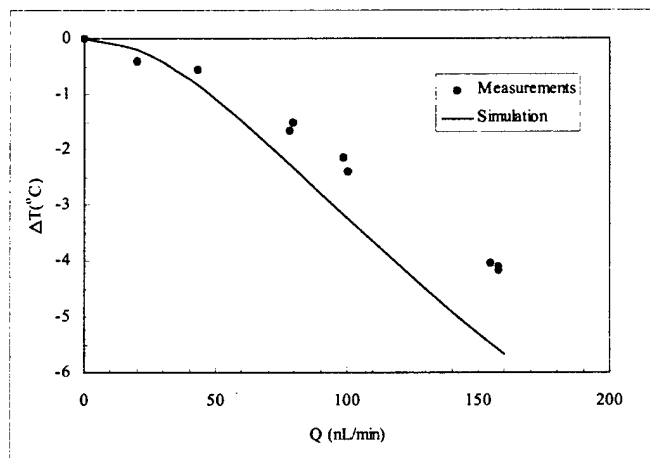Figure 3.5.12. Simulation model and ΔT distribution under 100nL/min.

Figure 3.5.13. Simulation results vs. measurement data of suspended channel

Finally, our flow sensors detect not only fluid flow, but also air bubbles. In figure 3.5.14 the passage of air bubbles is logged using real-time data acquisition. Since air has a lower heat capacity and conductivity than water, the sensor sees a sudden temperature rise, shown as spikes in figure 3.5.14. Further investigation is underway to investigate the possibility of detecting foreign particles other than air bubbles. This can be particularly useful in micro-chemical reaction applications where bubbles or particles are crucial.
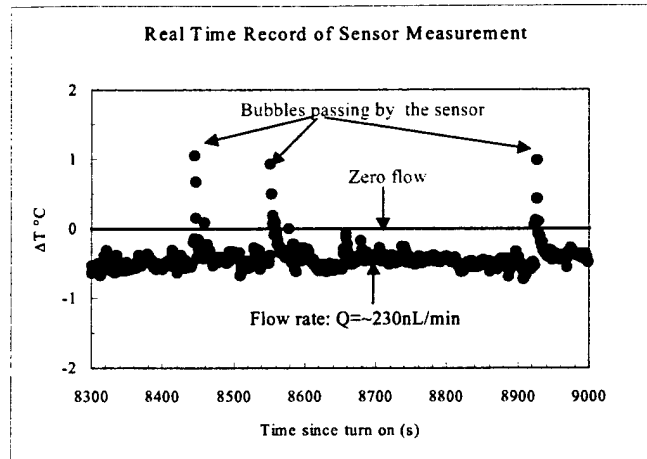
Real Time Record of Sensor Measurement

Figure 3.5.14. A real time record of sensor measurement of the temperature spikes up
when air bubbles passes by the sensor.

3.6 Conclusion

The robust nature of these microchannels facilitated high-pressure measurements. Mass flow data at unprecedented high inlet pressures has been successfully obtained, and the deviation of this data from theory is attributed to fluid flow effects such as local flow acceleration and a non-parabolic velocity profile, as well as to bulging in the channel. This bulging effect was isolated and measured using incompressible liquid flow. In addition, at a fixed inlet pressure, a complete saturation flow rate curve has been obtained by evacuating and pressurizing the exit of the channel. The pressure measurement data shows nonlinearly distribution along the channel because of slip boundary conditions. Most importantly, we obtained coefficients for the parabolic dependence of the resistance of the imbedded thermal sensors to temperature, as well as the coefficient for the sensor's linear dependence on pressure. Our temperature distribution shows negligible temperature change data along the channel with a high-pressured gas flow, and for the first time directly provides the evidence to prove that it is reasonable to treat micro channel flow as isothermal flow. Also, we have successfully demonstrated a polysilicon channel-flow sensor for measuring small liquid channel flow with an unprecedented resolution better than 10nL/min. More interestingly, we further confirmed that micro bubbles going through the channel can also be detected. This is a unique and crucial advantage because bubble detection is an important issue for micro fluidics. Finally, we have devised a thermal model of our sensor that allows us to simulate the flow meter operation. The results are in good agreement with experimental data.

4. PROJECT SUMMERY

In this project we have systematically studied the fundamentals, as well as the practical implications, of impinging jet and jet-array cooling. For the first time, we successfully developed a MEMS-based heat transfer measurement paradigm including a technology for MEMS device fabrication, an experimental setup well suited for micro scale thermal study, and an accurate and efficient data processing technique. Our MEMS-based measurement paradigm integrates sensing and heating, and allows measurement in a significantly large area at a very high spatial resolution. The heat transfer data demonstrate the excellent promise of micro-impinging-jet heat transfer, and provide useful rules for designing impinging-jet-based micro heat exchangers for IC packages. Our investigation of unsteady impinging jets has demonstrated that unsteady impinging jets can further enhance the heat transfer.

Furthermore, micro channel flow, which is related to the fluid and thermal transfer of impinging jet cooling system, has been carefully investigated as well. We have successfully fabricated micro channels with integrated temperature, pressure and flow sensors, which are designed to investigate the basic science of micro-scale channel flow. Considerable discrepancies between existing theory and experimental data have been observed, and we have proposed an improved flow model, that appropriately accounts for such discrepancies. Finally, we have demonstrated a polysilicon channel-flow sensor for measuring small liquid channel flow with an unprecedented resolution better than 10nL/min and developed a simulation model of the sensor.

5. ACKNOWLEDGEMENT

6. REFERENCES

[1] Tien, C-L, Majumdar, A., Gerner, F., ed. Microscale Energy Transport Series in Chemical and Mechanical Engineering, Taylor & Francis, 1998.

[2] Hollworth, B., Durbin, M., "Impinging Cooling of Electronics," J. Heat Transfer, v. 114. p.607-613, August 1992

[3] Martin, H., "Heat and Mass Transfer between Impinging Gas Jets and Solid Surface," Advances in Heat Transfer, v. 13, 1997

[4] Kasagi, N., "Forced Convection and Turbulence in Thermal Control," Chapter 3, Cooling Techniques for Computers, Win Aung, ed., Hemisphere Publishing Corporation, New York, 1991 pp. 97-140.

[5] Knisely,C., and Rockwell, D., "Self-sustained Low Frequency Components in an Impinging Shear Layer," J.Fluid Mechanics. v. 116, pp. 157-186, 1982.

[6] J. Pfahler, J. Harley, H. Bau, J. Zemel, "Gas and liquid flow in small channels," Symp. Micromechanical Sensors,Actuators, and Systems (ed. D. Cho, R. Warrington, et al.) ASME DSC v.32, p49-60, 1991.

[7] E.B. Arkilic, M.A. Schmidt, K.S. Breuer, "Gaseous flow in microchannels," Application of Microfabrication to Fluid Mechanics, ASME Winter Annual Meeting, pg. 57-65, Chicago, IL Nov. 1994.

[8] K.C. Pong, C.M. Ho, J. Liu, Y.C. Tai, "Non-linear pressure distribution in uniform microchannels," Application of Microfabrication to Fluid Mechanics, ASME Winter Annual Meeting, pg. 51-56, Chicago, IL Nov. 1994.

[9] J. Liu, Y. C. Tai, K. C. Pong, and C. M. Ho, "Micromachine channel/pressure sensor systemf for "microflow studies", Transducers' 93, pp.995-997

[10] J.C. Shih, C.M. Ho, J. Liu, Y.C. Tai, "Monatomic and polyatomic gas flow through uniform microchannels," Application of Microfabrication to Fluid Mechanics, ASME Winter Annual Meeting, pg. 197-203, Atlanta, Ga, Nov. 1996.

[11] R.K. Prud'homme, T.W. Chapman, J.R. Bowen, "Laminar compressible flow in a tube," Appl. Sci. Res. v.43, p.67-74, 1986.\

[12] H.R. van den Berg, C.A. Seldam, P.S. Gulik, "Compressible laminar flow in a capillary," J.Fluid Mechanics, v. 246, p.1-20, 1993.

[13] J.C. Harley, Y. Huang, H.H. Bau, J.N. Zemel, "Gas flow in micro-channels," J.Fluid Mechanics, v. 284, pp257-274, 1995.

[14] X. Wang, X. Yang and Y. C. Tai, " Gas-Phase Silicon Etching with Bromine Trifluoride, pp.2D3.02, Transducer '97, Chicago

7. PUBLICATIONS RESULTED FROM THIS PROJECT

[1] S. Wu, Q. Lin, Y. Yuen, and Y.C. Tai, "MEMS Flow Sensors for Nano-Fluidic Applications", *Proc. 13th Annual International Workshop on Micro Electro Mechanical System, January 23-27, 2000, Miyazaki, Japan.*

[2] S. Wu, Q. Lin, Y. Yuen, Y.C. Tai, and C.M Ho, "MEMS Impinging-Jet-Array Heat Exchangers", *Proc. 13th Annual International Workshop on Micro Electro Mechanical System, January 23-27, 2000, Miyazaki, Japan.*

[3] Roger Allan, "Technology Breakthrough: MEMS Micro Heat Exchangers Employ Impinging Jets To Boost Cooling Efficiency", *pp. 29-30, Electronic Design, April 5, 1999.*

[4] Lawrence Kren, "Electronics in The News: Micro Jets Help Chips Chill", *pp. 62, Machine Design, June 3, 1999.*

[5] S. Wu, J. Mai, Y.C. Tai, and C.M. Ho, "Micro Heat Exchanger by Using MEMS Impinging Jets", *Proc. 12th Annual International Workshop on Micro Electro Mechanical System, pp. 171-176, January 17-21, 1999, Orlando, Florida.*

[6] S. Wu, J. Mai, Y. Zohar, Y.C. Tai, and C.M. Ho, "A Suspended Microchannel with Integrated Temperature Sensors for High-pressure Flow Studies", *Proc. 11th Annual International Workshop on Micro Electro Mechanical System, pp. 87-92, January 25-29, 1998, Heidelberg, Germany.*